

# Industrial aerodynamics

Edited by Frédéric L. Chalot<sup>1</sup>

<sup>1</sup> *Direction Générale Technique, Dassault Aviation, Saint-Cloud, France*

## ABSTRACT

This chapter describes the use of computational fluid mechanics at Dassault Aviation. A historical perspective gives a measure of the successive giant steps that have been made over the past 30 years. A rather detailed description of industrial codes leads to a good understanding of the key numerical concepts assembled to create a powerful tool for computational aerodynamics. The fundamental issue of turbulence modeling is addressed in detail. A large range of complex applications is described to illustrate the variety of problems solved. The status of the development and application of shape optimization techniques and multidisciplinary design are finally illustrated.

KEY WORDS: aerodynamics; military aircraft; passenger aircraft; space vehicle; Euler; Navier-Stokes; flow control; shape optimization

## 1. INTRODUCTION

As we celebrate the centennial of powered flight, the understanding of aerodynamics and flight mechanics has gone a long way...

Aircraft design went from trial and error testing with essentially only flight experiment, virtually no wind tunnel, and very little theory or modelization at the time of the Wright brothers, to heavy use of ground experiment in facilities of various sizes, and nowadays to unforeseen computer simulations. Such an evolution was not obvious at all, say fifty or even twenty years ago. We remember a day in the mid eighties when Euler calculations over a complete aircraft would seem forever impossible to some aerodynamicists in the industry. A few visionary engineers though knew that one day the combination of advanced numerical analysis, detailed physical modelization and powerful computer would make this dream a daily reality: compute the turbulent flow past a complete industrial configuration. The adventure is on-going...

The key contributors to a successful aerodynamic design are three-fold: wind tunnel testing, theoretical modelization, and eventually of course flight testing. These three type of activities have always contributed to design. They were pretty much unbalanced though. Nowadays they tend to become even: flight testing being more and more expensive is reserved for ultimate design evaluation; computer simulations on the other hand get more and more affordable and provide more and more useful information.

As an example, the advanced design for a new generation combat aircraft such as the Rafale, required over 6000 hours of wind tunnel testing, before the first flight; over 850 flights of the Rafale A demonstrator; and made extensive use of the CFD codes available at the time. This is illustrated

in Figure 1. The new Falcon 7X configuration was tested during over thirty wind tunnel sessions, each lasting from one to several weeks. Tens of full 3-D turbulent Navier-Stokes calculations were performed to finalize the shape. It will start its flight testing in 2005.

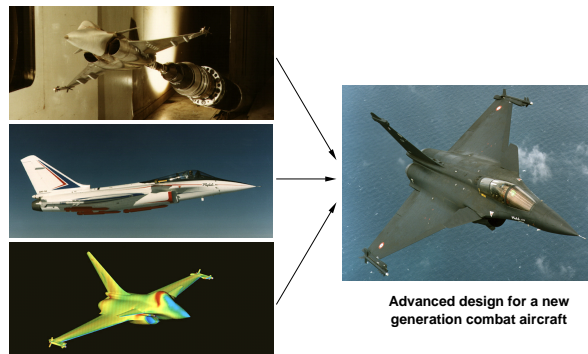


Figure 1. Three components of advanced design: experiment, modelization, and flight testing.

Over a few decades, CFD went from producing pretty pictures to providing a better understanding of complex flows and to producing ways to design better airplanes. Ground testing and experimental techniques have gone a long way as well: non intrusive velocimetry and visualization techniques, such as PIV, PSP, or LDV, have provided the engineers with new means of analysis and tools to validate their designs and models. Validation is an on going process: in every new study or program, we incorporate wind tunnel calibration tests to further validate and extend the range of application of our simulation tools.

This chapter will address the key issues of industrial aerodynamics. It will not attempt an exhaustive review of the many outstanding tools, methods and applications achieved at the main research institutes (NASA, ONERA, DLR, NAL. . . ) or throughout the industry. Present status and future challenges will mainly be addressed by considering computational aerodynamics at Dassault Aviation where this topic is identified as a key area for the design of high performance civil and military aircraft, and space vehicles. A number of field of application are not discussed, most notably concerning turbomachinery, rotary wings and helicopters, automotive and train industry.

## 2. THE HISTORICAL DEVELOPMENT OF COMPUTATIONAL FLOW MECHANICS

*By Pierre Perrier, secretary, French Academy of Technology and foreign associate, National Academy of Engineering.*

As a starting statement, one can say that the complete design by computer of an aircraft which was only a dream fifty years ago has almost become routine at the turn of the century. When only hand computations and heavy experimental facilities were available in the past, supercomputers with advanced codes complement or replace these tools nowadays.

From an outside eye, the transition to virtual design is often perceived as a step forward, which was in fact only recently achieved, and as the end-point of a continuous increase in the power of computers, from supercomputers to PC's. But the real development of computerized design has been an on-going improvement procedure: continuous increase in the design efficiency has resulted in better performances and cost effectiveness thanks to a better mastering of the flows around and inside vehicles. It has been a complex balance between almost continuous improvement of hardware and a few major discontinuous steps in software, such as the inclusion of new algorithms which resulted in major advancements in design capabilities.

It is particularly clear in the case of flow mechanics, that such major advancements can be identified along the way in the somewhat short history of computational aerodynamics and thus define a few major historical milestones. The steps correspond to new ideas introduced in numerical computations which allowed new design concepts and finally yielded unprecedented qualities in the end products of the technology. Moreover, a competition between computational and experimental studies came to its end when their complementary use was conveniently balanced and understood. Taking into account the complexity of real unsteady tridimensional flows, we can nowadays perceive the limitations of computational fluid mechanics by a proper evaluation through "numerical vs experimental" workshops. So CFD and wind tunnels have found their complementary domain of utility, clarifying a somewhat controversial debate about real and virtual worlds, about actual physics and modeling.

### *2.1. The first step: first solvers and their vanishing efficiency*

Before World War II, only analytical resolutions of partial differential equations were of practical usefulness thanks to explicit algebraic solutions, with the help of tabulated data. The introduction of analogical and digital computers, as a complement to desk machines, allowed the selection of numerical techniques relying on simple matrix inversions and tabulations of basic functions (e.g. log and trigonometric functions). Those were only computed more easily when computer speed improved.

All the major aeronautical research centers (NACA, RAE, ONERA, and TSaGI) built at that time tables for aircraft aerodynamic design. A few of them were more sophisticated in their use of mathematics and/or analogic physical solvers. For example, Peres and Malavard tabulated values giving loads on wings due to camber and twist. They made a convenient use of linearized approximations and rheoelectric analogical computers. A distribution of electric potentials was placed in a water tank where a 3-D metallic model was instrumented. Such a distribution on the body permitted the resolution by a perturbation method of design problems with an elementary solution of the Laplace equation for incompressible flows. Similarly, solutions of the linearized wave equation for supersonic flows along Mach lines were extracted by analog computers; they solved time dependent perturbations generated through an array of electric amplifiers connected in a line-by-line and transverse fashion.

The first true advancement in solving such unsteady finite differences between nodes of an array of



Figure 2. Peres and Malavard's rheoelectric tank.

points was initiated in Great Britain in the 1950's by hand computing. A manual iterative relaxation procedure for solving Laplace equation revealed itself as a viable computational process; it was in fact an efficient algorithm, if some care was taken to handle data correctly. One had to work line after line and reduce progressively the errors in order to fulfill the equations approximated in finite differences. Used in numerical computers, the under-relaxation method was an efficient solver of Laplace equation, with boundary conditions specific to each configuration. It was discovered later that it was in fact a time marching procedure towards an assumed steady state. Irregular arrays of points could be adjusted to local gradients in the solution; but it appeared that the time step had to be chosen according to the smaller distance between points with a conditional stability parameter. The speed of convergence of relaxation methods together with the need to partition the space following the different equations to solve, appeared as a major computational problem when the algorithm was used on early computers. Work done in Germany on viscous boundary layers became useful at the time and research on viscous and inviscid flows pursued separated ways for a long time.

An advancement in inviscid flow rebuilding by computation took advantage of the linearity of the equations: the linear superposition of the field of singularities known by analytical solutions offered an alternative to the poor efficiency of finite differences at that time. It was the first main battle between very different flow solvers, with a stress put on efficient linear system resolution or matrix inversion. When a large number of control points on boundaries had to be handled (associated with "sources" and "sink" points) the computation time and the computer memory size increased from hundreds in the 1960's to thousands in the 1970's; but the quality of 3-D results remained comparable to relaxation in finite differences, although finite differences required at least ten times as many collocation points across the field of computation. Similarly, an extension coupling sinks and source points with horseshoe vortices placed along the surface soon appeared as an efficient algorithm for lifting wings.

The names which illustrated that period of time, when "integral methods" became the usual mathematical tool in industrial use, were Weissinger for lifting surfaces and later Hess and Smith for complete incompressible pressure on the surface of an aircraft. At that time, the numerical computation phased out the analytical tools and the rheo-electric 3-D analogic computers of Peres and Malavard.

The analytic solution for 2-D wing sections by harmonic transformation of coordinates remained in use due to the improvement of discretized exact analytical solutions derived for lifting inviscid cylinders; but the multi-body high-lift devices phased out as well such analytical methods focused only on single body transformations.

As far as non-linear compressible aerodynamics was to be used in design for transonic aircraft, it was however clear that the next step would open the way to finite difference methods: they were more efficient in supersonic and subsonic compressible flows, but not able yet to be adjusted to complex geometries and boundary conditions of a complete aircraft.

The progress in finite difference algorithms came from advances in compressible flow computations, for a very specific problem: the solution of hypersonic flow around blunt bodies, with a continuous acceleration from the stagnation point to subsonic and supersonic flow. The classical problem of supersonic flow around a forebody of cylindrical shape gave birth to efficient iterative time-dependent potential flow and also Euler flow (with all three conservation equations: mass, momentum, and energy) solvers, thanks to the progress done by Moretti and many others in the US. At the same time, and for the same problem, an approach based on the integral evaluation of a polynomial solution of pressure on a limited number of bands located in the region between the shock wave and the body was achieved in USSR by Dorodnitsin; this approach was efficient because it led to a set of coupled ordinary differential equations (ODE) between the coefficients of the polynomial expansion, thus not requiring a large computation time. Surprisingly efficient with a reduced number of bands, it appeared as not converging when the number of bands and coefficients increased much, a trend inverse of what may be obtained with refined meshes in a finite-difference-method (FDM) approach. One discovered that an increase in stabilization by the addition to the relaxation scheme of some artificial viscosity gave a more robust numerical output; consequently, FDM had the capability to precisely capture the detached shock ahead of the body. The way was open for the solution of the supersonic inviscid thick wing section problem. Taking into account the swept wing problem with subsonic flow normal to the leading edge, a few tentative tests were made to calculate the flow past inviscid transonic wing sections, but with a very large computation time resulting from very small time steps; that precluded the recurrent use of the methods in the design process of real transonic wings or compressor blades. Moreover, only 2-D computations were tractable and quasi 2-D methods were the only engineering methods available.

## *2.2. The second step: opening finite differences to efficient solvers for transonic problems*

The search began to go from incompressible to compressible flows: in finite difference solvers, iterative procedures were extended on simple rectangular grids and for integral solvers the iterative addition of compressibility sources and sinks was introduced in the field. But such a procedure was unstable in supersonic flow for integral methods and in finite differences required upwinded relaxation schemes for stability and gave unrealistic double shock patterns. So the empirical corrections built by correlations of experimental results and theoretical ones remained useful for design; the more elaborated data sheets were done by RAE in England. Analytical solutions of smooth (i.e., without shock wave) transonic flow was obtained by NLR in the Netherlands in support for correlations.

The true advancement avoided the non-physical leading edge shock using a perturbation method in the leading edge area; true boundary conditions on wing sections were also transferred to its meanline. So a transonic thin-wing finite difference approximation allowed for the first time a prediction of the pressure distribution on a realistic swept wing with shock wave thanks to the team of Murman and Cole (1971). Such a tool opened the way to the first efficient 3-D transonic design which was applied to the Boeing 727 and 747 series. However, the final design still relied on intensive wind-tunnel testing

to take into account the interactions with the fuselage, the pylons, and the nacelles. A rectangular mesh was well suited for shock waves normal to the body and the direction of the incoming velocity; however the singularity added at the leading edge was a limitation for the design of the forepart of the wing section which remained difficult to optimize. In parallel, a 2-D unsteady approach was developed by Yoshiara. Theoretical work validated by computer entered for the first time in competition with a pure trial and error design: the iterative modification of the geometry of a 2-D model in transonic wind tunnel was developed by Whitcomb at NASA Langley. Some evaluation of boundary-layer flow in uncoupled mode was tested in France and in the US for the prediction of the extension of separated flows.

### 2.3. The third step: building of an efficient 3-D transonic finite-difference solver

Computational work began to be of value in transonic research at NASA Ames with Balhaus and others and in the academics with Jameson (1975). The latter soon became a reference. He successfully added to the solver ingredients often painfully discovered by many others. The computation time was consequently drastically reduced; the accuracy improvements allowed precise comparison of different designs. So the work in the US led to the first efficient codes for the prediction of the transonic potential flow around a swept wing; and later around blades of rotating machines with a boundary fitted refined mesh and a variable spacing of nodes in the field for a better prediction of the flight pressures. The predicted position of shock waves without inclusion of boundary layer coupling, was roughly the same as in wind tunnel testing; the numerical viscosity of the solver luckily appeared to work as the effect of the true viscosity inside the viscous boundary layers.

Parallel to this work, and also for the transonic inviscid potential flow, the French team led by Glowinski and Perrier built a new mathematically consistent solver, based on a finite element method and using tetrahedra as elementary control volumes (Bristeau *et al.*, 1985). Such a solver allowed the first computation of a complete aircraft in transonic flow with all of its topological complexity: vertical tail and horizontal stabilizer, engines and nacelles (see Figures 3–5).

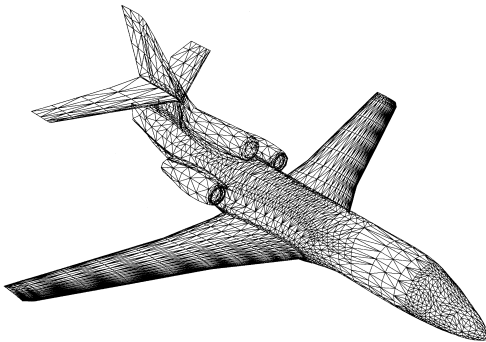


Figure 3. Falcon 50 surface mesh.

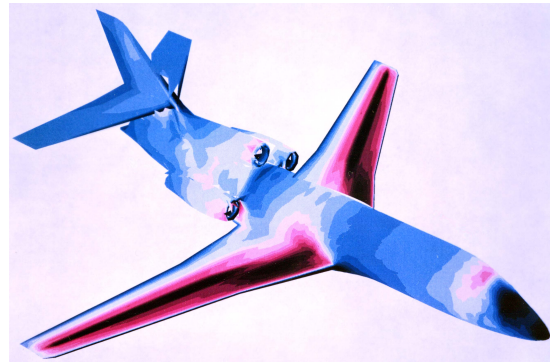


Figure 4. Falcon 50 pressure distribution.

It appeared that advancement in computational quality required a better rebuilding of entropy production through shock waves, viscous dissipation and convection in viscous layers. Anyhow, the first optimization of the aerodynamical shape of a complete aircraft was possible, but the effort had to be pushed ahead onto Navier-Stokes solvers. Work done in finite differences by Lax was at the limit of

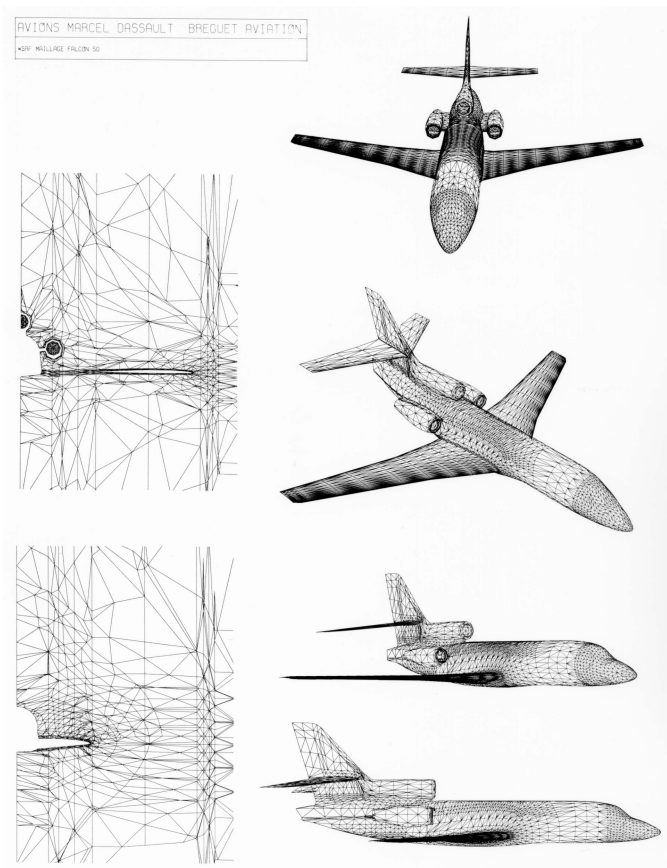


Figure 5. Falcon 50 mesh.

foreseen development of computers: it was restricted to small parts of the flow and already made use of turbulence modeling. Coupling viscous layers and potential flow was equally reorienting the work on Euler solvers able to convect entropy losses in shocks and viscous layers. Finite difference schemes were reoriented towards finite volumes; complex geometries were to be addressed by the partition of space to manage the topological complexity of real geometries of aircraft, engine, cars...

First Navier-Stokes equation solvers exemplified the dramatic distance in Reynolds number between real flows and engineering models, and the need for convenient turbulence modeling.

#### 2.4. The fourth step: building Euler and Navier-Stokes solvers for supercomputing

The increasing power of computers in the eighties opened the way to more refined meshes and more complete equations. Euler solvers were progressively built as new tools for design. This came with many problems though. A few of these problems arose from the necessity of truncation of spurious modes in the flow; from acoustic waves generated by the transient discretized errors; or from the unsteadiness of the flow. Another type of problems came from the non-uniqueness of

solutions with discontinuities without constraints on entropy evolution or dissipation in recirculating flows. The introduction of forcing source terms and the management of numerical viscosity in the discrete algorithm helped eliminating numerical artifacts. Many researchers on both sides of the Atlantic contributed to that golden age of the building of computational flow dynamics with a major impact on industrial design. In parallel, T.J.R. Hughes at Stanford (Hughes, Franca and Mallet, 1986; Shakib, Hughes and Johan, 1991; Chalot, Hughes and Shakib, 1990; Chalot and Hughes, 1994) helped reorienting the work on finite element methods towards an efficient Navier-Stokes solver that allowed the necessary robustness for the prediction of highly compressible flows with chemistry as encountered by reentry vehicles. The concurrent investment in multi-domain/multi-mesh finite difference or finite-volume solvers and in finite element filling of the space around complex geometry led to a first group of really efficient codes for design: many “physical” ingredients in the algorithms tried to emulate the more physical output of refined Navier-Stokes solvers. An example of an inviscid code benefiting from advanced thermochemical models is provided in Figure 6. It shows the importance of “real gas” effects in the interaction between the detached shock wave and the winglets of the Hermès space plane.

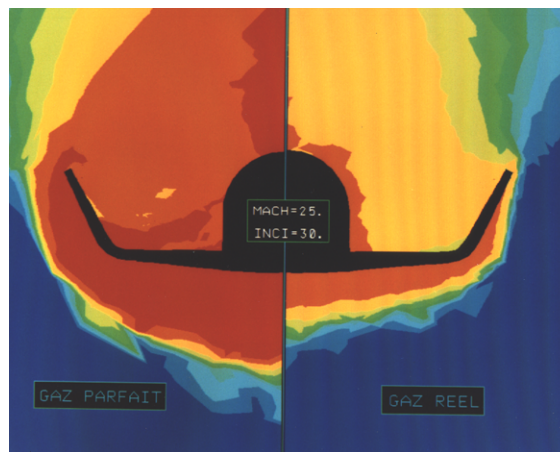


Figure 6. Hermès space shuttle: real gas effect.

If the work on Euler codes led to efficient solvers, the true engineering challenge appeared in mesh generation. The finite difference methods needed a body fitted mesh generator and in fact streamline-fitted sets of points in 3-D; points were to be ordered in three reduced coordinates  $i$ ,  $j$ , and  $k$ . Smooth variations in the distances between points were mandatory, even with the improvement in robustness of algorithms with finite volume approximations, closer in spirit to finite element methods. A multiscale approach with progressive refinement of meshes added constraints as the geometrical connection between the blocks needed to cope with the topological complexity of engineering designs. The finite element method showed its effectiveness, escaping from “ $ijk$ ” constraints, adding points only where needed and connecting them with tetrahedra of various sizes and orientations.

With respect to Navier-Stokes solvers, the limited capacity of computers had precluded their practical use in design for a long time. Nonetheless, a lot of work in research has helped identifying where the future lies: in the turbulence modeling specific to any type of viscous layer, viz. boundary layers, wakes, vortical flows. . . Development of direct Navier-Stokes (DNS) solvers of high accuracy, with famous names again on both sides of the Atlantic, helped the improvement of statistical turbulence

modeling which forms the basis of solvers for complex flows. On the engineering side, optimization tools began to help the design with the development of geometrical software.

### *2.5. The fifth step: multidomain, multiphysics and optimization codes*

At the turn of the century, problems embedding multiphysics within multiple computational domains became properly tractable and perhaps open to optimization on the new large parallel supercomputers. The selection of algorithms more adapted to parallelism appeared as a new challenge, taking into account the ratio of computing time to memory transfer time. From fluid-fluid interaction (viscous-inviscid for example) to fluid and other physics interaction (aeroelasticity for example) and to generalized cost functions (global efficiency with constraints in volume of fluid or weight of structural mass for example), the concept of multidomain/multiphysics optimization emerged as an accessible target for engineering. The development of Computer Aided Design (CAD) gave the opportunity to couple computed geometric variations with the industrial chain of the detailed design as existing in the design offices. The coupling of detailed design and the best of physical modeling offers the true opportunity to really introduce the work of generations of scientists into the improvement process of mechanical machines (aircraft, engines, trains, factories...). Initially all the power of mathematical optimization was limited to cases where adjoint equations of the direct continuous problems were explicitly constructed and numerically solved; but the automatic generation of the discrete adjoint equation from the discrete algorithm using the source code itself opens the way to a direct family of efficient optimizers. They use automatic discrete differentiation procedures able to build more efficient tools adjusted to complex physics with variable models which can be improved step by step.

Extreme conditions of design are still far from being tractable today, but simulations of time-dependent real physics near-extreme conditions are now open to first computations: a new step is to be built in engineering design, where a mix of fluid mechanics, solid mechanics, electromagnetism... is to be handled efficiently.

### *2.6. The next step*

Roughly, the five major steps described above match the last five decades of the development of computational mechanics after World War II. The critique of computation outputs is more and more founded on computational workshops where validation is performed by comparison with true experimental physics and cross-validation between different algorithms and physical modeling. The separate approaches followed by specialists in inviscid and viscous flows, in real gas effects, and in other disciplines can now be replaced with a unified approach. Computer simulations often lead to improved analysis of the real physics, and sometimes drastic new understanding has been reached. Nobody can now consider computational physics as rebuilding exactly the real world, but some margin of errors is commonly accepted on each design problem. Such errors are so low compared to past design without computers that major improvements have been achieved or will be achieved in the near future thanks to computational power. However, the complexity of real physics still needs further improvement of codes to significantly reduce the experimental cross-check and thus the time and cost of development of a high-technology product. From now on, computational flow mechanics can be considered as a mature discipline, but subject to on-going improvements and adjustments to each new innovative design.

### NUMERICAL CODES

In addition to the standard palette of classical aerodynamics tools such as 2-D and 3-D panel methods, lifting line theory, full potential flow, and boundary-layer, we use two advanced CFD codes, one Euler and one Navier-Stokes, which we are going to describe next. They both rely on unstructured meshes. The first one is based on a Galerkin/finite volume formulation, whereas the later one uses a Galerkin/least-squares finite element strategy.

#### 3. EULER CODE

In order to describe the numerical ingredients of Dassault Aviation's Euler code, called *Eugénie*, we start with the Euler equations which read:

$$\frac{\partial W(x, t)}{\partial t} + \nabla \cdot F(W(x, t)) = 0 \quad (1)$$

where

$$W = \begin{Bmatrix} \rho \\ \rho V \\ E \end{Bmatrix} \quad F(W) = \begin{Bmatrix} \rho V \\ \rho V \otimes V + PId_3 \\ (E + P)V \end{Bmatrix}$$

##### 3.1. Weak solutions

An hyperbolic system may not have a regular solution even for a continuous initial data. A weak solutions of the Euler equations  $W$  is such that,  $\forall \phi$  regular

$$\begin{aligned} \int_{t \geq 0} \int_{\Omega_f} W(x, t) \frac{\partial \phi}{\partial t}(x, t) dx dt + \int_{\Omega_f} \int_{t \geq 0} F(W(x, t)) \cdot \nabla \phi(x, t) dx dt \\ + \int_{\Omega_f} W^0(x) \phi(x, 0) dx - \int_{\partial \Omega_f} \int_{t \geq 0} F(W(x, t)) \cdot n \phi(x, t) d\sigma dt = 0 \end{aligned} \quad (2)$$

##### 3.2. Spatial discretization

The computational domain  $\Omega_f$  is replaced with a Finite Element triangulation  $\Omega_h$ . The triangulation  $\mathcal{T}_h$  is formed by  $N_T$  elements denoted  $T_j$ ;  $h$  is the maximal length of the side of the elements;  $N_S$  is the number of vertices in the triangulation.

$$\Omega_h = \bigcup_{j=1}^{N_T} T_j, \quad T_j \in \mathcal{T}_h$$

The spatial integration uses the *Finite Volume Galerkin* method: for each vertex  $i$  of the mesh we associate a cell  $C_i$  obtained by joining the center of gravity of the triangles containing vertex  $i$  and the mid-point of the face to which  $i$  belongs.

Figure 7 presents a cell in two dimensions.

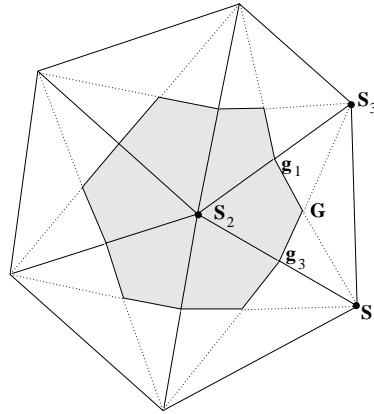


Figure 7. 2-D cell.

These cells form a partition of  $\Omega_h$ :

$$\Omega_h = \bigcup_{i=1}^{N_S} C_i$$

The test functions are taken as the characteristic functions of the cells: they evaluate to 1 inside a given cell, and to 0 outside.

In the following we will utilize the notations:

- $\mathcal{K}(i)$ : nodes neighbor of  $i$
- $\mathcal{E}(i)$ : elements which contain  $i$
- $\mathcal{F}(e)$ : faces of element  $e$
- $\mathcal{S}(e)$ : nodes of element (or face)  $e$
- $M_{ij}$ : mid-point of a edge  $ij$
- $g_i$ : center of gravity of face opposed to node  $i$
- $\partial C_{ij}$ :  $\partial C_i \cap \partial C_j$
- $n_{i,j}$ : normal of  $\partial C_{ij}$
- $n_i$ : outward normal of  $C_i$
- $\eta_{ij} = \sum_{e \in \mathcal{E}(i) \cap \mathcal{E}(j)} \int_{\partial C_{ij}} n_{i,j} d\sigma$

We can now write

$$\int_{\Omega_h} \nabla \cdot F(W) \varphi_i dx = \int_{C_i} \nabla \cdot F(W) \varphi_i dx = \int_{\partial C_i} F(W) \cdot n_i d\sigma = \sum_{j \in \mathcal{K}(i)} \int_{\partial C_{i,j}} F(W) \cdot n_{i,j} d\sigma$$

For a cell  $i$  equation (2) reads

$$\text{mes}(C_i) \frac{\partial W_i}{\partial t} + \sum_{j \in \mathcal{K}(i)} \int_{\partial C_{ij}} F(W) \cdot n_{i,j} d\sigma + \int_{\Gamma \cap \partial C_i} F(W) \cdot n_i d\sigma = 0 \quad (3)$$

### 3.3. Numerical fluxes

Let  $i$  and  $j$  be two nodes of the triangulation; the numerical flux  $\Phi_{ij}$  approximates  $\int_{\partial C_{ij}} F(W) \cdot n_i d\sigma$  and represents the flux going through  $\partial C_{ij}$ .

In a general manner,  $\Phi_{ij}$  can be expressed  $\Phi_{ij} = \Phi(W_i, W_j, \eta_{ij})$ . We can rewrite

$$\Phi_i = \sum_{j \in \mathcal{K}(i)} \Phi(W_i, W_j, \eta_{ij}) + \Phi_{i\infty} + \Phi_{iB}$$

where  $\Phi_{i\infty}$  for cell  $i$  is the flux coming from infinity and  $\Phi_{iB}$  the flux on the body.

Equation (3) becomes

$$\text{mes}(C_i) \frac{\partial W_i}{\partial t} + \sum_{j \in \mathcal{K}(i)} \Phi_{ij} + \Phi_{i\infty} + \Phi_{iB} = 0 \quad (4)$$

To calculate  $\Phi(W_i, W_j, \eta_{ij})$ , different numerical fluxes can be used. Appropriate boundary conditions define the fluxes  $\Phi_{i\infty}$  and  $\Phi_{iB}$ .

**3.3.1. Modified Lax-Wendroff flux** One of the most often used flux is based on a Lax-Wendroff flux with an extra dissipation (see Billey, 1984; Lax and Wendroff, 1960). It is a predictor-corrector second-order-accurate centered scheme:

#### Step 1: predictor

$$\widetilde{W}_T = \frac{1}{\text{mes}(T)} \left\{ \int_T W^n dv - \alpha \Delta t_T \frac{CFL_{pred}}{CFL} \int_{\partial T} F(W^n) \cdot n d\sigma \right\}$$

with:

- $\text{mes}(T)$  volume of element  $T$
- $n$  outward normal vector
- $\Delta t_T = \max_{i \in \mathcal{S}(T)} (\Delta t_i)$  where  $\Delta t_i$  is a local time step
- $\int_{\partial T} F(W^n) \cdot n d\sigma \approx \sum_{f \in \mathcal{F}(T)} F(\overline{W}^f) \text{mes}(f) n_f$ , où  $\overline{W}^f = \frac{1}{3} \sum_{i \in \mathcal{S}(f)} W_i$

#### Step 2: corrector

$$\begin{aligned} {}^c\Phi_i^T &= \beta_1 \int_T F(W) \cdot \nabla \varphi_i dv + \beta_2 \int_T F(\widetilde{W}_T) \cdot \nabla \varphi_i dv \\ &= \left[ \beta_1 \overline{F(\overline{W}^f)}^T + \beta_2 F(\widetilde{W}_T) \right] \text{mes}(T) \cdot \nabla \varphi_i|_T \end{aligned}$$

$$\text{where } \overline{F(\overline{W}^f)}^T = \frac{1}{\#\mathcal{S}(T)} \sum_{i \in \mathcal{S}(T)} F(W_i)$$

#### Step 3: viscosity

An extra numerical viscosity is added in the region of shocks which are detected using a pressure sensor introduced by Jameson and Schmidt (see Jameson and Schmidt, 1985)

$${}^v\Phi_{ij} = -\lambda_{ij}\varepsilon_{ij}(W_j - W_i)$$

with:

- $\lambda_{ij} = \frac{10 CFL * M_{ij}}{3 \Delta t_i + \Delta t_j}$
- $M$  mass matrix
- $\varepsilon_{ij} = \min(1, \chi \Delta P_{ij})$
- $\Delta P_{ij} = \frac{|P_j - P_i - \nabla P_i \cdot X_i X_j|}{|P_j + P_i - \nabla P_i \cdot X_i X_j|}$

The Lax-Wendroff flux reads

$$\Phi_i = \sum_{T \in \mathcal{E}(i)} {}^c\Phi_i^T + \sum_{j \in \mathcal{K}(i)} {}^v\Phi_{ij}$$

The constants were determined by a parametric study

$$\alpha = 1 + \sqrt{5}/2 \quad \beta_2 = 1/2\alpha \quad \beta_1 = 1 - \beta_2 \quad \chi = 0.8$$

**3.3.2. Peraire-Jameson flux** This flux is based on a centered flux with a fourth order viscosity and an extra second order viscosity in the region of shocks (see Fezoui and Stoufflet, 1989; Selmin, 1989).

We define

$$\widetilde{W} = \begin{pmatrix} \rho \\ \rho V \\ H \end{pmatrix}$$

where  $H$  is the total enthalpy ( $H = E + P$ )

Peraire's flux reads

$$\Phi(W_i, W_j, \eta_{ij}) = \eta_{ij} \cdot \frac{F_i(W) + F_j(W)}{2} - |\lambda_{ij}| \left( \varepsilon_{ij}^{(2)} (\widetilde{W}_i - \widetilde{W}_j) + \varepsilon_{ij}^{(4)} D_{ij}^{(4)} \widetilde{W} \right)$$

with

$$\lambda_{ij} = \frac{1}{2} (V_i \cdot \eta_{ij} + c_i \|\eta_{ij}\| + V_j \cdot \eta_{ij} + c_j \|\eta_{ij}\|)$$

where  $D_{ij}^{(4)} \widetilde{W}$  approximates the fourth derivative of  $\widetilde{W}$ :

$$\begin{aligned} D_{ij}^{(4)} \widetilde{W} &= \widetilde{W}_j - \widetilde{W}_i - \nabla \widetilde{W}_{ij} \cdot X_i X_j \\ &= \widetilde{W}_j - \widetilde{W}_i - \frac{1}{2} \left( \nabla \widetilde{W}_i \cdot X_i X_j + \nabla \widetilde{W}_j \cdot X_i X_j \right) \end{aligned}$$

Sensors  $\varepsilon_{ij}^{(2)}$  and  $\varepsilon_{ij}^{(4)}$  are defined using the second derivative of the pressure:

$$\varepsilon_{ij}^{(2)} = \min(1, k_2 \Delta P_{ij}) \quad \varepsilon_{ij}^{(4)} = 2 \max(0, k_4 - \delta_4 \varepsilon_{ij}^{(2)})$$

avec  $\Delta P_{ij}$  défini au paragraphe précédent.

A parametric study showed that  $k_2 = 2$ ,  $k_4 = 1/32$  and  $\delta_4 = 0.5$  give a good compromise between convergence speed and accuracy. For subsonic flows, the second order viscosity is not necessary ( $k_2 = \delta_4 = 0$ ).

*3.3.3. The Lax-Wendroff PSI scheme* The fluctuation splitting schemes were introduced by Roe in the beginning of the 80's and have been then developed since then, essentially thanks to Deconinck. In this paper, the fluctuation splitting schemes formalism is recalled. Then, the hyperbolic/elliptic decomposition of the three dimensional Euler equations is presented. This decomposition leads to an a coustic subsystem and two scalar advection equations, one of them being the entropy advection. Thanks to this decomposition, the two scalar equations are treated with the well known PSI scalar fluctuation splitting scheme, and the acoustic subsystem is treated with the Lax Wendroff matrix fluctuation splitting scheme. An additional viscous term is introduced in order to reduce the oscillatory behavior of the Lax Wendroff scheme. An implicit form leads to a robust scheme which enables computations over a large range of Mach number. This fluctuation splitting scheme, called the Lax Wendroff - PSI scheme, produces little spurious entropy, thus leading to accurate drag predictions.

## 4. NAVIER-STOKES CODE

### 4.1. Description of the code

Dassault Aviation's Navier-Stokes code, called **AETHER**, uses a finite element approach, based on a symmetric form of the equations written in terms of entropy variables. The advantages of this change of variables are numerous: in addition to the strong mathematical and numerical coherence they provide (dimensionally correct dot product, symmetric operators with positivity properties, efficient preconditioning), entropy variables yield further improvements over the usual conservation variables, in particular in the context of chemically reacting flows (see Chalot and Hughes, 1994; Chalot, Mallet and Ravachol, 1994).

The code can handle the unstructured mixture of numerous types of elements (triangles and quadrilaterals in 2-D; tetrahedra, bricks, and prisms in 3-D). In practice mostly triangular and tetrahedron meshes are used.

The code has been successfully ported on many computer architectures. It is fully vectorized and parallelized for shared or distributed memory machines using the MPI message passing library (IBM SP2, Cray T3D, Fujitsu VPP 700, SGI Origin 2000, Bull NovaScale) or native parallelization directives (NEC SX-4) (see Chalot *et al.*, 1997; Chalot *et al.*, 2001).

### 4.2. The symmetric Navier-Stokes equations

As a starting point, we consider the compressible Navier-stokes equations written in conservative form:

$$\mathbf{U}_{,t} + \mathbf{F}_{i,i}^{\text{adv}} = \mathbf{F}_{i,i}^{\text{diff}} \quad (5)$$

where  $\mathbf{U}$  is the vector of conservative variables;  $\mathbf{F}_i^{\text{adv}}$  and  $\mathbf{F}_i^{\text{diff}}$  are, respectively, the advective and the diffusive fluxes in the  $i^{\text{th}}$ -direction. Inferior commas denote partial differentiation and repeated indices indicate summation.

Equation (5) can be rewritten in quasi-linear form:

$$\mathbf{U}_{,t} + \mathbf{A}_i \mathbf{U}_{,i} = (\mathbf{K}_{ij} \mathbf{U}_{,j})_{,i} \quad (6)$$

where  $\mathbf{A}_i = \mathbf{F}_{i,i}^{\text{adv}}$  is the  $i^{\text{th}}$  advective Jacobian matrix, and  $\mathbf{K} = [\mathbf{K}_{ij}]$  is the diffusivity matrix, defined by  $\mathbf{F}_i^{\text{diff}} = \mathbf{K}_{ij} \mathbf{U}_{,j}$ . The  $\mathbf{A}_i$ 's and  $\mathbf{K}$  do not possess any particular property of symmetry or positiveness.

We now introduce a new set of variables,

$$\mathbf{V}^T = \frac{\partial \mathcal{H}}{\partial \mathbf{U}}$$

where  $\mathcal{H}$  is the generalized entropy function given by

$$\mathcal{H} = \mathcal{H}(\mathbf{U}) = -\rho s$$

and  $s$  is the thermodynamic entropy per unit mass. Under the change of variables  $\mathbf{U} \mapsto \mathbf{V}$ , (6) becomes:

$$\tilde{\mathbf{A}}_0 \mathbf{V}_{,t} + \tilde{\mathbf{A}}_i \mathbf{V}_{,i} = (\tilde{\mathbf{K}}_{ij} \mathbf{V}_{,j})_{,i} \quad (7)$$

where

$$\begin{aligned} \tilde{\mathbf{A}}_0 &= \mathbf{U}_{,\mathbf{V}} \\ \tilde{\mathbf{A}}_i &= \mathbf{A}_i \tilde{\mathbf{A}}_0 \\ \tilde{\mathbf{K}}_{ij} &= \mathbf{K}_{ij} \tilde{\mathbf{A}}_0. \end{aligned}$$

The Riemannian metric tensor  $\tilde{\mathbf{A}}_0$  is symmetric positive-definite; the  $\tilde{\mathbf{A}}_i$ 's are symmetric; and  $\tilde{\mathbf{K}} = [\tilde{\mathbf{K}}_{ij}]$  is symmetric positive-semidefinite. In view of these properties, (7) is referred to as a symmetric advective-diffusive system.

For a general divariant gas, the vector of so-called (physical) entropy variables,  $\mathbf{V}$ , reads

$$\mathbf{V} = \frac{1}{T} \begin{Bmatrix} \mu - |\mathbf{u}|^2/2 \\ \mathbf{u} \\ -1 \end{Bmatrix} \quad (8)$$

where  $\mu = e + pv - Ts$  is the chemical potential per unit mass;  $v = 1/\rho$  is the specific volume. More complex equations of state are treated in Chalot, Hughes and Shakib, 1990.

We would like to stress the formal similarity between the conservation variables  $\mathbf{U}$  and the entropy variables  $\mathbf{V}$ , which can be made more apparent if we write the conservation variables in the following form:

$$\mathbf{U} = \frac{1}{v} \begin{Bmatrix} 1 \\ \mathbf{u} \\ e + |\mathbf{u}|^2/2 \end{Bmatrix}$$

We write  $\rho$  in the form  $1/v$  to make the similarities even more apparent. The structures of both sets of variables are very close. Besides a few sign changes, the temperature is replaced with the specific volume and the internal energy with the chemical potential per unit mass. Neither set appears as a natural set of variables to use, and in any case entropy variables are not less natural than conservative variables.

Taking the dot product of (7) with the vector  $\mathbf{V}$  yields the Clausius-Duhem inequality, which constitutes the basic nonlinear stability condition for the solutions of (7). This fundamental property is inherited by appropriately defined finite element methods, such as the one described in the next section.

#### 4.3. The Galerkin/least-squares formulation

The Galerkin/least-squares (GLS) formulation introduced by Hughes and Johnson, is a full space-time finite element technique employing the discontinuous Galerkin method in time (see Shakib, Hughes

and Johan, 1991). The least-squares operator ensures good stability characteristics while retaining a high level of accuracy. The local control of the solution in the vicinity of sharp gradients is further enhanced by the use of a nonlinear discontinuity-capturing operator.

We consider the time interval  $I = ]0, T[$ , which we subdivide into  $N$  intervals  $I_n = ]t_n, t_{n+1}[$ ,  $n = 0, \dots, N - 1$ . Let  $Q_n = \Omega \times I_n$  and  $P_n = \Gamma \times I_n$  where  $\Omega$  is the spatial domain of interest, and  $\Gamma$  is its boundary. In turn, the space-time ‘‘slab’’  $Q_n$  is tiled by  $(n_{el})_n$  elements  $Q_n^e$ . Consequently, the Galerkin/least-squares variational problem can be stated as

Within each  $Q_n$ ,  $n = 0, \dots, N - 1$ , find  $\mathbf{V}^h \in \mathcal{S}_n^h$  (trial function space), such that for all  $\mathbf{W}^h \in \mathcal{V}_n^h$  (weighting function space), the following equation holds:

$$\begin{aligned} & \int_{Q_n} \left( - \mathbf{W}_{,t}^h \cdot \mathbf{U}(\mathbf{V}^h) - \mathbf{W}_{,i}^h \cdot \mathbf{F}_i^{\text{adv}}(\mathbf{V}^h) + \mathbf{W}_{,i}^h \cdot \widetilde{\mathbf{K}}_{ij} \mathbf{V}_{,j}^h \right) dQ \\ & + \int_{\Omega} \left( \mathbf{W}^h(t_{n+1}^-) \cdot \mathbf{U}(\mathbf{V}^h(t_{n+1}^-)) - \mathbf{W}^h(t_n^+) \cdot \mathbf{U}(\mathbf{V}^h(t_n^+)) \right) d\Omega \\ & + \sum_{e=1}^{(n_{el})_n} \int_{Q_n^e} (\mathcal{L}\mathbf{W}^h) \cdot \boldsymbol{\tau}(\mathcal{L}\mathbf{V}^h) dQ \\ & + \sum_{e=1}^{(n_{el})_n} \int_{Q_n^e} \nu^h g^{ij} \mathbf{W}_{,i}^h \cdot \widetilde{\mathbf{A}}_0 \mathbf{V}_{,j}^h dQ \\ & = \int_{P_n} \mathbf{W}^h \cdot \left( - \mathbf{F}_i^{\text{adv}}(\mathbf{V}^h) + \mathbf{F}_i^{\text{diff}}(\mathbf{V}^h) \right) n_i dP. \end{aligned} \quad (9)$$

The first and last integrals represent the Galerkin formulation written in integrated-by-parts form. The solution space consists of piecewise polynomials which are continuous in space, but are discontinuous across time slabs. Continuity in time is weakly enforced by the second integral in (9), which contributes to the jump condition between two contiguous slabs, with

$$\mathbf{Z}^h(t_n^\pm) = \lim_{\varepsilon \rightarrow 0^\pm} \mathbf{Z}^h(t_n + \varepsilon).$$

The third integral constitutes the least-squares operator where  $\mathcal{L}$  is defined as

$$\mathcal{L} = \widetilde{\mathbf{A}}_0 \frac{\partial}{\partial t} + \widetilde{\mathbf{A}}_i \frac{\partial}{\partial x_i} - \frac{\partial}{\partial x_i} (\widetilde{\mathbf{K}}_{ij} \frac{\partial}{\partial x_j}).$$

$\boldsymbol{\tau}$  is a symmetric matrix for which definitions can be found in Shakib, Hughes and Johan (1991). The fourth integral is the nonlinear discontinuity-capturing operator, which is designed to control oscillations about discontinuities, without upsetting higher-order accuracy in smooth regions.  $g^{ij}$  is the contravariant metric tensor defined by

$$[g^{ij}] = [\boldsymbol{\xi}_{,i} \cdot \boldsymbol{\xi}_{,j}]^{-1}$$

where  $\boldsymbol{\xi} = \boldsymbol{\xi}(\mathbf{x})$  is the inverse isoparametric element mapping, and  $\nu^h$  is a scalar-valued homogeneous function of the residual  $\mathcal{L}\mathbf{V}^h$ . The discontinuity capturing factor  $\nu^h$  used in the present work is an extension of that introduced by Hughes, Mallet, and Shakib (see Hughes and Mallet, 1986; Shakib, Hughes and Johan, 1991).

A key ingredient to the formulation is its consistency: the exact solution of (5) satisfies the variational formulation (9). This constitutes an essential property in order to attain higher-order spatial convergence.

#### 4.4. Linear solver and residual evaluations

Convergence to steady state of the compressible Navier Stokes equations is achieved through a fully-implicit iterative time-marching procedure based on the GMRES algorithm (see Shakib, Hughes and Johan, 1989).

A low-storage extension based solely on residual evaluations was developed by Johan, Hughes and Shakib (1991). It reveals particularly adapted to parallel processing, where the linear solver often constitutes a painful bottleneck.

This algorithm has proven extremely efficient on many scalar or vector architectures (cf. Chalot *et al.*, 1997; Johan, 1992).

#### 4.5. Equations of state

Different equations of state for the gas mixture are available. Most calculations are performed using the *calorically perfect gas* assumption, for which the specific heats  $c_p$  and  $c_v$  are constant. Various models for cases where the gas departs from the calorically perfect gas assumption are implemented. First, the *thermally perfect gas* model takes into account the nonlinear behavior of internal energy modes, such as vibration, with respect to temperature. Calculations where the temperature goes high enough to enable the chemical dissociation and recombination of gas molecules can be handled using a 5-species ( $N_2$ ,  $O_2$ , NO, N, and O) *thermochemical equilibrium* model for air. Such a model assumes that chemical kinetics is negligible compared to the dynamic of the flow. In scarce occasions when this assumption breaks down, one can use a model based on a *mixture of thermally perfect gases in thermochemical nonequilibrium*. This last model can deal with any number of species interacting in any number of chemical reactions. Thermal nonequilibrium effects which describe the exchanges between molecular internal energy modes are also taken into account by this model.

Transport coefficients are theoretically derived by means of statistical mechanics. In particular, we use the full multi-component model to describe mass diffusion. This is the only model which can be shown to guarantee both mass conservation and the correct entropy production. Simpler model such as Fick's law simply cannot be used beyond a two-species mixture without seriously degrading the entropy balance. This model is used with an appropriate set of chemical species to compute jet flows (see section 13.3).

This crucial ingredient appears in the symmetrization process, which again shows the high level of consistency between mathematics, physics and numerics in the design of AETHER.

## 5. REYNOLDS-AVERAGED TURBULENCE MODELING

Turbulence modeling is one of the key elements in Computational Fluid Dynamics. In the early 80's, the use of unstructured finite element methods led to the computation of a full aircraft using a compressible potential solver (Glowinski, 1984). Since then, both numerical methods and computers have evolved, and today the same type of computation can be performed using a compressible Navier Stokes solver (Chalot *et al.*, 1993). In the meantime, few improvements were made to the work of Prandtl, Taylor, von Karman. . . The turbulence model is still the weak point of viscous calculations at high Reynolds number. The design of a good turbulence model is not a trivial task; an enormous amount of information is required to completely describe a turbulent flow since turbulence is inherently three dimensional and time dependent.

In principle, the time dependent, three dimensional Navier Stokes equations contain all the physics of a given turbulent flow. One of the difficulties arises from the fact that the largest scales are many orders of magnitude larger than the smallest scales. To make an accurate simulation of a turbulent flow, all physically relevant scales must be resolved leading to a number of grid points in the range of  $Re^{9/4}$ . The direct numerical simulation of a full aircraft at cruise speed is not feasible with today's fastest computers. Thus, the demand for turbulence modeling will remain strong for some years to come.

Turbulence is characterized by random fluctuations thus obviating a deterministic approach to the modeling problem. The statistical approach is then preferred. Averaging operations lead to statistical correlations in the Navier Stokes equations that need to be modeled. Several levels of modelization can be introduced. We will segregate them into two categories: models using the Boussinesq assumption (Boussinesq, 1877) and second moment closure models. For the latter, each component of the Reynolds stress tensor is described by a governing equation. This framework is the natural one in which non local and historic effects are incorporated. For three dimensional flows, a second moment closure introduces seven equations (more than the number of equations needed to describe the mean flow!) and an even larger number of closure coefficients. . . Models which rely on the Boussinesq assumption mimics the dissipative nature of turbulent flows through an eddy viscosity. Such models may not accommodate complex effects such as streamline curvature or rigid body rotation, but they keep the number of extra equations describing the turbulent field (and the number of closure coefficients) reasonable. In the balance of capturing the essence of the relevant physics and introducing the minimum amount of complexity, we chose the second option. Overkill is often accompanied by unexpected difficulties that in CFD almost always translates into numerical problems.

A turbulence model has to be decided upon to compute the eddy viscosity. Here again, we have to choose among several families of model: algebraic models, one equation models and two equation models. The implementation of an algebraic model (Baldwin and Lomax, 1978; Cebecchi and Smith, 1974. . .) in a Navier Stokes solver using unstructured grids is not straightforward and was judged not to be worth the effort. With one equation models, the eddy viscosity depends on flow history, then such models are more physically realistic. These models, such as Baldwin and Barth (1991) or Spalart and Allmaras (1994) perform very well for wall bounded flows, but the need to specify a turbulence length scale still remains. The determination of the length scale can be tricky in shear layer flows such as mixing layers or wakes. A two equation model alleviates the need for an external prescription of a turbulent length scale and should therefore be applicable to a wider class of flows. There are many different two equation models:  $k - \varepsilon$ ,  $k - \omega$ ,  $k - \ell$ ,  $k - k\ell$ , to name a few. The variety of models underscores the lack of generality of any given one which in turn implies that an industrial code must carry an array of models. To facilitate the introduction of a new turbulence model the mean flow solver and the turbulence solver are segregated; in addition this strategy allows to apply a specific numerical

treatment for the turbulence equations.

The extra equation needed for the turbulence models can be re-casted in the general form

$$\frac{\partial \rho s_i}{\partial t} + \nabla \cdot (\rho u s_i) - \nabla \cdot \left( \left( \mu + \frac{\mu_t}{\sigma_{s_i}} \right) \nabla s_i \right) = H_i$$

these equations are convection diffusion equation coupled through their source term. The turbulence quantities are positive, therefore one is seeking a scheme which enforces this constraint. The positivity of the turbulence variables is achieved by the combination of two main features: the use of a monotone discrete advective scheme and the time discretization of the source terms. First we will investigate the issue of the spatial discretization.

### 5.1. Monotone scheme for the turbulence equations

Consider the model problem

$$a \cdot \nabla \phi - D \Delta \phi = 0$$

The basic choice to enforce the monotony of the discrete advection diffusion equation would be to use a first order upwind scheme. In so doing, the sharp gradients are completely smeared out. It is thus necessary to implement a scheme of higher order accuracy. The scheme chosen is the one advocated by Struijs, Roe and Deconinck (1991). The main advantages of the scheme, along with its monotonicity and its low diffusion, are its compact stencil and the fact that all the necessary evaluations are performed element by element yielding an easy implementation in a Finite Element framework as well as a straightforward vectorization and parallelization. We must point out that this advection scheme is *non linear*. Such an elaborate treatment is needed in order to calibrate the accuracy of the modeling of the turbulence effects. With too coarse a numerical treatment such as a first order upwinding it is impossible to analyze the validity of any turbulence model. We want to solve this problem on *unstructured meshes* using a scheme that verifies a discrete maximum principle to enforce the positivity of the turbulence variables. Another requisite is to have a scheme with a compact stencil (for parallelization purposes).

The method of choice is a *distributive scheme* introduced by Deconinck *et al.* (1993). We present a series of distributive schemes: first, a first order accurate monotone scheme, then a second order accurate non monotone scheme and finally a second order accurate monotone scheme based upon the previous schemes using a limiting technique.

- first order scheme: N scheme

The domain of resolution  $\Omega$  is divided into triangles (for the sake of simplicity we will restrict ourself to the 2-D case, the extension to 3-D is straightforward), the discrete solution  $\phi_h$  can be written

$$\phi_h = \sum_{i=1}^3 \phi_i N_i$$

where  $N_i$  are the piecewise linear finite element shape functions. We define  $F^e$ , the advective flux on the element

$$F^e = \int_{\Omega_e} (a \cdot \nabla \phi_h) d\Omega = |\Omega_e| \sum_{i=1}^3 \phi_i a \cdot \nabla N_i = |\Omega_e| \sum_{i=1}^3 \phi_i k_i$$

where

$$k_i = a \cdot \nabla N_i$$

The flux is distributed depending on the sign of  $k_i$ :

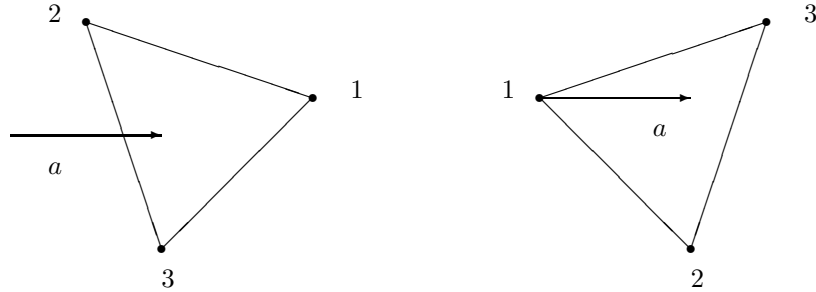


Figure 8. Schematics of flux distribution.

If  $k_i > 0$ , then  $a$  enter the element by the face opposed to node  $i$  (left case in Figure 8) and all the flux is put to this node. If the case  $k_i < 0$  (right case in Figure 8) the flux needs to be distributed between the two downstream nodes. The discrete flux is then for node  $i$

$$F_i^e = |\Omega_e| k_i^+ (\phi_i + \frac{F^e / |\Omega_e|}{\sum_{j=1}^3 k_j^+})$$

where

$$k_i^+ = \max(0, k_i) \text{ and } k_i^- = \min(0, k_i)$$

$F_i^e$  can be written using a matrix form as

$$F_i^e = \sum_{j=1}^3 A_{ij}^{\text{adv}} \phi_j$$

with

$$A_{ij}^{\text{adv}} = |\Omega_e| k_i^+ (\delta_{ij} + \frac{k_j^-}{\sum_{l=1}^3 k_l^+})$$

It is easy to verify that the matrix  $A_{ij}$  is such that

$$\begin{aligned} A_{ii} &\geq 0 \\ A_{ij} &\leq 0 \text{ if } i \neq j \end{aligned}$$

The N-scheme is monotone but only first order accurate.

- **second order scheme: LDA scheme**

For the scheme the numerical flux is defined by:

$$F_i^e = |\Omega_e| \frac{\max(0, k_i)}{\sum_j \max(0, k_j)} \sum_j k_j \phi_j$$

This scheme is second order accurate, but since it is a linear scheme and preserves the linearity of a solution is not a monotone scheme.

- second order monotone scheme: PSI scheme

A monotone second order accurate scheme can be constructed from the previous two schemes using a slope limiting technique as proposed by Abgrall (1999). The new numerical flux is defined by:

$$F_i^e = \ell F_i^{eN} + (1 - \ell) F_i^{eLDA}$$

where  $F_i^{eN}$  and  $F_i^{eLDA}$  are respectively the numerical fluxes given by the N-scheme and the LDA-scheme.

Once again, the choice of  $\ell$  depends on the sign of  $k_i$  and for that there are two situations:

- case 1:  $k_1 > 0$ ,  $k_2 \leq 0$  and  $k_3 \leq 0$  we choose

$$\begin{aligned} F_1^{eN} &= F_1^{eLDA} = |\Omega_e| \sum_j k_j \phi_j \\ F_2^{eN} &= F_2^{eLDA} = 0 \\ F_3^{eN} &= F_3^{eLDA} = 0 \end{aligned}$$

then any  $\ell$  works, and we choose  $\ell = 1$ .

- case 2:  $k_1 > 0$ ,  $k_2 < 0$  and  $k_3 \leq 0$  we choose

$$\begin{aligned} F_1^e &= \ell F_1^{eN} + (1 - \ell) F_1^{eLDA} = \left( \ell + (1 - \ell) \frac{F_1^{eLDA}}{F_1^{eN}} \right) F_1^{eN} \\ F_2^e &= \ell F_2^{eN} + (1 - \ell) F_2^{eLDA} = \left( \ell + (1 - \ell) \frac{F_2^{eLDA}}{F_2^{eN}} \right) F_2^{eN} \\ F_3^{eN} &= F_3^{eLDA} = 0 \end{aligned}$$

Since the N-scheme is monotone, a sufficient condition for the PSI-scheme to be monotone is to have

$$\left( \ell + (1 - \ell) \frac{F_i^{eLDA}}{F_i^{eN}} \right) \geq 0$$

Let define

$$r_i = \frac{F_i^{eLDA}}{F_i^{eN}}$$

then if we choose

$$\ell = \max(\ell(r_1), \ell(r_2))$$

with

$$\ell(r) = \begin{cases} \frac{r}{1-r}, & r < 0 \\ 0, & \text{else} \end{cases}$$

we obtain a monotone PSI-scheme.

It is worth noting that in the two target case (case 2 above) the PSI-scheme is a **non linear** scheme (even for a linear equation!) since the slope limiter  $\ell$  depends on the solution  $\phi$ . We will see in the time discretization paragraph how to deal with that.

### 5.2. Time discretization and linearization of the source terms

Let consider the one dimensional model problem  $\frac{d\phi}{dt} = S\phi$  where  $S$  is a constant. The solution is  $\phi(t) = \phi(0) \exp(-St)$ . The solution remains positive with a positive initial condition.

We are going to investigate which scheme: implicit or explicit is best suited to enforce the positivity of the discrete solution.

- implicit scheme:  $\frac{\phi^{n+1} - \phi^n}{\Delta t} = S\phi^{n+1}$  which leads to:  $\phi^{n+1} = \frac{1}{1 - \Delta t S} \phi^n$  If  $S > 0$  the positivity constraints limits the time step  $\Delta t < \frac{1}{S}$
- explicit scheme:  $\frac{\phi^{n+1} - \phi^n}{\Delta t} = S\phi^n$  which leads to:  $\phi^{n+1} = 1 + \Delta t S \phi^n$  If  $S < 0$  the positivity constraints limits the time step  $\Delta t < -\frac{1}{S}$

For this problem, depending on the sign of  $S$  an implicit or an explicit scheme is preferred. We will use this remark for the time discretization of the turbulence equations.

For the  $k - \epsilon$  model the source terms read

$$H_k = \mu_t P - \frac{2}{3} \rho k \nabla \cdot u - \rho \epsilon$$

and

$$H_\epsilon = C_1 \frac{\epsilon}{k} \mu_t P - \frac{2}{3} C_1 \rho \epsilon \nabla \cdot u - \rho C_2 \frac{\epsilon^2}{k}$$

It is clear that the source terms can be written as  $H_i = H_i^+ - H_i^-$ , with both terms  $H_i^+$  and  $H_i^-$  positive. The time discretization applies as follows  $H_i^+$  is treated explicitly and  $H_i^-$  semi-implicitly (Chalot, Mallet and Ravachol, 1994). The final time discretization for the  $k - \epsilon$  model is

$$H_k = \mu_t^n P^n \frac{2}{3} \rho^n \nabla \cdot u^n k^{n+1} - \rho^n \frac{\epsilon^n}{k^n} k^{n+1}$$

and

$$H_\epsilon = C_1 \frac{\epsilon^n}{k^n} \mu_t^n P^n - \frac{2}{3} C_1 \rho^n \nabla \cdot u^n \epsilon^{n+1} - \rho C_2 \frac{\epsilon^n}{k^n} \epsilon^{n+1}$$

We present now on the generic form of the turbulence equations the practical implementation of the PSI-scheme.

$$\frac{\rho^n (s_i^{n+1} - s_i^n)}{\Delta t} + \nabla \cdot (\rho^n u^n s_i^{n+1}) - \nabla \cdot \left( \left( \mu + \frac{\mu_t^n}{\sigma_{s_i}} \right) \nabla s_i^{n+1} \right) = H_i^{+n} - H_i^{-n} \frac{s_i^{n+1}}{s_i^n}$$

With  $\delta s_i = s_i^{n+1} - s_i^n$  the above equation can be written as:

$$\begin{aligned} \frac{\rho^n \delta s_i}{\Delta t} + H_i^{-n} \frac{\delta s_i}{s_i^n} + \nabla \cdot (\rho^n u^n \delta s_i) - \nabla \cdot \left( \left( \mu + \frac{\mu_t^n}{\sigma_{s_i}} \right) \nabla \delta s_i \right) = \\ H_i^{+n} - H_i^{-n} - \nabla \cdot (\rho^n u^n s_i^n) + \nabla \cdot \left( \left( \mu + \frac{\mu_t^n}{\sigma_{s_i}} \right) \nabla s_i^n \right) \end{aligned}$$

The N-scheme is used for the convective term of the left hand side of the equation, the PSI-scheme is used for the right hand side of the equation. We notice that the non linearity of the PSI-scheme can be easily handled since the right hand side only involves values determined at the previous time step.

### 5.3. Beyond the Boussinesq assumption

In the eddy viscosity model, the Reynolds stresses and the shear stresses are parallel. In the case of high swirl flows, it is sometimes necessary to circumvent this hypothesis and take into account some anisotropic effects. This can be achieved either by a full Reynolds Stress model or through an Algebraic Reynolds Stress model (Rodi, 1976; Gatski and Speziale, 1992). We present here a version of an Explicit Algebraic Reynolds Stress Model (EARSM). This model introduced by Wallin *et al.* (1998) is a simplified version of a full Reynolds stress transport model and due to its explicit formulation does not exhibit the usual numerical stiffness of classical Algebraic Stress Models. The EARSM model is built onto a two equation turbulence model. The derivation is presented in the case of the  $k - \epsilon$  model.

The anisotropy tensor is defined by:

$$a_{ij} = \frac{\overline{\rho u'_i u'_j}}{\bar{\rho} k} - \frac{2}{3} \delta_{ij}$$

Under a local equilibrium hypothesis, the sum of the convective and diffusive terms can be neglected in the Reynolds stress transports equations. An implicit relation can then be written for the anisotropic part of the Reynolds stresses:

$$\frac{\overline{\rho u'_i u'_j}}{\bar{\rho} k} (\mathcal{P} - \bar{\rho} \epsilon) = P_{ij} - \bar{\rho} \epsilon_{ij} + \Pi_{ij}$$

The turbulent kinetic energy  $k$  and its dissipation  $\epsilon$  are determined using the standard  $k - \epsilon$  model. In the model, the production terms  $\mathcal{P}$  et  $P_{ij}$  are exactly computed by

$$\mathcal{P} = -\overline{\rho u'_i u'_j} \langle u_i \rangle_{,j}$$

and

$$P_{ij} = -\overline{\rho u'_i u'_k} \langle u_j \rangle_{,k} - \overline{\rho u'_j u'_k} \langle u_i \rangle_{,k}$$

The dissipation tensor  $\epsilon_{ij}$  and the pressure term  $\Pi_{ij}$  need to be modelled. We assume the dissipation tensor to be isotropic

$$\epsilon_{ij} = \frac{2}{3} \epsilon \delta_{ij}$$

Classically, the pressure term is split into a “slow” and a “rapid” part. The slow part is computed using Rotta’s model

$$\Pi_{ij}^{\text{slow}} = -C_1 \frac{\epsilon}{k} (\overline{\rho u'_i u'_j} - \frac{2}{3} \bar{\rho} k \delta_{ij}) = -C_1 \bar{\rho} \epsilon a_{ij}$$

for the “rapid” term, we use the Launder, Reece and Rodi model (1975)

$$\begin{aligned} \Pi_{ij}^{\text{rapid}} = & -\frac{C_2 + 8}{11} (P_{ij} - \frac{2}{3} \mathcal{P} \delta_{ij}) - \frac{30C_2 - 2}{55} \bar{\rho} k (\langle u_i \rangle_{,j} + \langle u_j \rangle_{,i} - \frac{2}{3} \langle u_l \rangle_{,l} \delta_{ij}) \\ & - \frac{8C_2 - 2}{11} (D_{ij} - \frac{2}{3} \mathcal{P} \delta_{ij}) \end{aligned}$$

with

$$D_{ij} = \overline{\rho u'_i u'_k} \langle u_k \rangle_{,j} - \overline{\rho u'_j u'_k} \langle u_k \rangle_{,i}$$

then, the *implicit* relation for the anisotropic part of the Reynolds stress tensor reads

$$\begin{aligned} (C_1 - 1 - \frac{6C_2 + 4}{11} \tau \langle u_k \rangle_{,k} - \text{tr}(aS))a = & -\frac{8}{15} S + \frac{7C_2 + 1}{11} (a\Omega - \Omega a) \\ & - \frac{5 - 9C_2}{11} (aS + Sa - \frac{2}{3} \text{tr}(aS)\text{Id}) \end{aligned}$$

in the above expression, the mean strain and rotation tensors are normalized using the turbulence time scale  $\tau = \frac{\epsilon}{k}$  and are defined by:

$$S_{ij} = \frac{\tau}{2} (\langle u_i \rangle_{,j} + \langle u_j \rangle_{,i} - \frac{2}{3} \langle u_l \rangle_{,l} \delta_{ij})$$

$$\Omega_{ij} = \frac{\tau}{2} (\langle u_i \rangle_{,j} - \langle u_j \rangle_{,i})$$

The equation for the Reynolds stresses is simplified if one assumes that  $C_2 = 5/9$ . We obtain

$$(C_1 - 1 - \frac{2}{3} \tau \langle u_k \rangle_{,k} - \text{tr}(aS))a = -\frac{8}{15}S + \frac{4}{9}(a\Omega - \Omega a)$$

$C_1$  keeps its classical value:  $C_1 = 1.8$ .

Standard explicit algebraic stress models (Gatski and Speziale, 1992) assume that the term

$$\frac{\mathcal{P}}{\bar{\rho}\epsilon} = -\frac{2}{3} \tau \langle u_k \rangle_{,k} - \text{tr}(aS)$$

is constant. An extension proposed by Wallin *et al.* (1998) get rid of this strong hypothesis

Using tensorial analysis, the anisotropy tensor can be written as:

$$a_{ij} = \sum_{l=1}^{10} \beta_l T_{ij}^l$$

where  $T_{ij}^l$  are function of the tensorial invariants of  $S$  and  $\Omega$ . These invariants read

$$\text{II}_S = \text{tr}(S^2), \text{II}_\Omega = \text{tr}(\Omega^2), \text{III}_S = \text{tr}(S^3), \text{IV} = \text{tr}(S\Omega^2), V = \text{tr}(S^2\Omega^2)$$

with

$$(S^2)_{ij} = S_{ik}S_{kj}, S^3 = S^2S = SS^2$$

$$\begin{aligned} T^1 &= S & T^3 &= \Omega^2 - \frac{1}{3}\text{II}_\Omega \text{Id} & T^4 &= S\Omega - \Omega S \\ T^2 &= S^2 - \frac{2}{3}\text{II}_S \text{Id} & T^6 &= S\Omega^2 + \Omega^2S - \frac{2}{3}\text{IV} \text{Id} & T^9 &= \Omega S\Omega^2 - \Omega^2 S\Omega \\ T^5 &= S^2\Omega - \Omega S^2 & T^8 &= S\Omega S^2 - S^2\Omega S & & \\ T^7 &= S^2\Omega^2 + \Omega^2 S^2 - \frac{2}{3}V \text{Id} & & & & \\ T^{10} &= \Omega S^2\Omega^2 - \Omega^2 S^2\Omega & & & & \end{aligned}$$

We only present the detailed calculation for 2-D flows, the generalization to 3-D flows just involves more tensor invariants. For a 2-D flow, only  $T^1, T^2, T^4$  and  $\text{II}_S, \text{II}_\Omega$  remain. To close the problem, the  $\beta_l$  need to be determined

The method is as follows: let introduce an auxilliary variable  $N$

$$N = C'_1 - \frac{9}{4} \text{tr}(aS)$$

with

$$C'_1 = \frac{9}{4} (C_1 - 1 - \frac{2}{3} \tau \langle u_k \rangle_{,k})$$

The equation for the anisotropy tensor can be written as

$$Na = -\frac{6}{5}S + (a\Omega - \Omega a)$$

If we assume  $N$  known, it is possible to compute the  $\beta_l$  coefficient. In 2-D, there are only 2 non zero  $\beta_l$  which read

$$\beta_1 = -\frac{6}{5} \frac{N}{N^2 - 2\Pi_\Omega} \quad \beta_4 = -\frac{6}{5} \frac{1}{N^2 - 2\Pi_\Omega}$$

$N$  is solution of a non linear equation, which is for a 2-D flow

$$N = \frac{C'_1}{3} + (P_1 + \sqrt{P_2})^{1/3} + (P_1 - \sqrt{P_2})^{1/3}$$

with

$$P_1 = \left( \frac{C'_1{}^2}{27} + \frac{9}{20} \Pi_S - \frac{2}{3} \Pi_\Omega \right) C'_1$$

and

$$P_2 = P_1^2 - \left( \frac{C'_1{}^2}{9} + \frac{9}{10} \Pi_S + \frac{2}{3} \Pi_\Omega \right)^3$$

The Reynolds stress tensor arising from the EARSM model can be split into two parts: a part described by an turbulent viscosity and a purely anisotropic part.

$$\overline{\rho u'_i u'_j} = -\mu_t (\langle u_i \rangle_{,j} + \langle u_j \rangle_{,i} - \frac{2}{3} \langle u_k \rangle_{,k} \delta_{ij}) + \frac{2}{3} \bar{\rho} k \delta_{ij} + \bar{\rho} k a_{ij}^{\text{ani}}$$

This interesting feature of the EARSM model is very useful from a numerical point of view. The terms associated with the eddy viscosity are treated in the standard implicit manner in the Navier-Stokes solver and the anisotropy terms, which can be viewed as corrections, are treated explicitly.

#### 5.4. Conclusion

The focus of this section was on classical turbulence models and some improvements incorporated into them for use in engineering applications. The motto was to use the minimum amount of complexity while capturing the essence of the relevant physics. Nevertheless, a model devised / improved in this spirit does not pretend to apply universally to all turbulent flows. There is no guarantee that such a model is accurate beyond its establish database. Thus, the end user must be aware of the model limitations and analyze the solution accordingly. Furthermore, the Reynolds Averaged Models have serious theoretical shortcomings in the case of unsteady flows. The Large Eddy Simulation (L.E.S) can nowadays be viewed as a potential replacement for Reynolds Averaged models in complex flow situations (unsteady flows, large separations, ...) In LES computations, the energy containing eddies are actually computed, only the small-scale turbulence has to be modeled. This turbulence is more nearly isotropic and has universal characteristics; it is thus more amenable to modeling.

## 6. LARGE EDDY SIMULATION

The Large Eddy Simulation (LES) can be considered as a mid-point between the RANS approach where all the turbulent scales are modelled and the DNS where all the turbulent scales are computed. In an LES simulation, only the largest scales, the scales that contains most of the energy, are computed, the effect of the smallest scales are modelled. The smallest scale have a more predictable behavior (inertial range in the energy spectrum) and should be easier to model.

We present here the LES extension of the *industrial* RANS solver used at Dassault Aviation.

The starting point of an LES formulation is to be able to separate the large scales and the small scales. This is usually done by applying a filter to the Navier-Stokes equations. Any variable  $F$  can be decomposed into a filtered variable  $\overline{F}$  and a fluctuating part  $F'$ . The filtered variable is defined in the physical space as a convolution product

$$\overline{F(x)} = \int_{\Omega} G(x - x^*)F(x)dx^*$$

where  $G$  is the filter applied to the instantaneous variable  $F$ . For LES simulation, the filters usually used are the box filter, the gaussian filter and the sharp cut-off filter. This filter is usually used for spectral simulation.

It is important to remark, that unlike in the RANS approach we generally have  $\overline{\overline{F}} \neq \overline{F}$  and  $\overline{F'} \neq 0$ .

Moreover, the fact that we actually solve the *discretized* Navier-Stokes equation can be viewed as a filtering operation. For example, on a regular mesh with a grid size  $\Delta$ , the smallest scale that can be computed is  $2\Delta$  meaning that the greatest wave number computable on this grid is  $k_c = \frac{\pi}{\Delta}$

Futhermore, we assume that the filter and the derivatives commute:

$$\frac{\partial \overline{F}}{\partial t} = \overline{\frac{\partial F}{\partial t}} \quad \frac{\partial \overline{F}}{\partial x_i} = \overline{\frac{\partial F}{\partial x_i}}$$

This is not true on an irregular mesh. Ghosal and Moin (1995) have shown that this commutation introduces an error equivalent to the truncation error of a second order accurate scheme.

### 6.1. Subgrid scale model

When the filter is applied to the Navier-Stokes equations, the equation for the filtered quantities involves correlations of the unresolved scales that need to be modeled. case.

Just like in the RANS case, then unknown terms are modeled using an extra viscosity, *the subgrid scale* viscosity. The equations to be solved have formally the same expression as the RANS equations. The difference between the LES and RANS methods are

- The LES method requires to solve the *unsteady 3-D* Navier-Stokes equations. The RANS method applies to 2-D or 3-D steady or unsteady equations.
- the extra viscosity is given by a subgrid scale model which is more general than a classic turbulence model.

The subgrid scale model retained here is the Smagorinsky model, the extra viscosity is

$$\nu_t = (C_s \Delta)^2 \sqrt{\frac{1}{2} S_{ij} S_{ij}}$$

where  $S = \nabla \overline{u} + \nabla^t \overline{u} - \frac{2}{3} \nabla \cdot \overline{u} I$ ,  $\Delta$  is the size of the filter which is taken here as  $\Delta = |\Omega_e|^{1/3}$ ,  $|\Omega_e|$  being the volume of the element.

The constant  $C_s$  can be derived for an homogeneous turbulence following a Kolmogorov cascade (Lilly, 1987)

$$C_s = \frac{1}{\pi} \left( \frac{3C_k}{2} \right)^{-3/4} \approx 0.18$$

where  $C_k = 1.4$  is the kolmogorov constant.

### 6.2. Improvement to the Smagorinsky model

We consider here the flow of two layers of fluid with respective speed of 1 and  $-1$ . The transition to turbulence takes place through a Kelvin Helmholtz instability. The first unstable mode is a 2-D mode which leads to big 2-D structures, then a 3-D unstable mode triggers the transition to turbulence. The effect we are interested in is to capture the vortex stretching, typical of a 3-D turbulence, that can be measured here by the streamwise component of the vorticity.

This temporal simulation is performed on a box with periodic boundary conditions in the streamwise direction. The initial condition for the velocity is an hyperbolic tangent profile above which a white noise of amplitude  $10^{-3}$  is added. The convective Mach number for this computation is  $M_c = 0.4$

In Figure 9 we present an iso-surface of the streamwise vorticity obtained with the GLS formulation and the Smagorinsky model. The level of streamwise vorticity is very low and there is almost no 3-D activity in this flow. The same computation redone with the Galerkin formulation and the Smagorinsky model gives exactly the same results and thus reveals the culprit: for a shear flow, the Smagorinsky model is too dissipative.

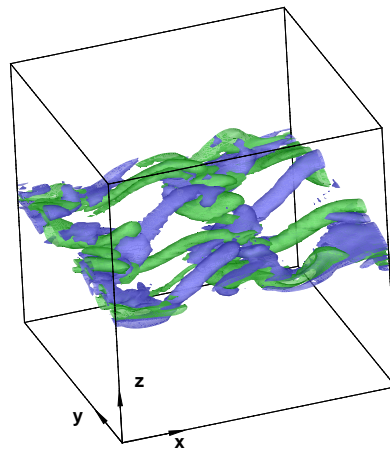
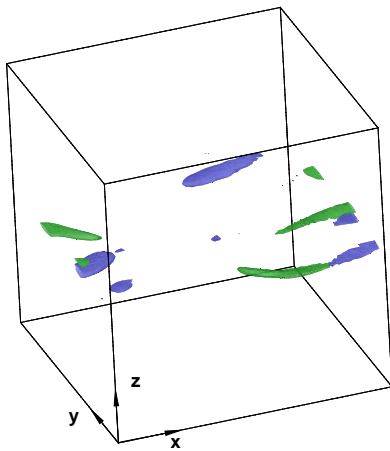


Figure 9. Smagorinsky model: Streamwise vorticity.

Figure 10. Selective model: Streamwise vorticity.

The Smagorinsky model depends upon the shear stress of the flow and thus is too dissipative for a flow with a mean shear. An elegant manner to correct this is to look at the physics of the flow. We are interested by 3-D turbulence, thus we should tell the subgrid model to be active only when the flow is really 3-D. A fix proposed by David (1995) for a different subgrid scale model is applied here to

the Smagorinsky model: at a given point  $A$  we compute the local vorticity  $\omega_A$  and the average of the vorticity at the points around  $A$   $\overline{\omega_A}$  the 3-D character of the flow is then deduced from the angle  $\alpha$  between the two vectors  $\omega_A$  and  $\overline{\omega_A}$ . Following David the flow is declared to be 2-D if  $\alpha < 20^\circ$  and then not turbulent. The *selective* Smagorinsky model derived from this procedure reads

$$\nu_t = H\nu_t^{\text{Smag}}$$

with

$$H = \begin{cases} 1 & \text{if } \alpha \geq 20^\circ \\ 0 & \text{otherwise} \end{cases}$$

The selection function  $H$  tries to characterize the three dimensional behavior of the flow and is based on an estimate angle of the local vorticity vector and the average vorticity vector in the neighborhood. A sharp cut-off is used between the two regimes: the subgrid viscosity is set to zero where the three dimensionality criterium is not satisfied and kept to the value given by the Smagorinsky model otherwise.

This model used with the GLS formulation leads to a real 3-D flow as shown in Figure 10. The quality of the results was confirmed by comparison with other LES results at higher resolution and the statistics obtained compared very well with the published results.

The final strategy retained for LES simulation of compressible flows is: Galerkin/Least-Square formulation and selective Smagorinsky model, as detailed in Chalot *et al.* (1998).

### 6.3. LES computation of mixing enhancement

The experimental setup is summerized in Figure 11 (see also Chalot *et al.*, 1999). It consists of a supersonic and a subsonic flow separated by a splitter plate; downstream of the splitter plate there is a mixing device. The Mach numbers in the mixing layer are 0.3 for the subsonic side and 1.4 for the supersonic side. The mixing device consists of a supersonic micro-jet that impinges the subsonic side of the mixing layer.

In the computations, the wind tunnel are removed; the lower and upper wall are only accounted for through the pressure and periodic boundary conditions are used in the spanwise direction. These simplifications do not impair the significance of the results since we are mostly concerned with the near field effect of the jet

The configurations of the mixing layer without and with the jet active are presented.

Figure 12 presents the results without the cross jet. The flow first develops Kelvin Helmholtz instabilities which eventually break down and lead to a fully three dimensional turbulent flow.

Figure 13 and Figure 14 represent cuts in the symmetry plane respectively in the case without and with cross jet. In the case with the mixing jet active, the three dimensional flow occurs directly downstream of the jet. RANS computations (not presented here) were also performed. In the case without jet, the RANS simulation gives an accurate result but totally fails to predict the mixing enhancement due to the cross jet.

### 6.4. Future of LES

LES is a very efficient tool for free shear flow. This kind of flow does not depend too much on the Reynolds number and with today's computers realistic configurations can be computed. To apply the LES methodology to wall bounded flows is a different matter. For these flows, the Reynolds number effect is very strong. As seen earlier, the LES method requires to resolve the structures which contain

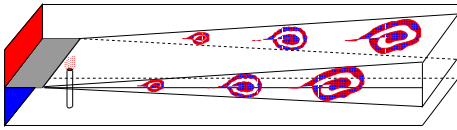


Figure 11. Schematic of the experiment

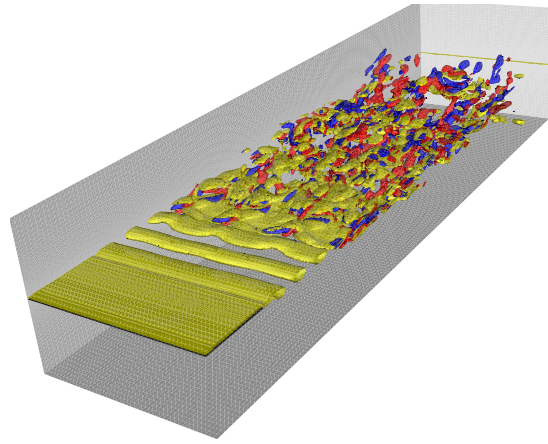


Figure 12. Subsonic/supersonic mixing layer without jet.

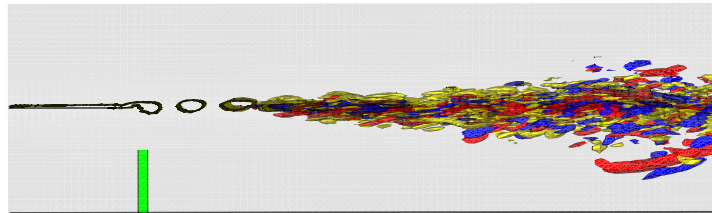


Figure 13. Subsonic/supersonic mixing layer.

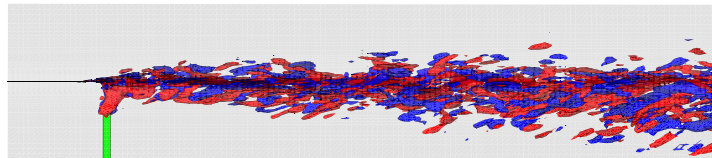


Figure 14. Subsonic/supersonic mixing layer with jet.

the energy and these structures can be very small near a wall and the computation at a realistic Reynolds number (say  $Re = 10^6$ ) is a formidable task. For wall bounded flows, the difficulties to be encountered can be listed

- very fine mesh needed to resolve the scales containing the energy in the wall region (fine mesh required in both spanwise and normal to the wall direction, the real killer is the spanwise refinement!);
- implicit time integration required due to the very fine mesh and fast and efficient implicit solvers (e.g. multigrids);

- modification of the subgrid model to account for the low Reynolds region in the vicinity of the wall.

For wall bounded flows, two directions seem to emerge:

- use of wall function to model the near wall region;
- hybrid RANS/LES method such the “Detached Eddy Simulation” (DES) proposed by Spalart *et al.* (1997).

The last method seems more promising towards a “general” turbulence model. Such a model should be able to automatically detect the region where all the scales can be modeled (RANS approach) and the region where the energy containing eddies must be resolved (LES). There is work in progress and some results can be expected soon.

## 7. MESH GENERATION

In order to use a CFD code in an industrial setting, the point is not to simply have access to a CFD code, but to master all the necessary paraphernalia around it. Obviously, as a starting point, one needs efficient solvers with respect to the available computing resources. Besides, one needs a discretized geometry to work with: CAD/CAM tools constitute the basis of all geometrical shape design. Once the desired shape has been modelled, it is fairly easy to discretize it into a surface mesh. One of the great challenges of CFD is to build a volume mesh from the surface mesh, which meets the requirements of a Navier-Stokes computation. Whereas the generation of volume meshes for inviscid Euler calculations can be fairly automated, the construction of Navier-Stokes grids still requires a great deal of human input and insight. In particular, a lot of care must be taken to cluster mesh points close to the wall in order to capture the features of the boundary layer.

Mesh generation methods have evolved in time along with the wish to compute more and more complex flows and geometries.

Early meshes were built using cartesian methods with quadrangles on the boundaries and hexahedral bricks in the volume. Each vertex is completely defined by an array of indices. This type of regular mesh is referred to as “structured” (see Figure 15). Node neighbors are implicitly defined by the  $(i, j, k)$  index set.

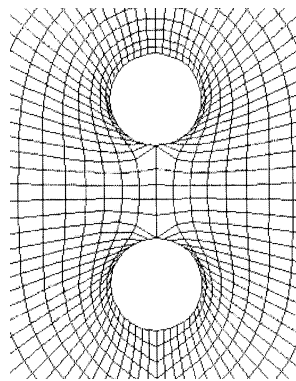


Figure 15. Typical structured mesh.

The limitation of such meshes appeared quickly with the increasing geometrical complexity of the models to be computed. Is it possible to accommodate large local concavities or convexities with regular, non skewed elements? How to handle cuspidal points? A solution might be to use “multi-block” meshes. As before with structured meshes, the same generation method is used, but the space is decomposed into as many blocks as there are geometrical difficulties. The simulation code must take care of the additional task of making the connections between blocks. One can easily imagine that this technique can turn out quite heavy to operate.

Another much more promising way towards complex geometries is to rely on so-called “unstructured” meshes. Wall surfaces are described using triangles and volume elements which build upon these faces are tetrahedra and sometimes prisms. Neighbor connections are no longer implicit; they must be described through a connectivity array.

Early unstructured meshes (Figure 16) were very poor and numerical codes had to be pretty robust

to be able to handle them! Generation techniques gradually improved and smoothness increased dramatically, thus enabling to solve any geometrical problem.

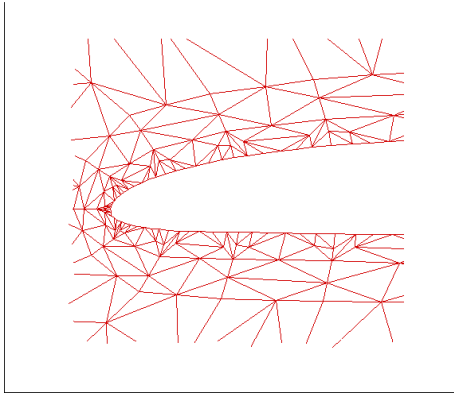


Figure 16. Falcon 50 mesh.

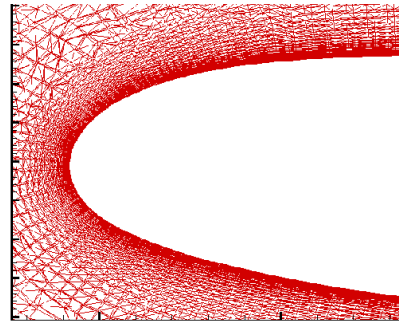


Figure 17. F7X mesh.

Several unstructured mesh generation techniques coexist. They all rely on a similar workflow:

- (i) define the boundaries of the computational domain;
- (ii) specify a cell size and generate nodes;
- (iii) connect the nodes;
- (iv) (eventually) optimize the geometry of the elements (smoothness and aspect ratio);
- (v) (eventually) optimize the connectivity (node neighbors).

In fluid mechanics and especially when a detailed representation of the wall boundary-layer is searched, the frontal mesh generation method reveals the most appropriate. The space is filled up one layer at a time starting from the discretization of the wall surface. This technique generates its own free-stream boundaries and enables a fine control of the mesh size close to the wall. Nodes are located in a way suitable for the calculation of the near-wall velocity profiles. Such a mesh is presented in Figure 17. It must be contrasted with the mesh of Figure 16 whose sole quality in its time was to connect the nodes together and to be computable.

Progress has still to be made towards a greater automation of the mesh generation algorithms described above. This automation might see computation overcome experimentation with substantial cost reductions, and will in any case allow the simulation of even more complex phenomena for which for instance the model can vary in time: as the geometry evolve in time, wall and volume meshes will have to deform, adapt, and eventually rebuild themselves. Figure 18 shows an example of an adapted mesh where different geometrical scales are present: the model is about 12 cm long and the nose radius does not exceed 1 mm. Mesh clustering near the wall is required to capture the features of the boundary layer; adaptive remeshing was able to enrich the mesh in the shock regions (detached bow shock and shock induced by the separation at the compression corner) and to capture the slip line where both shocks interact.

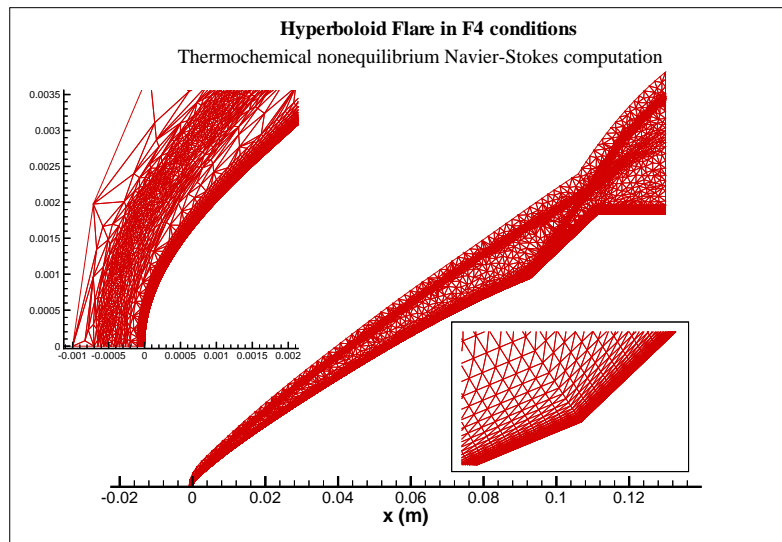


Figure 18. Hyperboloid Flare: mesh.

## 8. VALIDATION

Validation is a key ingredient to building confidence in order to be able to apply codes to new configurations.

We initiated the development of our major codes in the late 80's at the time of the Hermès space plane program. A major research and development project was launched then in Europe which led to unprecedented advances in numerical analysis, Computational Fluid Mechanics, flow thermophysics...

Several Workshops (Dervieux *et al.*, 1989; Dervieux *et al.*, 1986; INRIA and GAMNI-SMAI, 1990; INRIA and GAMNI-SMAI, 1991) were organized to bring together people from the experimental world and numerical analysts. They designed challenging test cases with CFD code validation in mind: the geometries were simple enough to be computed on the machines available then; the experiments were set up with detailed instrumentation (pressure, friction, and heat flux measurements); a great care was given to clean boundary conditions: a case specified as a 2-D case tried to avoid as much as possible side effects; a difficulty scale enabled a systematic check of every element of a CFD code: 2-D vs. 3-D, inviscid vs. viscous, perfect gas vs. equilibrium and nonequilibrium thermochemical effects, catalytic vs. perfectly non-catalytic surface conditions, laminar, transitional and turbulent flow, with or without radiative effects... Such a careful validation was a premiere and the only way to face the extrapolation from ground testing to flight with enough confidence. Ground testing facilities made also considerable progress at that time, in particular in the field of high enthalpy flows.

A large validation effort in the European aeronautical industry started in the nineties with European Commission funding. We can mention a few European projects among others: EUROVAL, ETMA, ECARP, AVTAC, EUROPIV, LESFOIL, FLOMANIA... The reader is referred to Vos *et al.* (2003) for a more detailed description of major European Navier-Stokes solvers and their validation.

## 9. CODE INTERFACE

We feel that in an industrial setting, the user should ideally interact with the software through an interface which is specialized to the application. He does not need a fancy Graphical User Interface or GUI with a million options to choose from. For an aeronautical application, one should have to specify a Mach number and an altitude and press compute. It should be as easy for the user to run a basic test case with a few hundred mesh points on a PC as a complete aircraft configuration with engines and nacelles with possibly tens of million nodes on a massively parallel computer. The system should be able to take care of standard boundary conditions and algorithmic parameters in a transparent way for the user. In our experience, an industrial user should not have to bother beyond step numbers and CFL numbers. Moreover the codes should be scriptable in order to be easily integrated into design loops (optimization or multidisciplinary applications) or simply to perform parametric studies (parameter sensitivity, polar curve calculations over a range of angles of attack...).

## 10. MILITARY APPLICATIONS

### 10.1. Inlet design

When the Rafale inlet was designed in the late 70's, advanced CFD was still in its infancy. Designing such an inlet with no inside device nor moving part for supersonic flight was a challenge at the time. Extensive wind tunnel testing was conducted to study the intake placement. Many different configurations were tested: side mounting as in the Mirage series, low configuration, and intermediate semi-low configurations which was eventually adopted (see Figure 19).

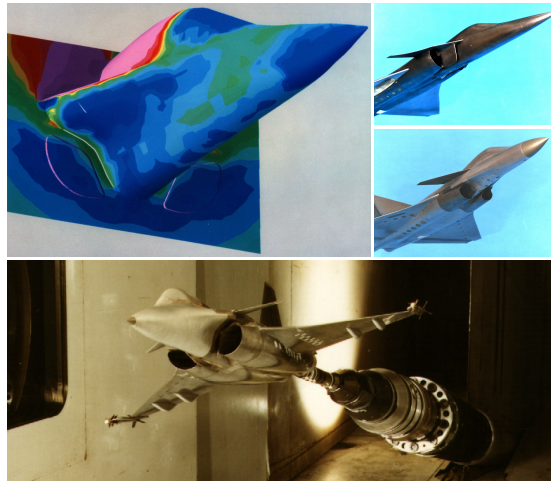


Figure 19. Inlet design.

An early optimisation loop based on a supersonic potential flow code was used to optimize the shape of the forebody. Euler calculations were then performed to check the quality of the flow at the entry plane of the inlet. Recent work has shown that modern optimum design tool such as the one described in section 14 can a posteriori validate this design. CFD was also used to check the implantation of new equipment such as antennas (see section 16.3).

In any case, inlet design will remain a challenge for the engineer. New concepts with highly curved ducts may see the limit of traditional turbulence models (see section 5) and require advanced models such as DES or LES (see section 6).

### 10.2. Store release

Modern military aircraft carry a high number of various stores at various locations. Flexible operational requirements (large range of Mach number, altitude and angles of attacks) are also demanded. These elements all lead to a need for a large number of complex store integration studies. A design strategy that combines wind tunnel tests, CFD computations and flight test must be defined. Large scale wind tunnel tests are performed with complex devices that allow an independent positioning and measurement of aerodynamic coefficients for the aircraft and the store (see Figure 20). Both flight tests and wind tunnel tests are quite costly which justifies significant computational efforts.

Several levels of numerical simulation can be considered. Configurations with many stores and

transonic Mach number flows are examples of situations where Euler computations can be required. Store integration studies require the capability to change easily the location of the store, to predict the impact of the store on the aerodynamic coefficients and the efficiency of the control surfaces of the plane. This application of CFD illustrates the need to develop complex and flexible simulation tools which include various modules that are used sequentially: mesh generation, mesh deformation, and mesh partitioning tools, flight mechanics modules (aircraft and missile) and various CFD solvers (Alleau *et al.*, 1996). At Dassault, the CFD code usually selected for these simulation is the Euler code Eugenie described in section 3. The numerical formulation relies on either a Finite volume Galerkin approach with Osher's Riemann solver and a 2nd order extension (Dervieux *et al.*, 1993) or a modified Lax Wendroff scheme. Explicit or preconditionned implicit solvers can be used.

The mesh generation strategy implemented at Dassault proceeds with the following steps: a mesh is created for the aircraft, meshes are created for each store, for a given store configuration (or when a store moves along its trajectory) a hole is created in the aircraft mesh, the store with its mesh is inserted and the meshes are connected leading to a single unstructured mesh. This approach leads to a good quality mesh close to the store and requires very low CPU resources for mesh evolution when the store moves. This technique is illustrated in Figure 22.

Store trajectory prediction is illustrated by the study of a cruise missile under a Rafale on Figure 23, and a cruise missile under a Mirage 2000 on Figure 24.



Figure 20. Store release testing at S1 Modane.

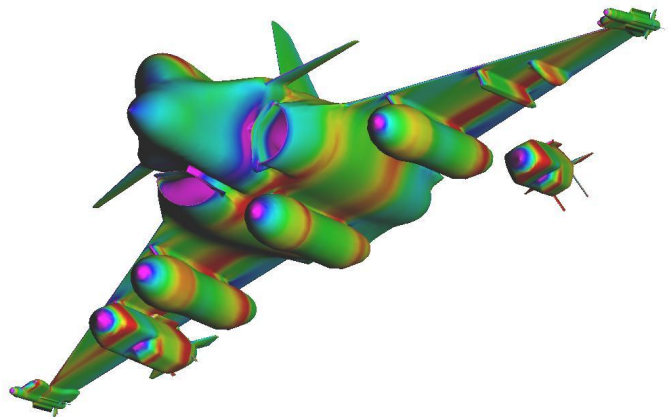


Figure 21. Euler computation of store release.

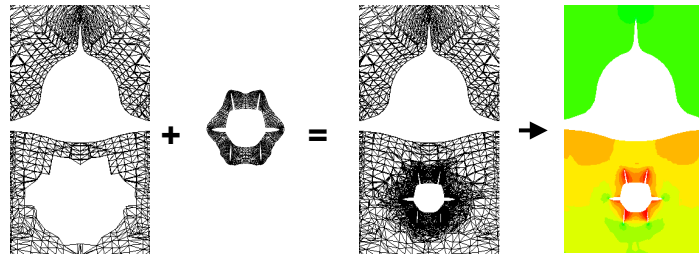


Figure 22. Mesh insertion for store release.

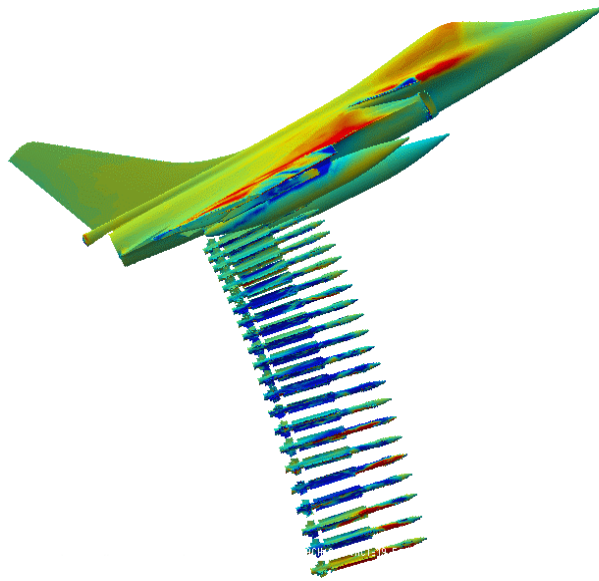


Figure 23. Rafale.

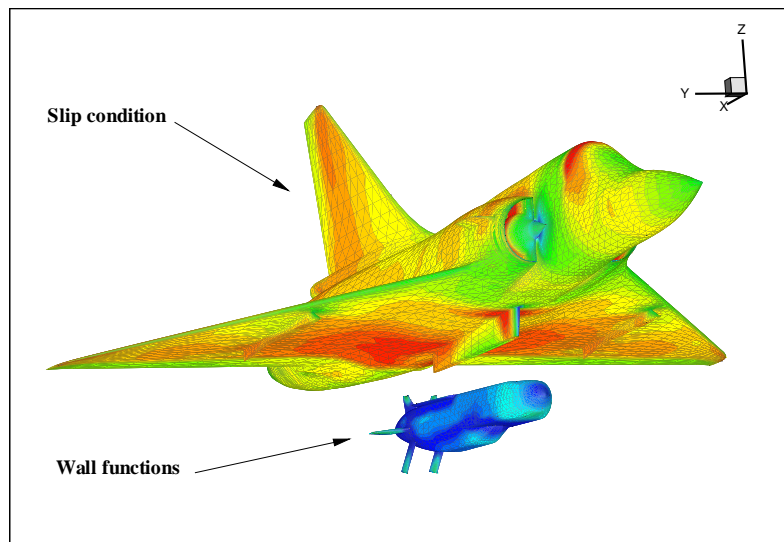


Figure 24. Mirage 2000.

### 10.3. High angles of attack and vortical flow

The flow over a delta wing at high angle of attack is characterized by a complex vortex structure and possible vortex breakdown. Accurate prediction of wing lift requires a good prediction of these vortices since the high velocity associated with the leeward vortices is associated with low pressure, while vortex breakdown will lead to a loss of lift. Figure 25 presents the vortex structure over a military wing at Mach 0.2 and an angle of attack of 25 degrees. A blunt generic forebody is included to avoid possibly unsteady cone vortices associated to a typical forebody. Slats are deflected at different angles. Three vortices are identified: one originating from the wing fuselage junction and two from each of the two slats. Computations have been performed with a two layer  $k-\varepsilon$  model and with an Explicit Algebraic Reynolds Stress model, the latter model yields improved results.

New generation stealth aircraft are characterized by shapes that combine flat surfaces and sharp angles. Complex vortical flow structures are generated even for low angles of attack. This is illustrated on Figure 26 where the flow structure over a recent UCAV (Unmanned Combat Air Vehicle) is presented. The onset and amplitude of the vortices must be computed accurately because they have an impact both on the control of the aircraft and on the fatigue life of its structure.

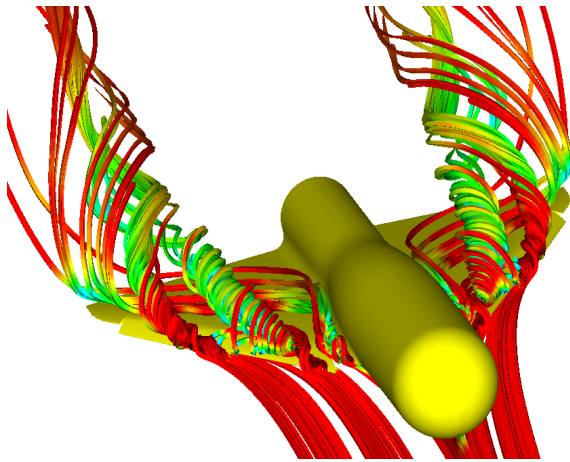


Figure 25. Mirage 2000 delta wing with generic fuselage.

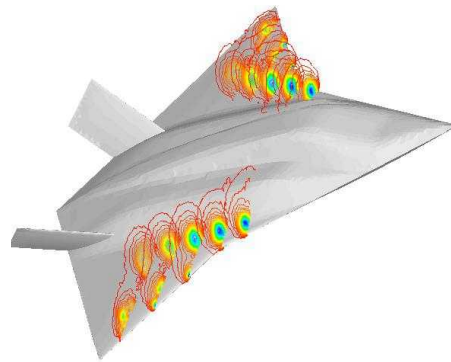


Figure 26. UCAV at high angle of attack.

## 11. CIVIL APPLICATIONS

### 11.1. Falcon 7X, PSP's, and ETW

The performance specifications for the new Falcon 7X business jet (high cruising speed, extended range, high climb rate, and short runway access) have guided the design of its aerodynamic architecture. Its new wing features include an increased leading-edge sweep angle, a high aspect ratio, and thin airfoil sections leading to an uncommon flexible structure. The complex phenomena involved implied a new approach to aerodynamic design. Intensive use of the most advanced modelization tools was made during the design process, including 3-D Navier-Stokes simulations as well as the most modern wind tunnel testing techniques and measurement tools, such as the European Transonic Windtunnel (ETW) and Pressure Sensitive Paint (PSP).

*11.1.1. Numerical modeling* The combination of detailed flow physics modeling and parallel supercomputing have revolutionized aerodynamic design. The Falcon 7X wing has been designed using an iterative process which makes intensive use of automated optimization software and numerical simulation. Both tools can generate tens of different wing shapes at lower cost. The shapes are analyzed computationally to yield the best compromise between cruise drag and usable lift range.

The best shapes are then tested in wind tunnels to validate the results. Problems observed during testing are corrected by reiterating the process. By combining the most advanced theoretical analysis with an immediate comparison of the latest experimental results, engineers can reduce the total number of development tests required prior to describing the final shape of the airplane.

*11.1.2. The ETW cryogenic wind tunnel* The ETW wind tunnel is located near Köln, Germany. A modern testing facility funded and managed by France, Germany, the UK, and the Netherlands, the tunnel was initially designed for Airbus commercial aircraft programs. ETW went into service in 1993. It is a world-class wind tunnel which can simulate on reduced scale models the real flight conditions of an airplane cruising at high altitude, reproducing the actual Mach and Reynolds numbers. Traditional wind tunnels cannot reach the highest values of Reynolds numbers seen by full-scale airplanes in flight. Consequently engineers must correct the wind-tunnel global figures, sometimes using empirical transposition rules.

Models in ETW are not placed in room-temperature air flow as in a conventional installation. Very low-temperature (down to 110 K) pure nitrogen is piped in at pressures of up to 4.5 bars. Under the combined effect of high pressure and low temperature, exact flight conditions are recreated on a given model scale. This requires electrical power of 55 MW. In addition, the liquid nitrogen mass flow rate used to keep temperatures at 110 K can reach 150 kg/s (this represents 20 semi-trailers per hour!).

Dassault Aviation used ETW for the Falcon 7X program. The wind tunnel is especially well suited to validate new wing shapes and to shed light on local phenomena, such as buffeting and aeroelastic deformation. Progress in numerical modeling and experimental techniques make for a perfect symbiosis: ETW tests validate the design choices made for the Falcon 7X wing and, in minute detail, the actual precision of the calculation results. Without the cryogenic wind tunnel, there would be no way to gauge the trustworthiness or operating limits of numerical models.

*11.1.3. Results* The ETW results obtained in early 2002 confirmed the relevance of our new approach. The experimental/calculation comparison is very good and validates our use of numerical models (see Figure 27). Information about performance under actual flight conditions improved the

procedures and transposition rules for all the traditional wind tunnels used in the full development of the Falcon 7X. We were able to compare the performances of a complete model of the aircraft in its current design to those of the Falcon 900EX in the ONERA S2 Modane wind tunnel. For example, at a cruise Mach number of 0.85, the Falcon 7X has the same lift limit as the F900EX at Mach 0.80 and shows a potential gain in lift to drag ratio of 15%.

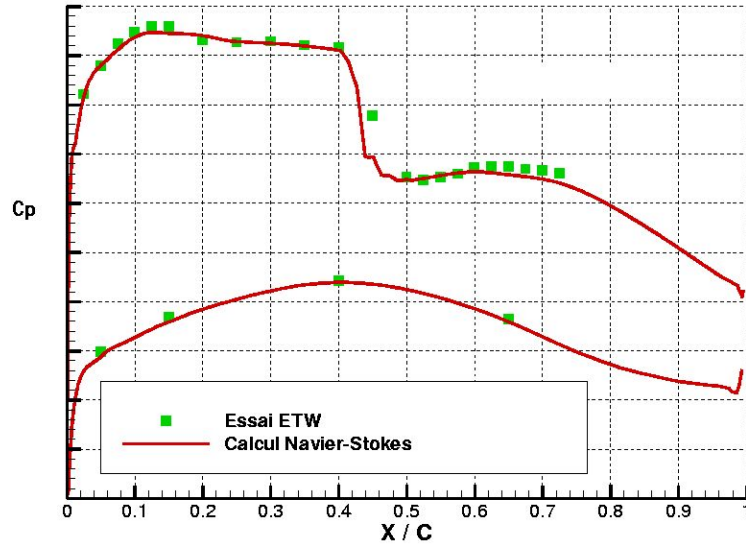


Figure 27. Comparison between Navier-Stokes calculation and ETW.

*11.1.4. Pressure sensitive paints* Figure 28 illustrates the progress achieved in both numerical simulations and experimental measurement techniques. Pressure values used to be available only at discrete locations on the wind tunnel model through intricate devices drilled in the model. Pressure Sensitive Paint (PSP) techniques developed at ONERA yield surface pressure maps comparable to those obtained with standard CFD post-processing packages. PSP's are less intrusive and more reliable (pressure taps can get clogged, and connection with the data acquisition system can be damaged). Moreover, they provide a more detailed piece of information. Unsteady extension is even under development.

Figure 28 presents the experimental result on the right, and two Navier-Stokes computations. The numerical result on the left does not take into account the deformation of the model in the wind tunnel; the calculation presented in the middle does: it matches the experiment more closely.

Figure 29 shows pressure coefficients on a complete F7X configuration with engines and stabilizers. This turbulent Navier-Stokes results is to be contrasted with the historical potential flow calculation (see Figure 4) obtained twenty years ago.

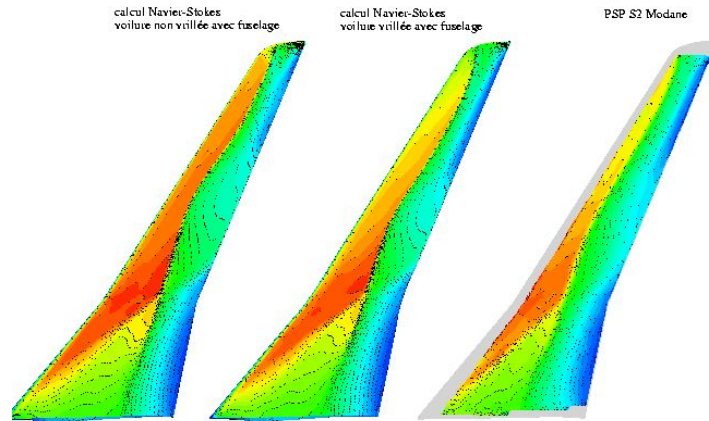


Figure 28. Comparison between Navier-Stokes calculation and PSP's.

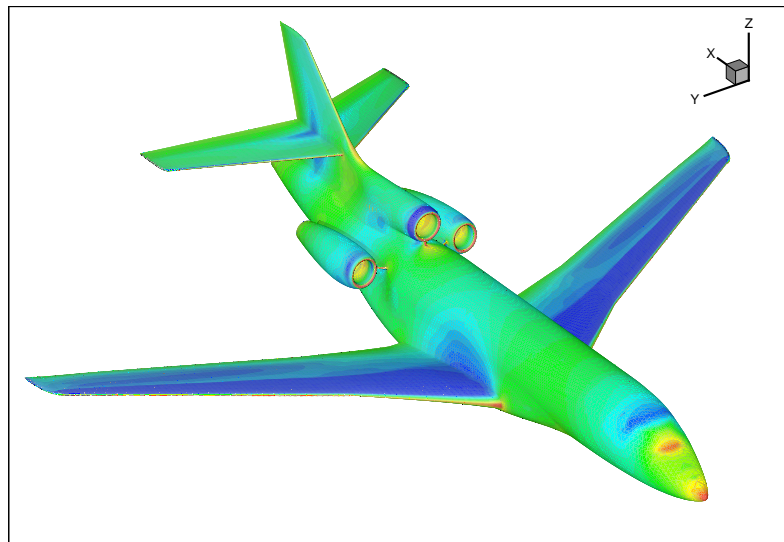


Figure 29. Falcon surface pressure.

### 11.2. Low speed, high lift and ground effect

Numerical simulations can be used to characterize the aircraft aerodynamic behavior in ground effect. Inviscid flow computations with a slip boundary condition on the ground have been shown to be sufficient to evaluate the variations of lift, pitching moment and induced drag as the airplane approaches the ground. A detailed analysis of the flowfield shows the impact of the ground on the induced downwash on the wing and on the horizontal tail surface.



Figure 30. F7X wind tunnel testing with ground effect.

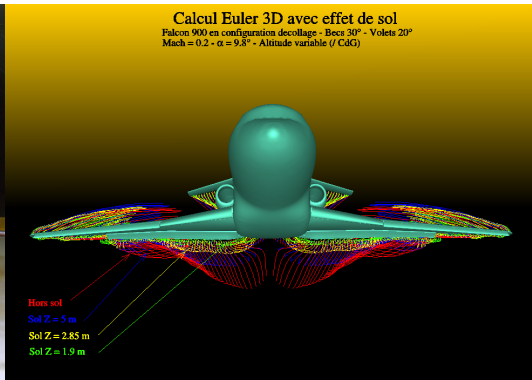


Figure 31. Euler computation of ground effect.

### 11.3. Airbrake efficiency

The combination of new developments in unstructured mesh generation and an increasing computing power have lead aerodynamicists to perform computations around complete aircraft under flight conditions different from classical cruise. One such a case is the computation of an emergency descent at high speed with extended airbrakes. The same aircraft configuration though at a lower speed can be encountered during high slope approaches to airports such as London City or Aspen, CO. The computations presented herein have been performed by solving steady RANS equations. They provide valuable information on the drag increase caused by the extension of the airbrakes. Loads on the aircraft and airbrake hinge moments can also be predicted numerically for structural design purposes. Recent developments in new numerical models such as Detached Eddy Simulation will increase the accuracy of these massively separated flow computations in the near future.

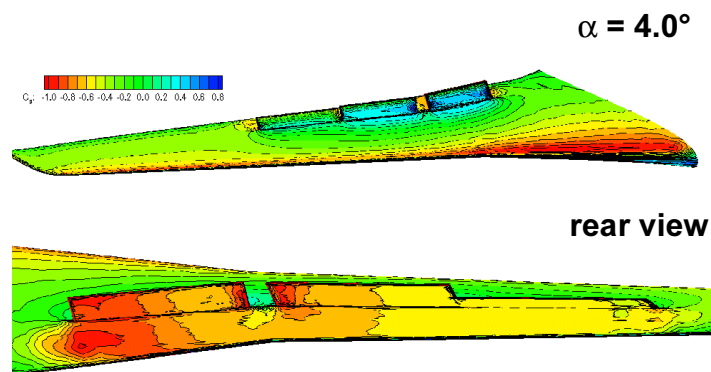


Figure 32. Airbrake efficiency.

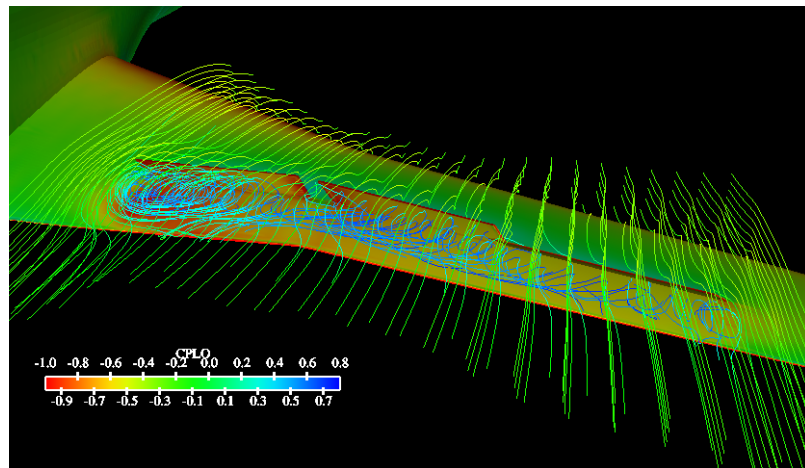


Figure 33. Airbrake efficiency.

### 11.4. Inlet design

The design of an S-duct shaped inlet is challenging. The inlet must provide a flow with the minimum of distortion in the compressor plane. The pressure loss in the inlet directly affects the thrust of the engine, and the irregularities of the flow can stall the compressor. The level and the spatial location of the pressure losses must be accurately predicted. A RANS calculation of the Falcon 50 S-duct is compared with experimental data in figure 34. The simulation uses a  $k - \varepsilon$  model and the agreement with the measurements can be improved with an anisotropic model such as the EARSM.

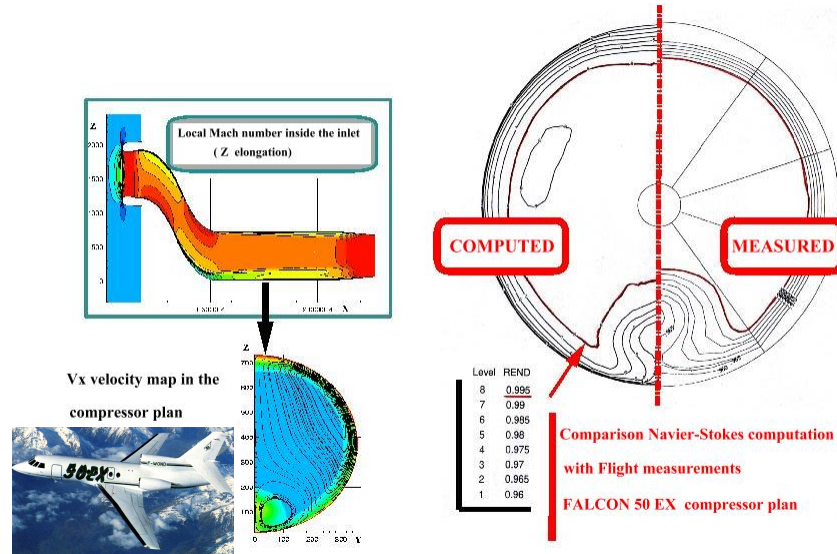


Figure 34. F50 Inlet design.

## 12. SPACE APPLICATIONS

12.1. *Hermès space shuttle and high-temperature hypersonic flows*

The first application of the NS code based on the Galerkin/least-squares approach was the aerothermal design of the Hermès space plane in the early 90's. This is illustrated by the calculation of the flow over the canopy of Hermès. It was performed at the most critical point on the reentry flight path for the windshield design: the altitude is 60 km, the Mach number is 20 and the angle of attack is 30 degrees. At this altitude the  $Re/m$  is 120,890. The equilibrium real gas hypothesis was used along with radiative boundary conditions. The mesh includes approximately one million elements. The surface mesh is presented in Figure 35. The finite element approach allows mesh refinement and a precise representation of the details of the geometry in the windshield area. Considerable mesh density is used in the direction perpendicular to the wall. Stanton number isolines are presented in Figure 36. Complex flow structure is observed. Detailed discussion of Navier-Stokes calculations related to the aerothermal design of Hermès can be found in Naïm *et al.* (1993) and Hagmeijer *et al.* (1994).

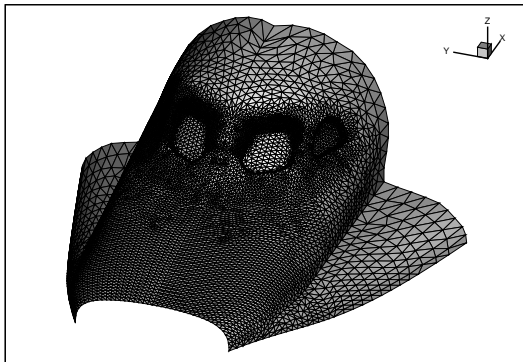


Figure 35. Hermès space shuttle: surface mesh.

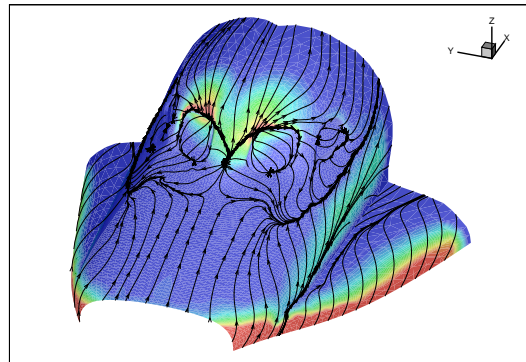


Figure 36. Hermès space shuttle: Stanton number.

### 12.2. Crew Rescue Vehicle

The second example concerns the transonic assessment of a Crew Rescue/Crew Transfer Vehicle.

Intensive parallel computing was used during the design process of the Crew Rescue/Crew Transfer Vehicle. Starting with the X-24, the final shape has been selected by NASA for its Crew Rescue Vehicle, and was at some point the basis for the European Crew Transfer Vehicle. The transonic optimization of such a spacecraft required numerous detailed computations of the complex flow between the main body and the winglets. Thanks to the NEC SX-4 installed at NLR, key ingredients to the design, such as multi-point lift-versus-drag and pitching-moment-versus-angle-of-attack curves, could be computed overnight. Eight processors were used routinely on meshes made up of about 220,000 nodes for symmetric configurations. This design project was the first project to rely on the ability to perform a complete shape computation with overnight turn over. The reader is referred to Chalot *et al.* (1997) for further details about the design of the CRV/CTV.

For the purpose of illustration, we have selected an unsymmetrical configuration past one of the many spacecraft shapes which were considered in the design iteration process: the free-stream Mach number is 0.95, the angle of attack  $20^\circ$ , and the side-slip angle  $5^\circ$ . A view of the surface mesh is presented in Figure 38. The complete three-dimensional mesh contains about 500,000 nodes.

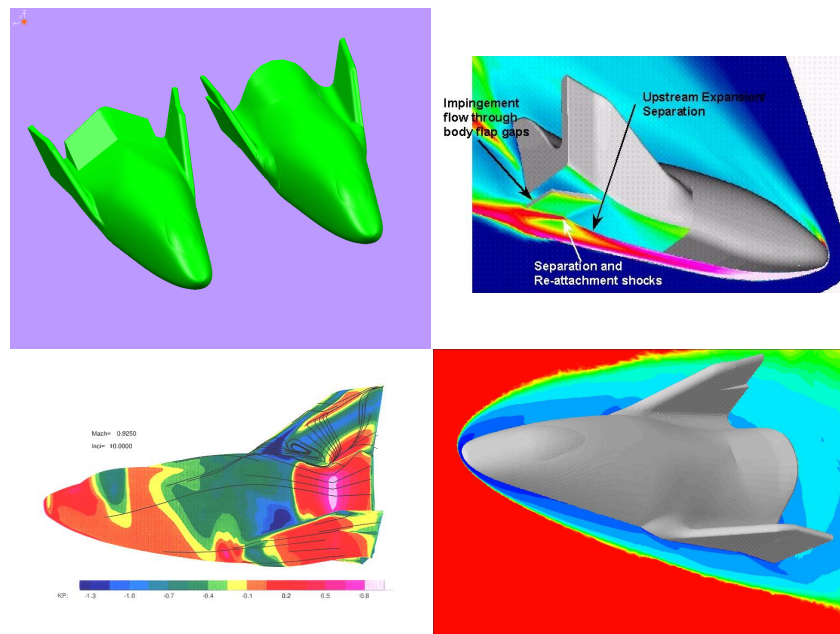


Figure 37. X-38.

Figure 39 shows the pressure-coefficient contours on the surface of the CRV/CTV; it gives an idea of the complex flow pattern which surrounds the vehicle.

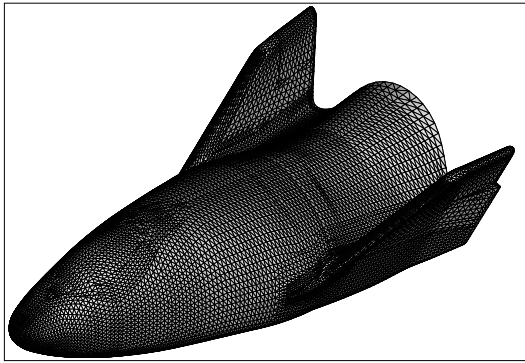


Figure 38. CRV: surface mesh.

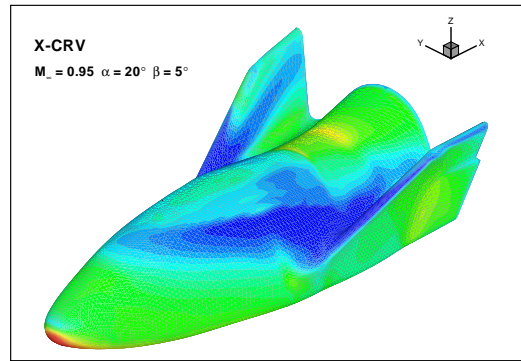


Figure 39. CRV: surface pressure.

### 13. FUNDAMENTAL STUDIES AND RESEARCH WORK

#### 13.1. Flow control

The quest for more efficient designs is a constant in the aeronautical industry. The improvement of the aerodynamic efficiency of airfoils and wings has been for a long time a preoccupation for both researchers and engineers. Flow control allows to change the flow around a given geometry without actually modifying the geometry itself. Some realisation can be listed: boundary-layer suction, vortex generators. . . Most of the past attempts were based on a trial and error approach and their results were mediocre; for instance inadequate fabrication quality impaired the efficiency of laminar design.

The better understanding of turbulence mechanisms and flow stability allowed important breakthroughs in flow control techniques: micro blowing for high angle of attack vortex flow control, boundary-layer separation control leading-edge vortex control or jet mixing enhancement.

More generally flow control benefits from the insight provided by new diagnosis tools like instantaneous flowfield measurement (PIV) or unsteady numerical simulations.

Flow control is a transverse discipline with application for both military and civil aircrafts. For a military aircrafts the aim is to improve its agility, to regularize the global aerodynamic efforts and moments or minimize its detectability. Forebody, wing leading edge, air inlet leading edge and duct, weapon bay and engine nozzle are prime candidate to accomodate control devices. For civil aircrafts the targets of flow control are less aggressive due to certification requirements. Nevertheless, flow control can lead to drag reduction, extended buffet limits or noise reduction.

#### 13.2. Forebody control at high angle of attack on a military aircraft

At high angle of attack, the fin operates in a separated flow and becomes inactive. It is thus suitable to manipulate the flow at the extreme forebody of the nose, which is naturally very unstable due to the unsymmetrical emission of alternate vortices (see Figure 40).

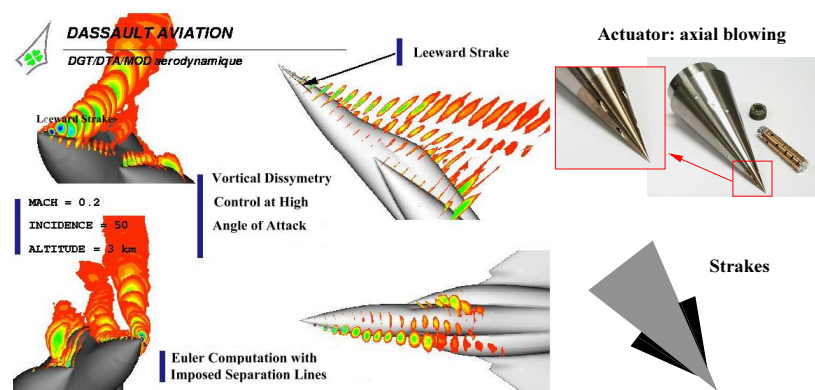


Figure 40. Forebody vortex control.

The optimization of the micro blowing devices has been conducted with experiments on generic models such as cones. Their efficiency was proven on a fighter aircraft model: the forebody yawing moment was comparable and even higher than the yawing moment produced by a 20° deflected rudder, and remained effective at angles of attack for which the rudder efficiency drops down.

Numerical simulations with the Navier-Stokes code described in section 4 have been performed for validation purpose and to analyze and understand the effect of the forward axial micro jets on the forebody vortices. The microblowing is a very efficient mean (very low injection flow rate) to symmetrize or dissymmetrize the forebody vortex shedding, and thus generates very significant lateral efforts. By an alternate left / right blowing at a given frequency, it is possible to modulate the yawing moment to a desired value.

### 13.3. Jet mixing enhancement

The objective is to find control devices to increase of the mixing rate of engine jet and thus reduce the infra-red signature and alter the noise emission. Control applied at the nozzle, either by fluidic devices like pulsed synthetic jets or by vibrating mechanical devices has been extensively studied.

A manipulation of the free shear layers a small distance downstream of the nozzle, by radial continuous and pulsed injection is considered here. Figure 41 presents a numerical comparison of the non adapted jet with and without control. It can be seen on this iso-Mach comparison that the spreading rate is significantly increased.

The leading actors are the longitudinal vortices generated by the normal interaction between the injector and the main jet, which accelerate the initial mixing between the jet and its environment. The trace of these vortices can be seen in Figures 42 and 43 which present the Mach number and the turbulent kinetic energy in a plane perpendicular to the jet.

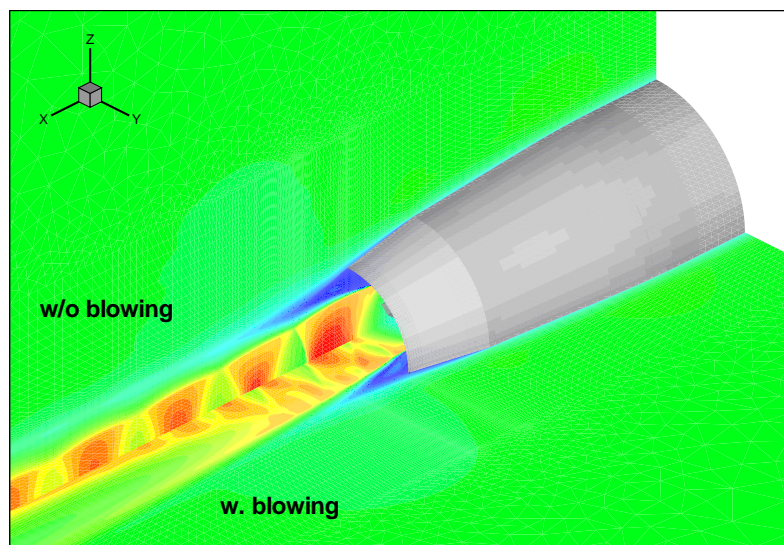


Figure 41. Jet with and without blowing.

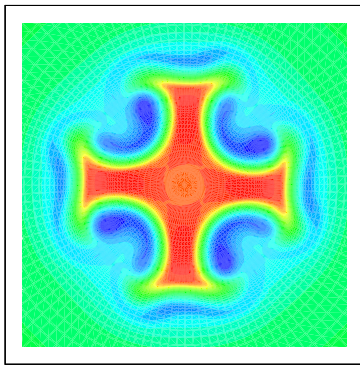


Figure 42. Mach number.

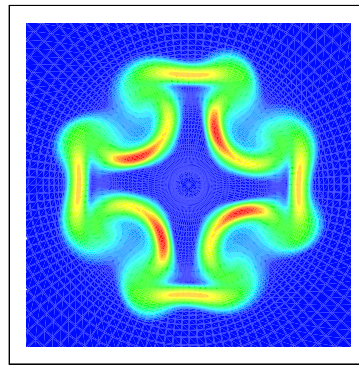


Figure 43. Turbulent kinetic energy.

## 14. SHAPE OPTIMIZATION

Automatic aerodynamic shape optimization will have a huge impact on design. It is described and illustrated in this section. Significant and continued effort (see Daumas *et al.*, 2002; Daumas *et al.*, 2002; Daumas *et al.*, 2002) has allowed a transition from a research topic to a design tool. Progressively more powerful processes are developed with more complex objectives and constraints and more accurate models: from 2-D to 3-D; from potential flow to Euler and Navier-Stokes. This already leads to better design and reduced design cycles.

In the first part, we give a description of the different modules within the considered optimization loop. The main particularity of our loop is its *CAD-based* aspect. CAD parameters are the design variables and their control is automatically driven by the optimizer.

In the second part, results of different wing optimizations on a full aircraft geometry, including wings, body and nacelle of a Dassault generic business jet (computed in the transonic domain).

### 14.1. Implementation of the overall optimization system

As shown in Figure 44, the optimization process requires the coupling of a certain number of tools. The Dassault Aviation code SOUPLE enabling these kind of computations, needs elementary modular tools like the optimizer which drives the process, the geometric modeller which allows geometric deformations, the CFD solver which provides the aerodynamic response, the cost function tool which gives the cost function evaluation and the related constraints. The modular tools can be written in any language. To link all these tools, SOUPLE is written in PERL which allows for improved modularity (see Schwartz, 1995 for more details).

### 14.2. The optimizer

The optimizer has a crucial contribution to the optimization process. Indeed, this tool will pilot the whole process by analyzing different values of the cost function and the related constraints and their sensibility with respect to the design parameters. The outputs of the optimizer are a new set of parameter values for which it is necessary to provide, on the one hand the cost function and the associated constraints and on the other hand their derivatives. In the current study, we use the optimizer developed at Dassault Aviation. This code is based on gradient evaluations which should be calculated either by finite differences or by adjoint formulation as explained later. The different available optimizers are Broydon-Fletcher-Goldfarb-Shanno (BFGS) for the unconstrained cases (Polak, 1971) and the Method of Feasible Directions for the constrained cases (Zoutendijk, 1960). The one-dimensional search is performed by either the Golden Section Method or Polynomial Extrapolation.

### 14.3. The geometric modeller

In order to obtain an efficient optimization system, a CAD-based modeller has been implemented giving access to a number of design variables for a given reference geometry. The wing is defined by a number of sub-elements defined by a set of spatial positions, tangents and curvatures. The definition of a new geometry is obtained by means of design variables defining either global wing geometric characteristics such as thickness, camber, twist, sweep etc, or local design variables.

Once the geometry is modified, a new surface mesh is generated. The latter is defined through the initial surface mesh. Indeed, we consider that the initial points are orthogonally projected on the new

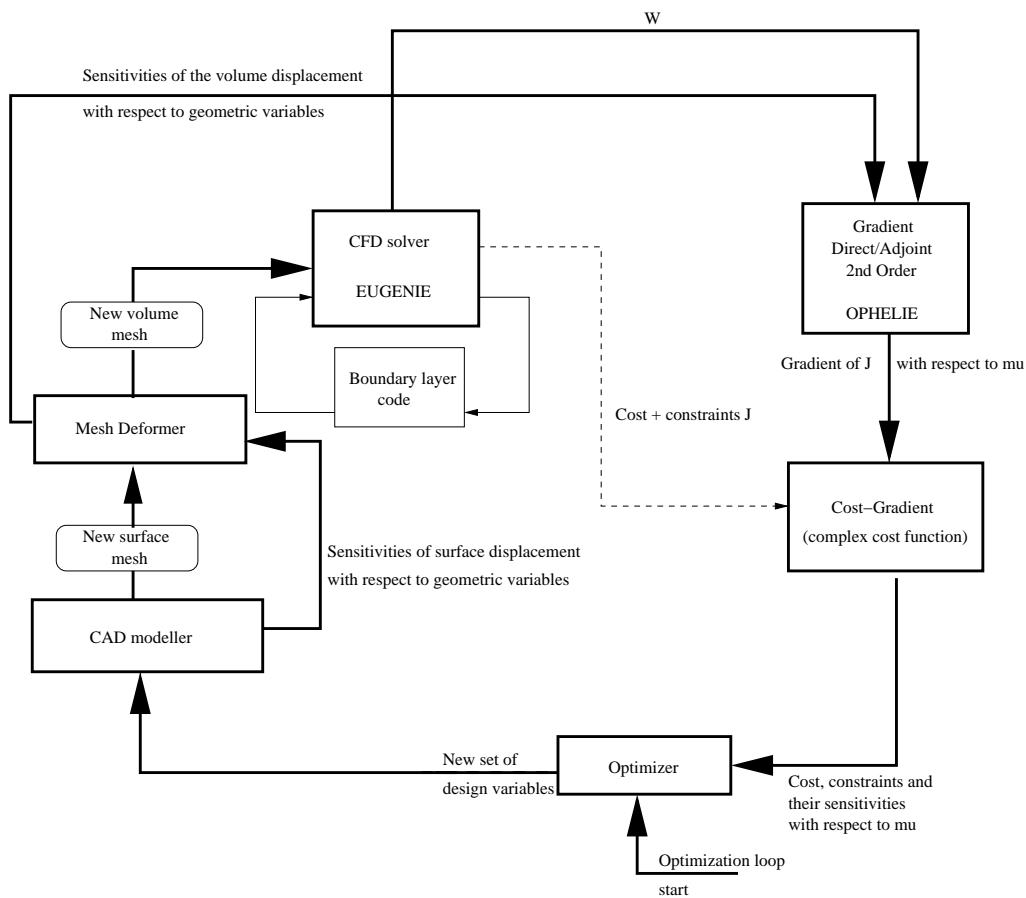


Figure 44. Overview of the Optimization process SOUPLE

surface.

The relationship between the CAD parameters and the meshes is plotted in Figures 45 and 46 where we can see how both entities behave when the twist angle for one wing section is changed. Figures 47 and 48 show a similar comparison obtained by changing the spatial positions and tangents for few CAD points from the same wing section (upper surface) while keeping the wing thickness constant. As can be seen, the modeller has moved also points from the lower surface in order to respect the constraint of thickness.

#### 14.4. The state equation

The flow solver used in the current work is the Dassault CFD solver EUGENIE based on the Euler equations (see section 3). As the main features of this code, we can list: 2-D [axisymmetric], 3-D - conservative variables - steady/unsteady (  $2^{nd}$  order temporal scheme ) - unstructured meshes mono/multi domains (complex configurations with wing, body, tail, control surfaces, nacelles, motors, air intakes, nozzles, stores...), - Finite Volumes cell vertex formulation - spatial centered schemes

*Encyclopedia of Computational Mechanics*. Edited by Erwin Stein, René de Borst and Thomas J.R. Hughes.

© 2004 John Wiley & Sons, Ltd.

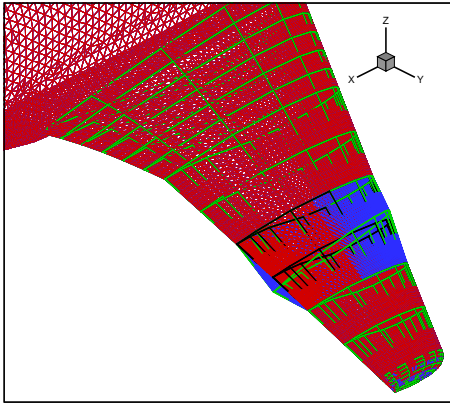


Figure 45. CAD and Meshes evolution

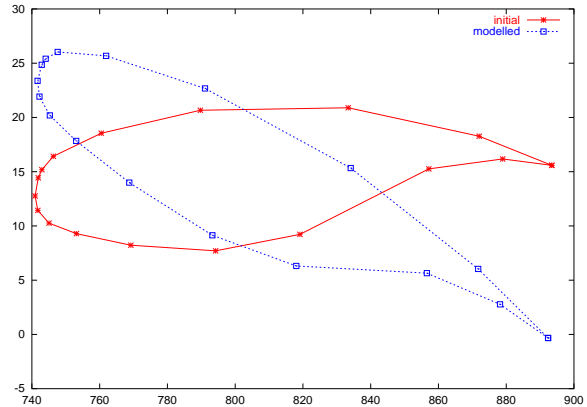


Figure 46. CAD-Profile evolution

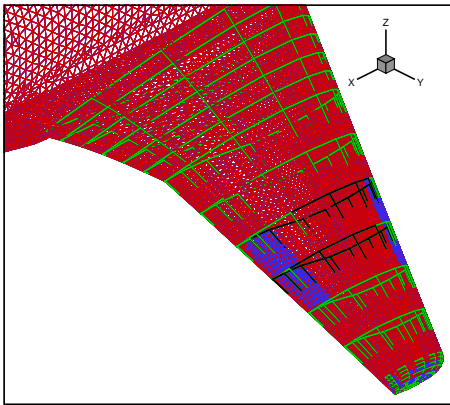


Figure 47. CAD and Meshes evolution

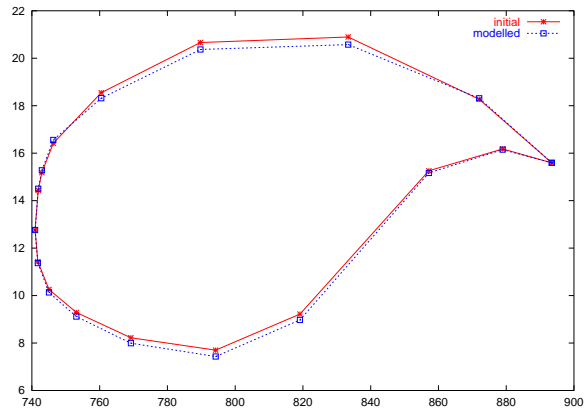


Figure 48. CAD-Profile evolution

(Lax-Wendroff,...) or upwind (Osher), large range of Mach number, perfect or real gas, chemistry - implicit strategy - dual time step - transpiration condition for moving boundaries - A.L.E, non galilean references techniques ...

In the test cases presented the Lax-Wendroff scheme was used to solve the Euler equations.

#### 14.5. The cost function and related constraints

In the current optimization process, the available cost function is based on the 6 global aerodynamic coefficients (pressure drag, lift, pitching moment...), on the spanwise lift distribution on the wing or local pressure distribution on the aircraft.

Optimization process constraints can be divided into three parts. First, there are the bounding boxes constraints concerning all optimization variables. These constraints are dealt by the optimizer. Constraints can also be imposed on particular design variables such as the thickness of the wing, or the leading edge radius. Respecting these constraints is assumed by the CAD-modeller as shown in Fig.

47 and 48. Finally, other constraints concern the different aerodynamic coefficients. These constraints can be considered either by penalization in the cost function using weight factors or by optimization subjected to non-linear equality and/or inequality constraints (even with their absolute value).

#### 14.6. The gradient evaluation

The general formulation of a shape optimization problem has been introduced by many authors: Cea (1981), Pironneau (1984), Jameson (1988), Cornuault *et al.* (1992), and Dervieux *et al.* (1994). To reduce computational costs and avoid numerical problems, analytical derivatives should be preferred to standard finite differences techniques. To make use of automatic differentiation tools, we choose an approach called discrete sensitivity analysis (Dinh *et al.*, 1996). It consists in applying the control theory to the discrete equations.

The mathematical formulation of a shape optimization problem is:

Find a shape  $\mu^* \in \mathcal{O}$  (a family of shapes) such that

- $\mu^* = \arg \min_{\mu \in \mathcal{O}} j(\mu)$  where  $j(\mu)$  denotes a cost function given by  $j(\mu) = J(\mu, \mathbf{W}(\mu))$  and  $\mathbf{W}(\mu)$  is the state-vector solution to the state equation  $\mathbf{E}(\mu, \mathbf{W}(\mu)) = 0$
- the constraints  $\mathbf{g}(\mu) = \mathbf{G}(\mu, \mathbf{W}(\mu))$  are respected, i.e. for each component of  $\mathbf{g}$ , we have  $\mathbf{g}_i(\mu) \leq 0$ .

We note  $\mathbf{f}(\mu) = \mathbf{F}(\mu, \mathbf{W}(\mu)) = (J(\mu, \mathbf{W}(\mu)), \mathbf{G}(\mu, \mathbf{W}(\mu)))$  the vectorial observation composed by the cost and constraints functions. To solve the previous problem, we have to compute the gradients of this observation with respect to the design variables  $\mu$ .

In the following equations,  $\mu$  is split into two groups of variables:  $\mathbf{l}$  is supposed to represent design variables such as the angle of attack  $\alpha$ , and  $\nu$  is supposed to represent geometric design variables which are linked to  $\mathbf{d}$  the surface displacement given by our CAD modeller, as defined in paragraph 14.3.

*14.6.1. The transpiration condition approach* In the first optimization approach developed by Dassault Aviation, body shape deformations were taken into account via an equivalent normal velocity distribution on the body, which is computed using surface normals. This hypothesis is valid for ‘small’ deformations and allows us to avoid deforming volume meshes (see Lighthill, 1958).

Considering the derivatives of  $f(\mu)$  and of the state equation, we obtain the following system of equations:

$$\left\{ \begin{array}{ll} \mathbf{E}(\mathbf{l}, \mathbf{d}(\nu), \mathbf{W}(\mu)) = \mathbf{0} & \text{(state)} \\ \frac{\partial \mathbf{E}}{\partial \mathbf{W}}(\mathbf{l}, \mathbf{d}(\nu), \mathbf{W}(\mu)) \left[ \frac{\partial \mathbf{W}}{\partial \mathbf{l}}, \frac{\partial \mathbf{W}}{\partial \nu} \right] = - \left[ \frac{\partial \mathbf{E}}{\partial \mathbf{l}}, \frac{\partial \mathbf{E}}{\partial \mathbf{d}} \frac{\partial \mathbf{d}}{\partial \nu} \right] & \text{(state derivative)} \\ f'(\mu) = \frac{\partial F}{\partial \mu}(\mu, \mathbf{W}(\mu)) & \text{(optimality)} \end{array} \right. \quad (10)$$

Using these notations, this leads to the direct formulation:

$$\left\{ \begin{array}{l} \frac{d\mathbf{F}}{d\mathbf{l}} = \frac{\partial \mathbf{F}}{\partial \mathbf{l}} + \frac{\partial \mathbf{F}}{\partial \mathbf{W}} \frac{\partial \mathbf{W}}{\partial \mathbf{l}} \\ \frac{d\mathbf{F}}{d\nu} = \frac{\partial \mathbf{F}}{\partial \mathbf{d}} \frac{\partial \mathbf{d}}{\partial \nu} + \frac{\partial \mathbf{F}}{\partial \mathbf{W}} \frac{\partial \mathbf{W}}{\partial \nu} \end{array} \right. \quad (11)$$

Introducing an adjoint state  $\Psi$ ,

$$\begin{cases} \mathbf{E}(\mathbf{l}, \mathbf{d}(\nu), \mathbf{W}(\mu)) = \mathbf{0} & \text{(state)} \\ \left[ \frac{\partial \mathbf{E}}{\partial \mathbf{W}}(\mathbf{l}, \mathbf{d}(\nu), \mathbf{W}(\mu)) \right]^T \Psi(\mu) = \left[ \frac{\partial \mathbf{F}}{\partial \mathbf{W}}(\mu, \mathbf{W}(\mu)) \right]^T & \text{(adjoint state)} \\ f'(\mu) = \frac{\partial F}{\partial \mu}(\mu, \mathbf{W}(\mu)) - \langle \Psi(\mu), \frac{\partial \mathbf{E}}{\partial \mu}(\mu, \mathbf{W}(\mu)) \rangle & \text{(optimality)} \end{cases} \quad (12)$$

Using these notations, this leads to the adjoint formulation:

$$\begin{cases} \frac{d\mathbf{F}}{d\mathbf{l}} = \frac{\partial \mathbf{F}}{\partial \mathbf{l}} - \Psi^T \frac{\partial \mathbf{E}}{\partial \mathbf{l}} \\ \frac{d\mathbf{F}}{d\nu} = \left[ \frac{\partial \mathbf{F}}{\partial \mathbf{d}} - \Psi^T \frac{\partial \mathbf{E}}{\partial \mathbf{d}} \right] \frac{\partial \mathbf{d}}{\partial \nu} \end{cases} \quad (13)$$

The introduction of the adjoint problem resulted from the application of control theory on the continuous system where the flow equations are viewed as a constraint. More details can be found in Lions (1968) and Dinh *et al.* (1996). This analysis can be directly performed on the discretised system with the help of automatic differentiation tools, such as ODYSSEE (Rostaing, Dalmas and Galligo, 1993).

In system (12), the evaluation of gradient  $f'$  is done at the cost of one extra linear equation, namely the adjoint equation for each component of  $F$ . This is the main advantage over traditional finite differences techniques where this extra cost is linear in terms of the size of  $\nu$ .

However, the complete evaluation of  $f'$  requires also the computation of  $\partial F / \partial \mathbf{W}$  and  $\partial \mathbf{E} / \partial \nu$ , which needs inputs from other tools than the CFD solver, namely the geometric modeller and the post-processing package (for example drag computations).

*14.6.2. The mesh deformation approach* In order to be not limited to ‘small’ deformations and lifting surfaces, we develop a new approach to take into account body shape deformations. Instead of the approximation made by the transpiration condition, we extend the surface displacement given by the CAD modeller to the volume mesh by a laplacian-like mesh deformation operator:

$$\mathbf{L}(\mathbf{d}(\nu), \mathbf{D}(\nu)) = \mathbf{0}$$

We solve the following problem:

$$\begin{cases} -\nabla \cdot (\kappa \nabla \mathbf{D}(\nu)) = \mathbf{0} \\ \mathbf{D}(\nu)|_{\Gamma_0} = \mathbf{d}(\nu) \\ \mathbf{D}(\nu)|_{\Gamma_\infty} = \mathbf{0} \end{cases} \quad (14)$$

where  $\Gamma_0$  is the surface,  $\Gamma_\infty$  is the infinite limit of our mesh, and  $\kappa$  is a local coefficient which is proportionnal to the volume of the tetrahedron.

Considering the derivatives of  $f(\mu)$ , of the state equation, and of the mesh deformation equation, we

obtain the following system of equations:

$$\left\{ \begin{array}{l} \mathbf{E}(\mathbf{l}, \mathbf{D}(\nu), \mathbf{W}(\mu)) = \mathbf{0} \quad (\text{state}) \\ \frac{\partial \mathbf{E}}{\partial \mathbf{W}}(\mathbf{l}, \mathbf{D}(\nu), \mathbf{W}(\mu)) \left[ \frac{\partial \mathbf{W}}{\partial \mathbf{l}}, \frac{\partial \mathbf{W}}{\partial \nu} \right] = - \left[ \frac{\partial \mathbf{E}}{\partial \mathbf{l}}, \frac{\partial \mathbf{E}}{\partial \mathbf{D}} \frac{\partial \mathbf{D}}{\partial \nu} \right] \quad (\text{state derivative}) \\ \mathbf{L}(\mathbf{d}(\nu), \mathbf{D}(\nu)) = \mathbf{0} \quad (\text{mesh deformation}) \\ \frac{\partial \mathbf{L}}{\partial \mathbf{D}}(\mathbf{d}(\nu), \mathbf{D}(\nu)) \frac{\partial \mathbf{D}}{\partial \nu} = - \frac{\partial \mathbf{L}}{\partial \mathbf{d}} \frac{\partial \mathbf{d}}{\partial \nu} \quad (\text{mesh deformation derivative}) \\ f'(\mu) = \frac{\partial F}{\partial \mu}(\mu, \mathbf{W}(\mu)) \quad (\text{optimality}) \end{array} \right. \quad (15)$$

Using these notations, this leads to the “total” direct formulation:

$$\left\{ \begin{array}{l} \frac{d\mathbf{F}}{d\mathbf{l}} = \frac{\partial \mathbf{F}}{\partial \mathbf{l}} + \frac{\partial \mathbf{F}}{\partial \mathbf{W}} \frac{\partial \mathbf{W}}{\partial \mathbf{l}} \\ \frac{d\mathbf{F}}{d\nu} = \frac{\partial \mathbf{F}}{\partial \mathbf{D}} \frac{\partial \mathbf{D}}{\partial \nu} + \frac{\partial \mathbf{F}}{\partial \mathbf{W}} \frac{\partial \mathbf{W}}{\partial \nu} \end{array} \right. \quad (16)$$

Introducing an adjoint state  $\Psi$ , we have:

$$\left\{ \begin{array}{l} \mathbf{E}(\mathbf{l}, \mathbf{D}(\nu), \mathbf{W}(\mu)) = \mathbf{0} \quad (\text{state}) \\ \left( \frac{\partial \mathbf{E}}{\partial \mathbf{W}}(\mathbf{l}, \mathbf{D}(\nu), \mathbf{W}(\mu)) \right)^{\mathbf{T}} \Psi(\mu) = \left[ \frac{\partial \mathbf{F}}{\partial \mathbf{W}}(\mu, \mathbf{W}(\mu)) \right]^{\mathbf{T}} \quad (\text{adjoint state}) \\ \mathbf{L}(\mathbf{d}(\nu), \mathbf{D}(\nu)) = \mathbf{0} \quad (\text{mesh deformation}) \\ \frac{\partial \mathbf{L}}{\partial \mathbf{D}}(\mathbf{d}(\nu), \mathbf{D}(\nu)) \frac{\partial \mathbf{D}}{\partial \nu} = - \frac{\partial \mathbf{L}}{\partial \mathbf{d}} \frac{\partial \mathbf{d}}{\partial \nu} \quad (\text{mesh deformation derivative}) \\ f'(\mu) = \frac{\partial F}{\partial \mu}(\mu, \mathbf{W}(\mu)) - \langle \Psi(\mu), \frac{\partial \mathbf{E}}{\partial \mu}(\mu, \mathbf{W}(\mu)) \rangle \quad (\text{optimality}) \end{array} \right. \quad (17)$$

Using these notations, this leads to the formulation with the direct mode for the differentiation of the mesh deformation equation and the adjoint mode for the differentiation of the state equation:

$$\left\{ \begin{array}{l} \frac{d\mathbf{F}}{d\mathbf{l}} = \frac{\partial \mathbf{F}}{\partial \mathbf{l}} - \Psi^{\mathbf{T}} \frac{\partial \mathbf{E}}{\partial \mathbf{l}} \\ \frac{d\mathbf{F}}{d\nu} = \frac{\partial \mathbf{F}}{\partial \mathbf{D}} \frac{\partial \mathbf{D}}{\partial \nu} - \Psi^{\mathbf{T}} \frac{\partial \mathbf{E}}{\partial \mathbf{D}} \frac{\partial \mathbf{D}}{\partial \nu} \end{array} \right. \quad (18)$$

Introducing adjoints for the differentiation of the state and mesh deformation equations, we have:

$$\left\{ \begin{array}{l} \mathbf{E}(\mathbf{l}, \mathbf{D}(\nu), \mathbf{W}(\mu)) = \mathbf{0} \quad (\text{state}) \\ \left[ \frac{\partial \mathbf{E}}{\partial \mathbf{W}}(\mathbf{l}, \mathbf{D}(\nu), \mathbf{W}(\mu)) \right]^{\mathbf{T}} \Psi(\mu) = \left[ \frac{\partial \mathbf{F}}{\partial \mathbf{W}}(\mu, \mathbf{W}(\mu)) \right]^{\mathbf{T}} \quad (\text{adjoint state}) \\ \mathbf{L}(\mathbf{d}(\nu), \mathbf{D}(\nu)) = \mathbf{0} \quad (\text{mesh deformation}) \\ \frac{\partial F}{\partial \mathbf{D}}(\mathbf{l}, \mathbf{D}(\nu), \mathbf{W}(\mu)) - \Psi^{\mathbf{T}} \frac{\partial \mathbf{E}}{\partial \mathbf{D}}(\mathbf{l}, \mathbf{D}(\nu), \mathbf{W}(\mu)) \\ = \Phi^{\mathbf{T}} \frac{\partial \mathbf{L}}{\partial \mathbf{D}}(\mathbf{d}(\nu), \mathbf{D}(\nu)) \quad (\text{mesh deformation adjoint}) \\ f'(\mu) = \frac{\partial F}{\partial \mathbf{l}}(\mu, \mathbf{W}(\mu)) - \langle \Psi(\mu), \frac{\partial \mathbf{E}}{\partial \mathbf{l}}(\mu, \mathbf{W}(\mu)) \rangle \\ - \langle \Phi(\nu), \frac{\partial \mathbf{L}}{\partial \mathbf{d}}(\mathbf{d}(\nu), \mathbf{D}(\nu)) \frac{\partial \mathbf{d}}{\partial \nu} \rangle \quad (\text{optimality}) \end{array} \right. \quad (19)$$

Using these notations, this leads to the “total” adjoint formulation:

$$\begin{cases} \frac{d\mathbf{F}}{d\mathbf{l}} = \frac{\partial \mathbf{F}}{\partial \mathbf{l}} - \boldsymbol{\Psi}^T \frac{\partial \mathbf{E}}{\partial \mathbf{l}} \\ \frac{d\mathbf{F}}{d\nu} = -\boldsymbol{\Phi}^T \frac{\partial \mathbf{L}}{\partial \mathbf{d}} \frac{\partial \mathbf{d}}{\partial \nu} \end{cases} \quad (20)$$

**14.6.3. Automatic differentiation** The tool used to obtain the derivatives described in the previous parts is *Odyssée*, automatic differentiation software developed by the INRIA which acts by transformation of the initial code. With a given set of input variables, and a group of programs written in Fortran 77 which evaluates a numerical function  $f$ , then *Odyssée* generates sub-programs computing its derivatives with respect to those variables. This software allows us to use direct or reverse mode of automatic differentiation.

#### 14.7. Application to a business jet

**14.7.1. Test case definition** The baseline geometry used in the optimization process is a generic Falcon Jet. An unstructured mesh made up of 255,944 tetrahedra and 45,387 vertices was generated and split in 16 domains. The flight condition considered is at a Mach number of 0.8 and an angle of attack equal to  $1.5^\circ$ , for which a relative residual of  $10^{-5}$  was reached after 10 minutes of CPU time on 16 IBM pwr3 processors resulting in a lift coefficient of 0.375. The local Mach distribution on the aircraft is shown in Fig. 49.

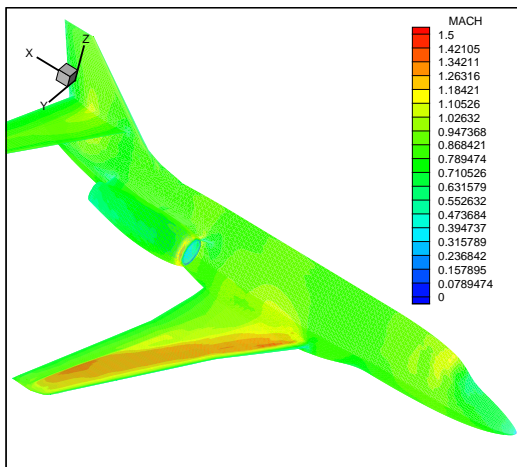


Figure 49. Mach distribution on the aircraft

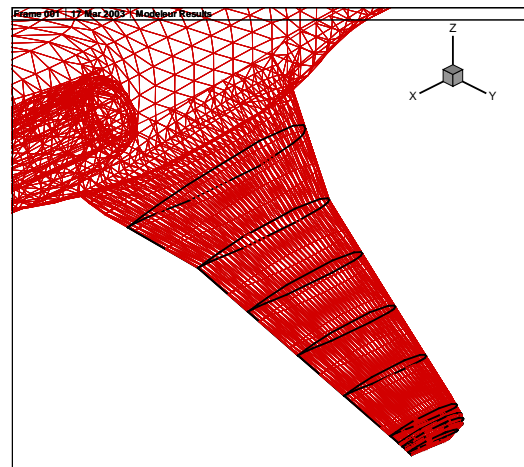


Figure 50. Location of wing sections

In the test cases which will be presented a “one shot” strategy is used i.e. each Euler computation starts from its previous solution to reach a relative residual of  $10^{-5}$  (with a maximum number of implicit strategy iterations equal to 3000).

To solve the linear systems ( $Ax = b$ ) represented in the gradients evaluation equations, we use a GMRes method with a number of Krylov of 100. We want this resolution with a relative residual of

$10^{-6}$ ; the maximum number of matrix products is 800 for each adjoint problem.

The cost function is defined to achieve a reduction of vortex drag using twist as a design parameter. Thus, a spanwise elliptical lift distribution was taken as objective defined as follows:

$$j = \frac{1}{2} \int_{y_{cut\,termin}}^{y_{max}} (cC_l - cC_l^{ell.})^2 dy \quad (21)$$

and subjected to a non linear equality constraint in order to maintain a constant lift coefficient. The relationship between this spanwise elliptical lift distribution and vortex drag is based on Prandtl theory.

The twist angle of 10 wing sections together with the angle of attack make up the set of design variables. The location of our control wing sections is shown in Fig. 50.

**14.7.2. Results** First, the evolutions of the cost function is shown in Figure 51, showing that the cost had been reduced by more than one order of magnitude.

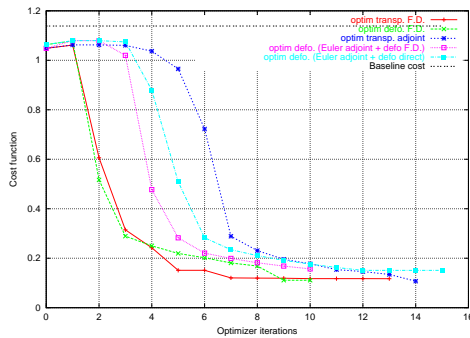


Figure 51. Cost function evolution

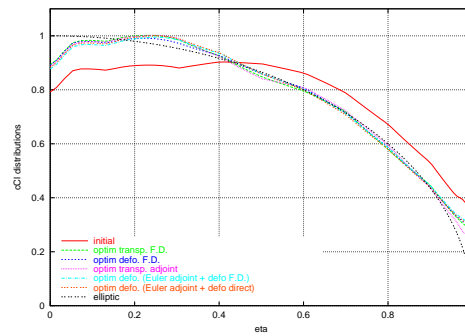


Figure 52. Lift coefficient distributions

Improvements on the cost function are illustrated by Figure 52 where the spanwise distributions of the lift coefficients are represented.

Analysis of the modified twist angle shows that when we had a sub-elliptic lift distribution, (for  $\eta \leq 0.5$ ), the optimizer led us to increase the twist angle, and conversely.

*14.7.3. Synthesis* In the following table, the results of the different optimizations which have been presented are shown in terms of gains in pressure, vortex and wave drag.

	Pressure drag (counts)	Vortex drag (counts)	Wave drag (counts)	angle of attack (deg.)	CPU cost (number of initial Euler CPU time)
Baseline configuration	328	84	30	1.50	1
Mesh deformation approach discrete Euler adjoint method F.D. deformation gradient	325	79	31	1.73	32

As can be seen in this table, significant improvement is achieved on the vortex drag with a small increase in wave drag. Indeed, we took as an objective a spanwise elliptic lift distribution which presents a local lift maximum greater than the baseline configuration. It turns out that this maximum is a first order component of the wave drag. Nevertheless, gains on vortex drag are greater than losses on wave drag.

### *Conclusion*

The optimization process has been defined and illustrated for a wing design example.

It should be emphasized that automatic optimization requires significant know-how in order to define the proper set of shape parameters, objective function (or combination of objectives), design sequences. Progressively, multidisciplinary processes are also identified and included into the optimization process.

## 15. AEROACOUSTICS

For a jet powered aircraft, the noise sources can be separated into two categories: the airframe noise generated by the high lift devices and landing gears and the power plant noise due to the turbomachines (fan, compressor, turbine) and the jet. In this section we present aeroacoustic results concerning the jet. Jet noise, which is a major contributor to the aircraft acoustic signature, has been studied for a long time. The modeling is mature, and the approach presented herein can be viewed as a “simple” post processing of a RANS calculation of the jet.

For jet noise, semi-empirical relations can be deduced from the Lighthill equation. The inputs of the acoustic semi-empirical model are obtained by a RANS calculation which gives both the mean quantities and a statistical description of the fluctuations.

The method described here was first developed for subsonic jets at ambient temperature (Bechara *et al.*, 1995) and then modified for perfectly expanded supersonic jets (Bailly, Candel and Lafon, 1996). The statistical method has two main advantages: good predictive capabilities and low computational cost; its main drawback is its narrow application field. It was worth considering its extension to more general configurations which for aircraft applications involve hot jets

The general principles of the statistical modeling of noise sources is first presented, then the extension to hot jets is detailed and finally some illustrating examples are discussed.

## 15.1. Statistical Noise Modeling

The acoustic model is derived from the density fluctuations governed by Lighthill equation (Lighthill, 1952):

$$\frac{\partial^2 \rho'}{\partial t^2} - a_o^2 \nabla^2 \rho' = \frac{\partial^2 T_{ij}}{\partial x_i \partial x_j} \quad (22)$$

The right hand side of the equations involves Lighthill tensor  $T_{ij} = \rho u_i u_j + (p - a_o^2 \rho) \delta_{ij} - \tau_{ij}$ ,  $\tau_{ij}$  represents the viscous stresses. Lighthill equation is exact but requires simplifications for a practical implementation. For a high Reynolds number flow and if the sound propagation occurs without entropy fluctuation (Bechara *et al.*, 1995), the far field solution reads

$$\rho'(\mathbf{x}, t) = \frac{x_i x_j}{4\pi a_o^4 x^3} \int_V \frac{\partial^2 T_{ij}}{\partial t^2} \left( \mathbf{y}, t - \frac{r}{a_o} \right) d\mathbf{y} \quad (23)$$

with  $r = |\mathbf{x} - \mathbf{y}|$  and  $T_{ij} \simeq \rho_o u_i u_j$ .

From the pressure autocorrelation defined by

$$R_a(\mathbf{x}, \tau) = \frac{\overline{\rho'(\mathbf{x}, t + \tau) \rho'(\mathbf{x}, t)}}{\rho_o a_o^{-3}} \quad (24)$$

the acoustic intensity can be deduced

$$I_a(\mathbf{x}) = R_a(\mathbf{x}, \tau = 0) \quad (25)$$

and also the acoustic spectral power density

$$S_a(\mathbf{x}, \omega) = \frac{1}{2\pi} \int_{-\infty}^{+\infty} R_a(\mathbf{x}, \tau) e^{i\omega\tau} d\tau \quad (26)$$

A model for  $R_a(\mathbf{x}, \tau)$  is thus needed. Assuming an isotropic turbulence convected by the mean flow (the turbulence is considered isotropic in a frame attached to the turbulent structures),  $R_a(\mathbf{x}, \tau)$  can be written as

$$R_a(\mathbf{x}, \tau) = \frac{A}{x^2} \frac{1}{C^5} \iiint_V D_{ijkl} \frac{\partial^4}{\partial t^4} R_{ijkl}(\mathbf{y}, \boldsymbol{\xi}, t - \frac{\tau}{C}) d\mathbf{y} d\boldsymbol{\xi} dt$$

where

- $D_{ijkl} = r_i r_j r_k r_l / r^4$ ;
- $A = 1/16\pi^2 \rho_o a_o^5$ ;
- $C = [(1 - M_c \cos \theta)^2 + \alpha^2 M_c^2]^{1/2}$  is the convection factor (Doppler effect).
- $R_{ijkl}$  is the correlation function in the moving frame  $R_{ijkl} = \rho^2 u'_i u'_j u''_k u''_l$

In the formulas above ' corresponds to a space-frequency localization,  $(\mathbf{y}, t)$  and '' corresponds to  $(\mathbf{y} + \boldsymbol{\xi}, t + \tau)$ . The velocity field is represented as the sum of a mean and a fluctuating component.  $\mathbf{u} = \mathbf{U} + \mathbf{u}_t$ .

The burden is now transferred on the modeling of  $R_{ijkl}$ . Following Bechara *et al.* (1995), the tensor  $R_{ijkl}$  can be written as the product of second order velocity correlations and a time correlation:  $R_{ij}(\mathbf{y}, \boldsymbol{\xi}) g(\tau)$ . The time correlation factor is chosen as  $g(\tau) = 1 / \cosh(\beta \omega_t \tau)$ .

With the hypothesis, the pressure autocorrelation tensor  $R_a(\mathbf{x}, \tau)$  becomes a function of the form  $\mathcal{F}(\mathbf{x}, \tau, \rho_o, a_o, \rho, U, M_c, u_t, L_t, \omega_t)$  and the solution of the Reynolds Averaged Navier-Stokes equations provides enough information to calculate all the quantities involved:

- The mean field (density, velocity and temperature) is directly available
- The turbulent characteristic length scale  $L_t$  and pulsation  $\omega_t$  as well as the velocity fluctuations are obtained using the turbulent kinetic energy  $k$  and its dissipation  $\varepsilon$ :  $L_t \sim k^{3/2} / \varepsilon$ ,  $\omega_t \sim \varepsilon / k$  and  $u_t \sim \sqrt{2k/3}$ ;
- only the convective Mach number  $M_c$  necessitates a specific computation that depends on the flow (simple jets (Bechara *et al.*, 1995) or coaxial jets (Héron *et al.*, 2001; Héron, Candel and Bailly, 2001)).

For this semi-empirical model, a global scaling parameter must be determined once and for all using an experimental result. The extension of the statistical model to account for entropy fluctuations is presented in the next paragraph.

### 15.2. Acoustic model for hot jets

The influence of the jet temperature on the acoustic radiation is an experimental fact (Davies, Fisher and Baratt, 1963). Models that account for the temperature fluctuations already exists; derived either from dimensional analysis (Stone, 1974) or from ad-hoc modifications of statistical models (Fortune and Gervais, 1998). The model presented here is constructed from the second term in Lighthill tensor and benefits from the theoretical work of Fisher, Lush and Harper-Bourne (1973) and Morfey (1976) on entropy fluctuations. Entropy fluctuations are deduced from temperature fluctuations (Fortune and Gervais, 1998) which are computed using a turbulent transport equation. In this model it is necessary to keep the entropy fluctuations in Lighthill tensor:

$$T_{ij} = \rho u_i u_j + (p - a_o^2 \rho) \delta_{ij}$$

Following the dimensional analysis proposed by Fisher, Lush and Harper-Bourne (1973) a model accounting for the temperature effects can be derived. For a perfect gas, a first order approximation reads:

$$\delta p = a^2 \delta \rho + (p/c_v) \zeta$$

where  $\zeta$  corresponds to local entropy fluctuations. We can then write:

$$\delta p - a_o^2 \delta \rho = \left(1 - \frac{a_o^2}{a^2}\right) \delta p + \frac{\rho a_o^2}{c_p} \zeta$$

Following Lighthill (1954), the first term can be neglected for the acoustic sources of interest

$$\delta p - a_o^2 \delta \rho = \frac{\rho a_o^2}{c_p} \zeta$$

and the far field density fluctuations become

$$\rho'(\mathbf{x}, t) = \frac{1}{4\pi a_o^4 x} \int_V \left[ \frac{x_i x_j}{x^2} \frac{\partial^2 \rho u_i u_j}{\partial t^2} + \frac{\partial^2}{\partial t^2} \left( \frac{\rho a_o^2}{c_p} \zeta \right) \right] \left( \mathbf{y}, t - \frac{r}{a_o} \right) d\mathbf{y} \quad (27)$$

The acoustic intensity can be deduced from (27). Let  $\rho_{jet}$ ,  $U_{jet}$ ,  $T_{jet}$ ,  $D_{jet}$  be the density, the velocity, the temperature and the diameter of the jet. The density, temperature and sound velocity of the ambient medium at rest are respectively  $\rho_o$ ,  $T_o$  and  $a_o$ ,

- $\partial^2/\partial t^2$  is dimensionally of the order of  $(U_{jet}/D_{jet})^2$ ;
- The integration over the source volume  $V$  is of the order of  $D^3$ ;
- The last term  $\zeta/c_p$  is of the order of  $\ln(T_{jet}/T_o)$ .

The density fluctuations are now:

$$\rho' \simeq \frac{1}{a_o^4 x^2} \left[ \frac{\rho_{jet} U_{jet}^2 D_{jet}^3}{(D_{jet}/U_{jet})^2} + \frac{\rho_{jet} a_o^2}{(D_{jet}/U_{jet})^2} \ln \left( \frac{T_{jet}}{T_o} \right) \right]$$

and the acoustic intensity  $I(\mathbf{x}) = R_a(\mathbf{x}, \tau = 0)$ :

$$I \simeq \frac{\rho_{jet}^2 D_{jet}^2}{\rho_o a_o^{-3} x^2} \left[ \left( \frac{U_{jet}}{a_o} \right)^8 + \ln \left( \frac{T_{jet}}{T_o} \right) \left( \frac{U_{jet}}{a_o} \right)^6 + \left( \ln \left( \frac{T_{jet}}{T_o} \right) \right)^2 \left( \frac{U_{jet}}{a_o} \right)^4 \right]$$

if we assume that the two sources respectively associated with velocity fluctuations and temperature fluctuations are strongly correlated.

The correlations participating to the acoustic emission can be written in a general tensor form:  $R_{ijkl}$

$$\frac{1}{\rho^2} R_{ijkl} = \overline{u'_i u'_j u''_k u''_l}$$

Introducing entropy fluctuations, this tensor reads

$$\frac{1}{\rho^2} R_{ijkl} = \overline{u'_i u'_j u''_k u''_l} + \overline{u'_i u'_j S''_T} \delta_{kl} + \overline{u''_k u''_l S'_T} \delta_{ij} + \overline{S'_T S''_T} \delta_{ij} \delta_{kl}$$

where  $S_T = (a^2/c_p)\zeta$ .

From Gibbs equation and assuming a constant evolution of pressure, temperature and entropy fluctuations are directly related.

$$S_T \approx \frac{\alpha^2}{T} T_t$$

the remaining terms are velocity and temperature correlations of the general form  $\overline{u'_{ti} T'_t}$ ,  $\overline{u'_{ti} u'_{ti} T'_t}$ ,  $\overline{T'_t T'_t}$ . All these terms are modeled using space and time correlation functions.

$$\overline{A'B'} = \overline{A'B'} f(\xi) g(\tau)$$

Since the turbulent mixing is governed by the velocity fluctuations, the correlations functions are the ones already used for the velocity.

The velocity-temperature correlations are computed using a first order closure model:

$$\overline{u_{ti} T_t} = -\kappa_t \frac{\partial T}{\partial y_i}$$

The triple correlation are modeled through a turbulent diffusivity  $\kappa_t$ . Using Reynolds average, for the temperature  $\mathcal{T} = T + T_t$  where  $T$  and  $T_t$  are respectively the mean and fluctuating temperature

$$u_{tj} T_t = u_j \mathcal{T} - u_{tj} T - U_j T_t - U_j T$$

thus:

$$\overline{u_{tj} u_{tj} T_t} = \overline{u_{tj} u_j \mathcal{T}} - \overline{u_{tj} u_{tj} T} - U_j \overline{u_{tj} T_t} - \overline{u_{tj}} U_j T$$

The last term  $\overline{u_{tj}} U_j T$  is zero. Only the first term  $\overline{u_{tj} u_j \mathcal{T}}$  requires modeling since all other terms are given by turbulent closures.

If  $Q_t = Q - \overline{Q}$  is a quantity transported in a turbulent flow  $u_t$ , using a gradient closure, the double correlation  $\overline{u_{tj} Q_t}$  reads:

$$\overline{u_{tj} Q_t} = -\beta_t \frac{\partial \overline{Q}}{\partial y_j}$$

For  $(u_j \mathcal{T})_t = u_j \mathcal{T} - \overline{u_j \mathcal{T}}$ , we have:

$$\begin{aligned} \overline{u_{tj} u_j \mathcal{T}} &= \overline{u_{tj} (u_j \mathcal{T})_t} \\ &\approx -\beta_t \frac{\partial \overline{u_j \mathcal{T}}}{\partial y_j} \end{aligned}$$

and  $\overline{u_j \mathcal{T}} = U_j T + \overline{u_{tj} T_t}$ .  $\beta_t$  is a new closure coefficient.

Assuming  $\beta_t = \kappa_t$ , we finally obtain:

$$\overline{u_{tj}^2 T_t} = -\kappa_t \left[ \frac{\partial U_j T}{\partial y_j} - \kappa_t \frac{\partial^2 T}{\partial y_j^2} \right] - \overline{u_{tj}^2 T} + \kappa_t U_j \frac{\partial T}{\partial y_j}$$

The jet is assumed to be locally a unidimensional flow. The velocity can be approximated by  $\mathbf{U} \approx U_1(y_2) \mathbf{e}_1$ , which leads to:

$$\begin{aligned} \overline{u_{t1}^2 T_t} &\approx -\kappa_t \left[ U_1 \frac{\partial T}{\partial y_1} - \kappa_t \frac{\partial^2 T}{\partial y_1^2} \right] - \overline{u_{t1}^2 T} + \kappa_t U_1 \frac{\partial T}{\partial y_1} \\ &\approx \kappa_t^2 \frac{\partial^2 T}{\partial y_1^2} - \overline{u_{t1}^2 T} \\ \overline{u_{t2}^2 T_t} = \overline{u_{t3}^2 T_t} &\approx \kappa_t^2 \frac{\partial^2 T}{\partial y_2^2} - \overline{u_{t2}^2 T} \end{aligned}$$

$\overline{T'_t T''_t}$  is the only term which can not be directly deduced from a standard  $k - \varepsilon$  RANS computation. A specific model needs to be developed. A reasonable approach consists in using a transport equation for  $\sigma = \overline{T'_t T''_t}$ . This equation reads:

$$\frac{\partial \bar{\rho} \sigma}{\partial t} + \frac{\partial}{\partial y_i} (\bar{\rho} \sigma \tilde{u}_i) = \frac{\partial}{\partial y_i} \left( \left( \frac{\mu}{\text{Pr}} + \frac{\mu_t}{\text{Pr}_t} \right) \frac{\partial \sigma}{\partial y_i} \right) + 2 \bar{\rho} \kappa_t \left( \frac{\partial \tilde{T}}{\partial y_i} \right)^2 - 2 \bar{\rho} \frac{\varepsilon}{k} \sigma$$

The practical implementation involves a three equation turbulence model: a classical  $k - \varepsilon$  model augmented with a extra equation for the temperature turbulent fluctuations which are considered a passive scalar in the turbulent flow. The post processing of such a RANS calculation provides all the necessary data for the acoustic model.

### 15.3. Numerical Examples

The first example illustrates the statistical method applied to a subsonic jet at ambient temperature. The numerical simulation of the experiment of Tanna (1977) shows the predictive capability of the acoustic model. Figure 53 presents a comparison between the measured directivity (symbols) and the computed directivity (solid line). The agreement is very good except for the small observation angle ( $\theta < 20^\circ$ ), for these angles the refraction effects in the jet are important and not considered in the model. Figure 54 compares the measured (symbols) and computed (solid line) 1/3 octave band spectra for an observation angle of  $90^\circ$ .

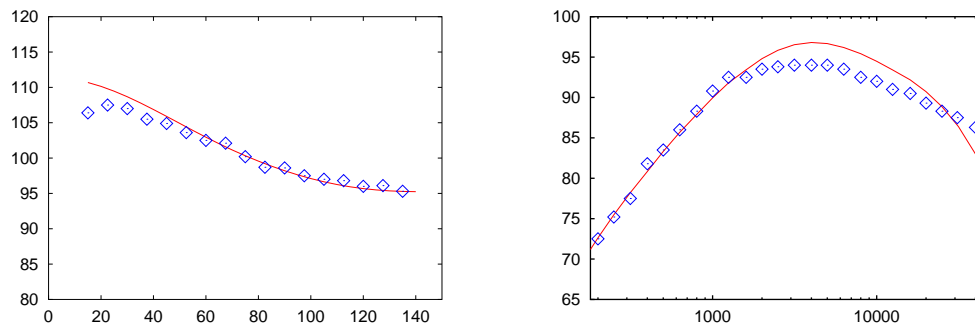


Figure 53. Subsonic cold jet: directivity in dB Figure 54. Subsonic cold jet: 1/3 octave spectrum in dB at  $90^\circ$

We now consider supersonic primary jets and attempt to simulate experiments carried out by Papamoschou and Debiasi (1999). The goal is to determine which particular secondary coaxial jets can be used to eliminate the Mach waves generated by the primary jet. The principle of this method consists in setting the secondary jet velocity at a value which brings the convection velocity of the primary jet structures to a subsonic value with respect to the sound speed in the secondary jet.

Figure 55 presents the turbulent kinetic energy for the conditions without Mach waves. Figure 56 presents the measured (symbols) and computed directivity (lines) for the cases with and without Mach waves. The good comparisons underlines the versatility of the acoustic model.

The model is finally applied to a subsonic hot jet ( $T_{jet}/T_0 = 2.3$ ) similar to the experiment from Tanna (1977). Figure 57 shows the temperature fluctuations obtained with the new turbulence model. The directivity is presented in figure 58. The green curve represents the acoustic intensity due to the

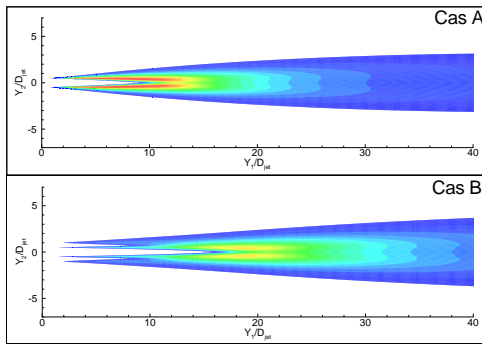


Figure 55. Turbulent kinetic energy

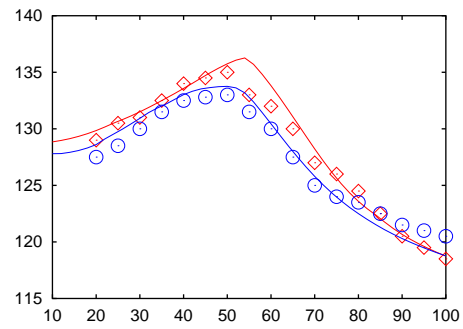


Figure 56. Coaxial Supersonic Jet: directivity in dB

velocity correlations, the cyan curve represents the acoustic intensity due to the velocity-temperature correlations and the purple curves represents the acoustic intensity due to the temperature correlations. The temperature fluctuations generate more noise than the velocity correlations! The sum of all the contributions compares well with the experimental data (symbols)

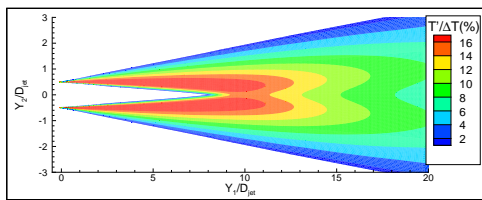


Figure 57. Temperature fluctuations

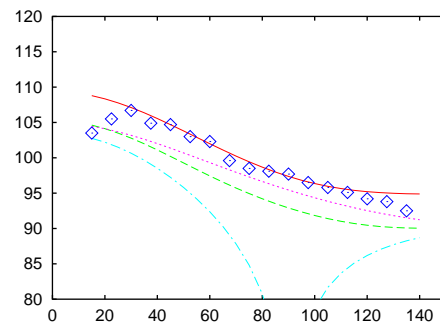


Figure 58. Subsonic hot jet: directivity in dB

## 16. MULTI-DISCIPLINARY APPLICATIONS

## 16.1. Flutter analysis

Multi physics simulation is an area of active development and fluid / structure interaction is typical example. For aircraft design, the main objective is to predict flutter. Flutter is the resonant interaction between unsteady aerodynamic loads and the elastic deformation of the aircraft structure. Flutter is a dangerous phenomena that can lead to the rapid loss of an aircraft. State of the art techniques rely on simplified linear numerical models for aerodynamics. This approach is fast and well calibrated (we emphasize the high number of configurations that must be analysed). However, when nonlinear flow behavior is present, these methods cannot be applied. Emerging techniques consider more complex flow models.

Two approaches can be considered. The first one relies on the coupling of non-linear unsteady CFD and unsteady structural dynamics codes. Significant effort has been devoted to the development of this approach. Critical numerical ingredients have been identified, most notably the need to use efficient staggered schemes and to fulfil the geometric conservation law criteria. This is described for example in Farhat and Lesoinne (1996). This approach has been implemented and demonstrated in our computational environment SOUPLE. It was used to study the flutter limit of the wing of a military aircraft with two fuel tanks. The configuration is illustrated in Figure 59 where the deformation associated with one mode is shown. The time history of one modal displacement is plotted in Figure 60. In this case, flutter is observed.

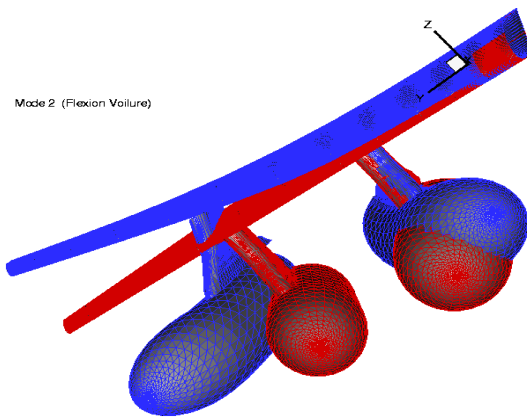


Figure 59. Fuel tank flutter.

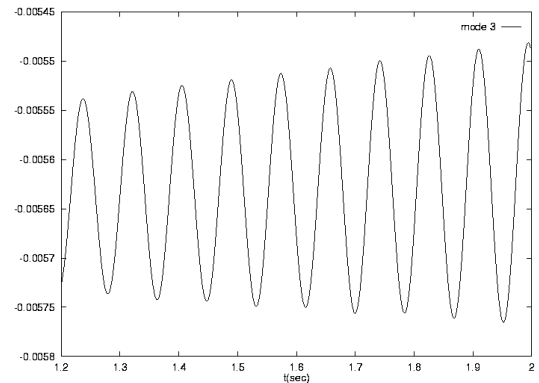


Figure 60. Divergent mode.

This approach is very general. It is however CPU intensive and this restricts its present application to validation study and to the analysis of the most critical and complex configurations.

An alternate approach is based on the solution of the linearized Euler equations in the frequency domain. The procedure includes the following steps. First a structural displacement basis is considered. For example a modal basis can be selected. The Generalized Aerodynamic Force matrix  $GAF(f)$  is computed next. For a given frequency,  $GAF(f)(i, j)$  is the aerodynamic pressure force associated to nodal displacement  $i$  when the structure oscillates along mode  $j$  at frequency  $f$ . Matrix  $GAF$  is obtained by solving the linearized Euler equations for each mode and a number of frequencies over

a selected frequency range. Typically, the number of modes considered is between 4 and 10 and the number of frequencies around 10. Between two frequencies, linear interpolation is performed. This step requires the solution of (number of modes) $\times$ (number of frequencies) complex linear systems. This is the most CPU intensive step of the procedure, however its cost is still low.

Once matrix  $GAF$  is computed, the complete dynamic behavior of the coupled system can be explored easily. The classical approach uses the ' $p-k$ ' method which is based on a loop over the velocity. Starting at zero velocity, for each velocity increment, the frequency and damping associated to each mode is computed. Flutter speed is reached as soon as negative damping is obtained.

The linearized Euler solver was developed on the basis of our industrial Euler code EUGENIE. It is an unstructured solver. A modified Lax-Wendroff numerical scheme is selected. A 1st order Steger-Warming version can also be used. Automatic differentiation was used to contribute to the generation of the code for the linearized operator. A software tool called *Odyssee* developed by INRIA was used. Significant efforts have been devoted to achieve a high level of efficiency. The GMRES linear solver was selected and incomplete LDU preconditioning is performed. Parallel implementation on distributed memory architecture has also been programmed. A detailed description can be found in Fanion (2001).

The method was validated using the well-known AGARD 445.6 wing test case. The experimental investigation was performed at NASA Langley transonic tunnel.

The wing has an aspect ratio of 4, a taper ratio of 0.6, the half-chord sweep angle is 45 degrees. The wing profile in streamwise direction is a NACA65A004. Data is available for a wide Mach number range from 0.338 to 1.141. The first four vibration modes are illustrated on Figure 61, the mesh used for the aerodynamic computations is available on Figure 62. A representative flutter diagram is presented on Figure 63. For three modes, the frequency and damping are obtained as a function of velocity. Flutter occurs when negative damping is predicted. The transonic dip phenomena is illustrated in Figure 64: the flutter speed index is plotted as a function of the Mach number. A nonlinear behavior can be observed through the transonic regime. We can verify that the linearized Euler based method can predict this phenomena correctly.

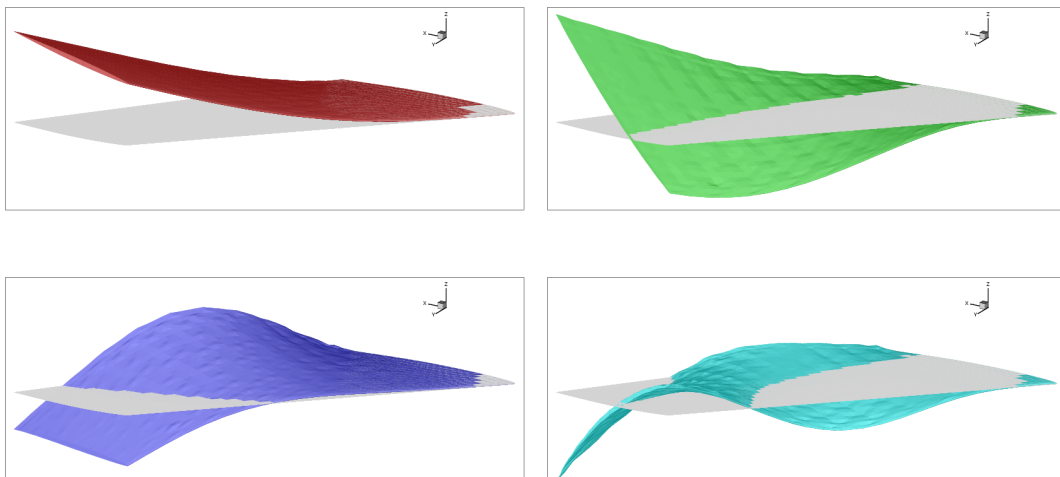


Figure 61. AGARD wing: vibration modes #1 to 4.

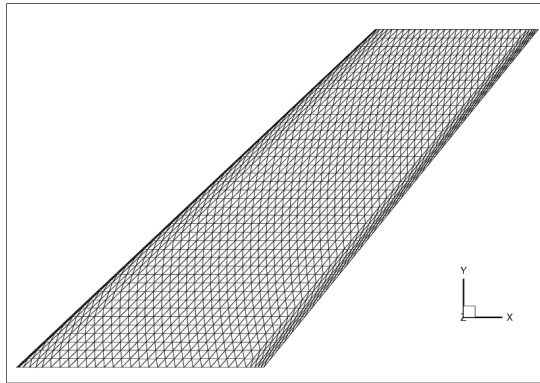


Figure 62. AGARD wing: mesh for Euler computation.

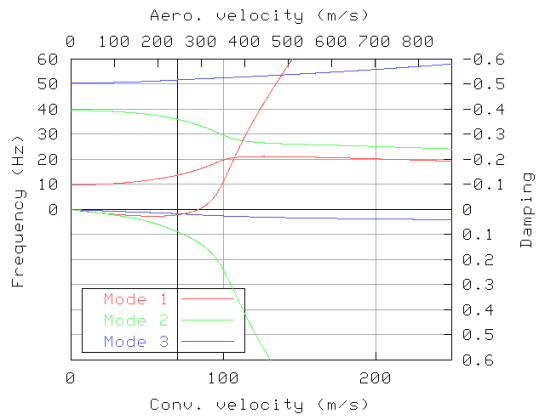


Figure 63. AGARD wing: flutter diagram (frequency and damping vs velocity for three modes).

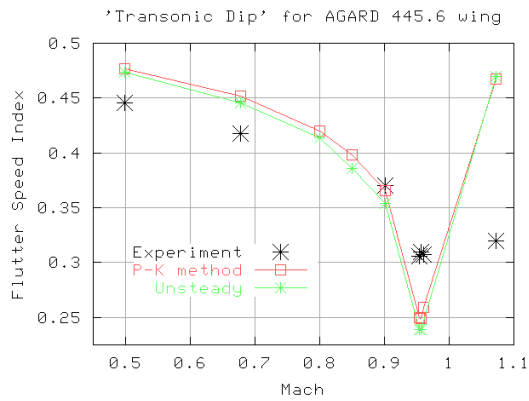


Figure 64. AGARD wing: transonic dip (flutter speed vs Mach number).

### 16.2. Parafoil

The capability of gliding parachutes to have a lift of drag ratio enough to reduce the size of the landing site is quite of interest to minimize the recovery cost of spacecraft like classical or advanced capsules. Studies, sponsored by ESA/CNES, around a half-scale demonstrator were performed in order to assess the aerodynamic characteristics and to determine the behavior of such a kind of complex configuration.

Wind tunnel experiments were performed at the ONERA S1 Modane facility (Figure 65) in order to measure the aerodynamic coefficients and the stress in the suspension lines using a specially designed balance system. This ground test of a large parafoil was a first in Europe and provided a solid validation basis for all numerical simulations.

The complete set of available theoretical tools was used to rebuild the wind tunnel test (panel method, 3-D Euler and turbulent Navier-Stokes). The non-rigid behavior of the wing was also considered with the computation of the flexible structure with a shell model and of the aerodynamic coupling which drives the equilibrium state in the wind tunnel. Figure 66 presents the pressure contours on the surface of the deformed shell structure. Good agreement in pitching moment and lift over drag ratio is obtained (see Figures 67 and 68). Further detail can be found in Tribot *et al.* (1997).

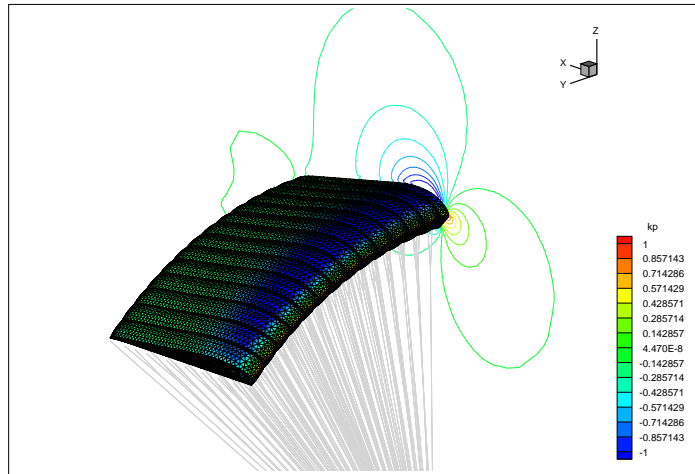


Figure 65. Parafoil model at S1 Modane.

Figure 66. Pressure contours on deformed surface.

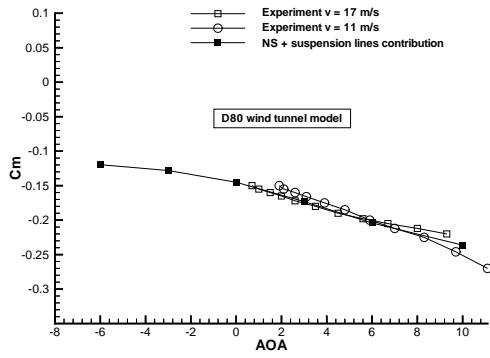


Figure 67. Pitching moment coefficient comparisons.

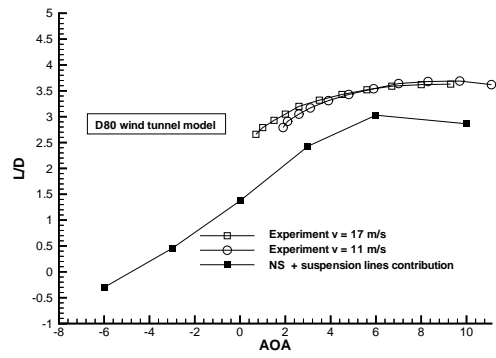


Figure 68. Lift-over-drag ratio comparisons.

### 16.3. Interaction with Electromagnetism

Conflicting disciplines make the optimization of an aircraft a challenging task. For instance, shapes suitable for a reduced electromagnetic signature may not be compatible with the greatest aerodynamic performance. Stealthiness would fancy an aircraft with no air intake, no control surfaces, no landing-gear well doors... Conversely, electromagnetic devices such as antennas and sensors need to be optimally placed on a military aircraft making sure they do not interfere with the global aerodynamic performance. An example of such an integration is presented in Figure 69. An antenna which must be located a far ahead as possible is checked against the operating range of the air intake.

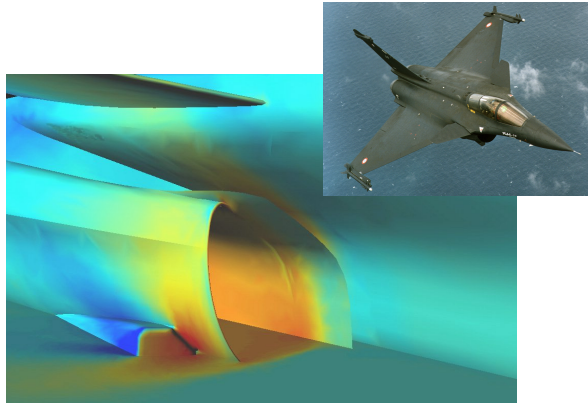


Figure 69. Antenna integration.

#### 16.4. Afterbody design and IR signature

Computation of the flow over the afterbody of a military aircraft is performed to reach two objectives: assess drag and provide data for infrared stealth prediction. Afterbody flows include many challenging features: normal shocks along the jet axis, compressible mixing layers with high density and temperature gradients, base flow and a possible shock-wave/boundary-layer interaction over the aft part of the fuselage. Turbulence models cannot account for such a range of complex flow phenomena and degraded accuracy may be expected. The thermodynamic model must account for the concentration and vibrational modes of species resulting from combustion that flow out of the nozzle. Flow control techniques are sought to enhance jet mixing and thereby reduce the signature (see section 13.3). Flow complexity is further increased when control is applied.

The geometric complexity of the afterbody of a two engine aircraft is illustrated in Figure 70. The result of a computation performed on this configuration is presented in Figure 71. CFD outputs are used as input for infrared signature computations. Thermochemical models such as those described in section 4.5 are used with a set of chemical species representative of combustion products (e.g.  $N_2$ ,  $O_2$ ,  $CO_2$ , and  $H_2O$ ); the use of a multicomponent mass-diffusion model is crucial in getting a correct description of the species mixing between the jet and the external flow. A typical Infra Red signature result is presented in Figures 72 and 73



Figure 70. Afterbody model.

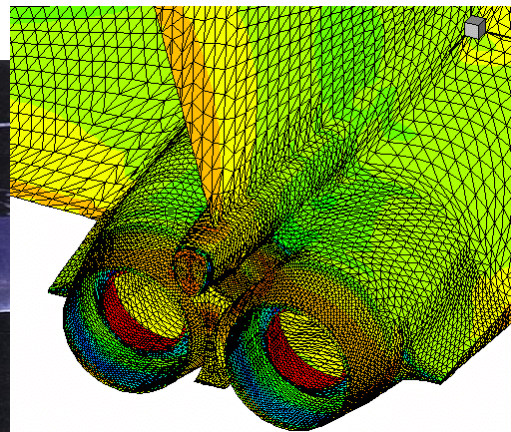


Figure 71. Afterbody surface mesh.

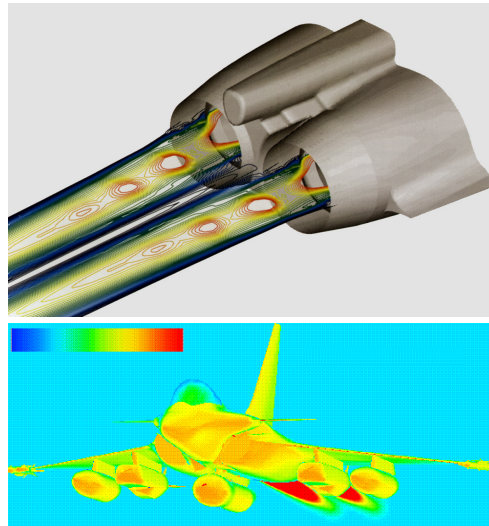


Figure 72. IR signature.

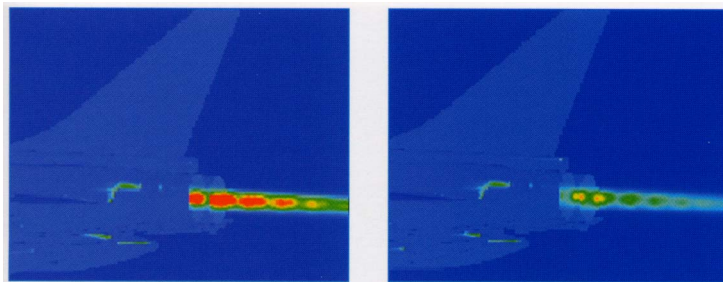


Figure 73. IR signature.

### 16.5. Aircraft cabin air conditioning

Careful air conditioning system is very important for long range business jets because very long duration flights lead to very high quality requirements for passenger comfort. Two criteria are identified: even temperature inside the cabin and low air velocity next to passengers.

The design of the air conditioning system of an aircraft cabin represents a good example of a design problem where a multidisciplinary approach is essential. This can be illustrated by the following key phenomena: air temperature decreases along cold walls next to the fuselage, air density increases and this air is driven downwards. The balance of convective, conductive and radiative heat transfer at the wall must be predicted accurately. A relevant fluid mechanic model is the Boussinesq approximation with buoyancy. Mixing and momentum transfer at air ducts must also be predicted accurately.

An incompressible derivative of the Navier-Stokes code described in section 4 is used for such calculations. For further details the reader is referred to Ravachol (1997).

Simulation of this problem has required an iterative coupling between the heat transfer computation within the aircraft structure, its equipment and insulation material and the flow solution inside the aircraft cabin.

A sample simulation is presented now. The computation is performed in the cabin of a Falcon 900 business jet. The high geometric complexity of the cabin with furniture and passenger models and the high number of inlet and outlet ducts (12 inlet ducts and 10 outlet ducts) add to the difficulty of the simulation task. The mesh includes about 800,000 grid points. The surface mesh is presented in Figure 74. Black surfaces correspond to adiabatic wall conditions; dark blue areas have a transmission condition; the red elements corresponds to different sections of the pilot bodies: they receive a constant heat flux condition ranging from 20 to 40 W/m<sup>2</sup>; inlets are represented in yellow, while outlets appear in green. The temperature inside the cockpit is presented on the surface of the geometry in Figure 75. Known phenomena expressed by passengers and pilots have been reproduced.

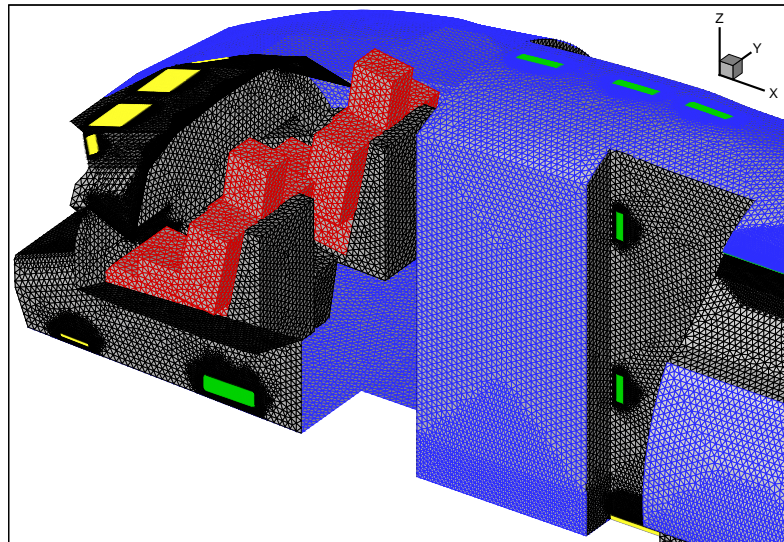


Figure 74. Surface mesh of the Falcon 900 cabin.

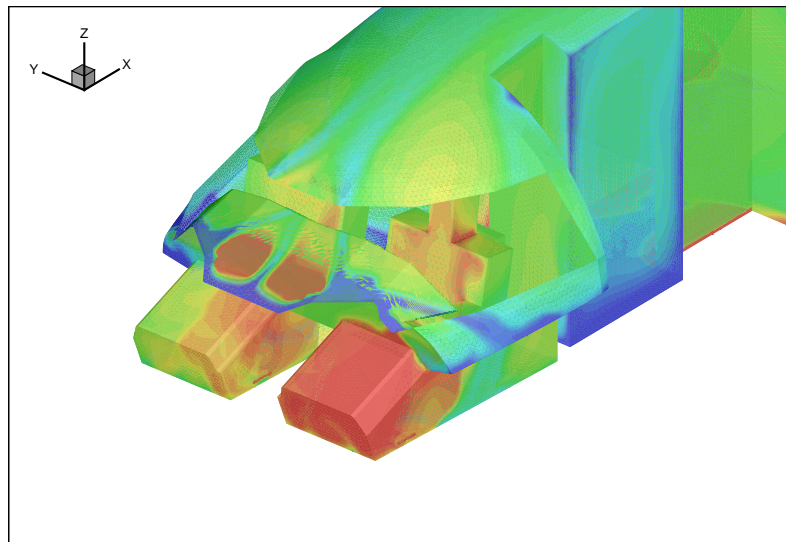


Figure 75. Falcon 900: wall temperatures.

## 17. CONCLUSION

Over the past few years, industrial computational aerodynamics has witnessed a fascinating development and it has reached a level where it has a major impact on aircraft design. The range of scientific issues associated with this development is quite large: it includes advanced mathematical analysis, complex fluid mechanics modeling and high performance computer science technologies. Industrial applications is also the place where science meets a real life problem, in our example beautiful scientific concepts contribute to the perfect design of beautiful aircraft.

A historical perspective has given a measure of the successive giant steps that have been made over the past 30 years. A rather detailed description of industrial codes has led to a good understanding of the key numerical concepts assembled to create a powerful tool for computational aerodynamics. The fundamental issue of turbulence modeling has been addressed in detail. A large range of complex applications has been described to illustrate the variety of problems solved. The status of the development and application of shape optimization techniques and multidisciplinary design has finally been illustrated.

The next decades should seek to achieve equally ambitious goals. Order of magnitude gains in efficiency are still needed to let the designer explore more solutions than is possible today. Widespread use of unsteady simulations will appear: CFD will become a movie maker even with the sound track thanks to the aeroacoustics. Future needs include accurate prediction of always more complex turbulent flows. This includes flows with complex interactions or large scale unsteady behavior and will require further improvement in turbulence models. Large eddy simulation is a very promising approach in particular in the framework of the variational multiscale method. Its application to design will require new developments, a zonal approach with coupling to RANS model might be needed for many applications. A number of multidisciplinary problems are already addressed using complex simulation. Future simulations will include further multidisciplinary problems with strong coupling between models. Examples include reliable and efficient prediction of structural vibration (most notably flutter and buffet induced acceleration), the evaluation of infrared signature or airframe acoustic modeling. The widespread application of automatic shape optimization to various design problems still requires continued effort, in particular when viscous flow models are needed. Multidisciplinary Design Optimization will progressively build powerful tools and lead to high performance designs. One challenge will be to have detailed CAD of all aircraft in the optimization process.

Mathematical insight and deep physical understanding will again be required and combined to allow the design of novel aircraft. Next generation computational aerodynamics techniques must bring to flight efficient environmentally friendly low noise and low emission aircraft, high performance supersonic business jets, innovative military aircraft with unusual shapes or safe space planes.

## ACKNOWLEDGEMENTS

The authors would like to thank all the persons at the Theoretical Aerodynamics Department at Dassault Aviation who have contributed with their work and dedication over the years to the achievement partly presented in this chapter.

We would like to thank in particular people who have directly contributed to the chapter with either texts or illustrations: D Alleau, JC Courty, L Daumas, Th Fanion, JM Hasholder, N Héron, Z Johan, M Mallet, M Ravachol, G Rogé, Ph Rostand, E Teupootahiti, JP Tribot, and B Stoufflet.

A special mention is reserved for Pierre Perrier, who wrote the historical section of the chapter. He started the Theoretical Aerodynamics department at Dassault and we all are very much in debt towards this pioneer of CFD and CAD design, to mention only a few of the many fields he contributed to.

We will also have a special thought for Ph Caupenne, E Guellec, B Mantel, and SA Waiter who have left too soon to see fully the impact of CFD on aircraft design.

### RELATED CHAPTERS

ecm003- ecm010- ecm012- ecm050- ecm051- ecm054- ecm060- ecm061- ecm062- ecm063- ecm064-

### REFERENCES

- Abgrall R. Towards the ultimate conservative scheme: following the queste. *Journal of Comp. Physics: to appear*. 1999.
- Alleau D, Bariant P, Roge G, Teupootahiti E. Interaction aérodynamiques dans les études d'intégration de charge sous avion. *Proceeding AAAF conference*. 1996.
- Bailly C, Candel S and Lafon P. Prediction of supersonic jet noise from a statistical acoustic model and a compressible turbulence closure. *Journal of Sound and Vibration*. 194(2):219–242, 1996.
- Baldwin BS and Barth TJ. A One-Equation Turbulence Model for High Reynolds Number Wall-Bounded Flows. *AIAA Paper*. 1991.
- Baldwin BS and Lomax H. Thin-layer Approximation and Algebraic Model for Separated Turbulent Flows. *AIAA Paper 78-257*, Huntsville, AL. 1978.
- Béchara W, Lafon P, Bailly C and Candel S. Application of a  $k-\epsilon$  turbulence model to the prediction of noise for simple and coaxial free jets. *J. Acoust. Soc. Am.* 97(6):3518–3531, 1995.
- Billey V. *Résolution des équations d'Euler par des méthodes d'éléments finis; application aux écoulements 3D de l'aérodynamique*. PhD Thesis, Université Pierre et Marie Curie, 1984.
- Boussineq J. Théorie de l'Écoulement Tourbillant. *Mém. Présenté par Divers Savants Acad. Sci. Inst. Fr.* Vol 23, pp 46–50. 1877.
- Bristeau MO, Glowinski R, Périaux J, Perrier P, Pironneau O and Poirier G. On the numerical solution of nonlinear problems in fluid dynamics by least squares and finite element methods (II), Application to transonic flow simulations. *Computer Methods in Applied Mechanics and Engineering*. vol. 51, pp. 363–394, 1985.
- Cea J. *Numerical Methods of Shape Optimal Design*, in Optimization of Distributed Parameter Structures (eds. E.J. Haug and J. Cea) Sijthoff and Noordhoff, Alphen aan den Rijn, The Netherlands, 1981.
- Cebecci T and Smith AMO. Analysis of Turbulent Boundary Layers. *Ser. in Appl. Math. & Mech.* Vol XV, Academic Press. 1974.
- Chalot F, Dinh QV, Mallet M, Naïm A and Ravachol M. A multi-platform shared- or distributed-memory Navier-Stokes code. *Parallel CFD '97*. Manchester, UK, May 19–21, 1997.
- Chalot F, Dinh QV, Mallet M, Ravachol M and Rogé G. Parallel CFD: a day-to-day industrial experience. invited keynote lecture, *Parallel CFD '01*. Egmond aan Zee, The Netherlands, May 21–23, 2001.
- Chalot F, Guillemot S, Hasholder JM, Leclercq MP, Mallet M, Naïm A, Ravachol M, Rosemblum JP, Rostand P, Stoufflet B and Teupootahiti E. Validation et utilisation industrielle d'un code résolvant les équations de la mécanique des fluides compressibles. *30ème Colloque d'Aérodynamique Appliquée*. Ecole Centrale de Nantes, Oct25–27, No. 17. 1993.
- Chalot F, Hasholder JM, Mallet M, Naïm A, Perrier P, Ravachol M, Rostand Ph, Stoufflet B, Oskam B, Hagemeyer R and de Cock K. *Ground to flight transposition of the transonic characteristics of a proposed Crew Rescue/Crew Transfer Vehicle*, paper #97-2305, 15th AIAA Applied Aerodynamics Conference, Atlanta, GA, June 23–25, 1997.

*Encyclopedia of Computational Mechanics*. Edited by Erwin Stein, René de Borst and Thomas J.R. Hughes.

© 2004 John Wiley & Sons, Ltd.

- Chalot F and Hughes TJR. A consistent equilibrium chemistry algorithm for hypersonic flows. *Computer Methods in Applied Mechanics and Engineering*. vol. 112, pp. 25–40, 1994.
- Chalot F, Hughes TJR and Shakib F. Symmetrization of conservation laws with entropy for high-temperature hypersonic computations. *Computing Systems in Engineering*. vol. 1, pp. 465–521, 1990.
- Chalot F, Mallet M and Ravachol M. A comprehensive finite element Navier-Stokes solver for low- and high-speed aircraft design, paper #94-0814. *AIAA 32nd Aerospace Sciences Meeting*. Reno, NV, January 10–13, 1994.
- Chalot F, Marquez B, Ravachol M, Ducros F, Nicoud F and T. Poinso T. A consistent Finite Element approach to Large Eddy Simulation. paper #98-2652. *AIAA 29th Fluid Dynamics Conference*. Albuquerque, NM, June 15–18, 1998.
- Chalot F, Marquez B, Ravachol M, Ducros F and T. Poinso T. Large Eddy Simulation of a compressible mixing layer: study of the mixing enhancement. paper #99-3358, *AIAA 14th Computational Fluid Dynamics Conference*. Norfolk, VA, June 28–July 1, 1999.
- Cornuault C, Petiau C, Coiffier B and Paret A. *Structural optimization of aircraft*, Practice and trends, AGARD R-784, 2/92.
- Damas L, Dinh QV, Kleinveld S and Rogé G. *CAD-Based Wing Body Optimization*, CEAS Aerospace Aerodynamics Research Conference, 10–13 June 2002, Cambridge, United Kingdom.
- Damas L, Dinh QV, Kleinveld S and Rogé G. *Recent improvements in aerodynamic design optimization on unstructured meshes*, French/Finnish Seminar, 13–14 June 2002, Jyväskylä, Finland.
- Damas L, Dinh QV, Kleinveld S and Rogé G. *How to take into account deformation in CAD-based Euler optimization process?*, Symposium IUTAM Transsonicum IV, 2–6 September 2002, Göttingen, Germany.
- David E. Modélisation des écoulements compressibles et hypersoniques: une approche instationnaire. *Ph.D. thesis, INP de Grenoble*. 1995.
- Davies POAL, Fisher MJ and Baratt MJ. The characteristics of the turbulence in the mixing region of a round jet. *Journal of Fluid Mechanics*. 15:337–367, 1963.
- Deconinck H, Paillere H, Struijs R and Roe PL. Multidimensional upwind schemes based on fluctuation splitting for systems of conservation laws. *J. Comput. Mech.* Vol. 11, pp. 323–340, 1993.
- Dervieux A, Fezoui L, Leclercq MP and Stoufflet B. A general upwind formulation for compressible flows on multielement meshes. *Numerical methods for Fluid Dynamics*. Oxford Science Publications, 1993.
- Dervieux A, Male JM, Marco N, Périaux J, Stoufflet B and Chen HQ. *Some Recent Advances in Optimal Shape Design for Aeronautical Flows*, Computational Fluid Dynamics '94, J. Wiley, 1994.
- Bristeau MO, Glowinski R, Périaux J and Viviani H (Eds.). *Numerical Simulation of Compressible Viscous Flows, A GAMM Workshop*. Numerical Fluid Mechanics, Vieweg, Braunschweig, **18**, 1986.
- Dervieux A, Van Leer B, Périaux J and Rizzi A (Eds.). *Numerical Simulation of Compressible Euler Flows, A GAMM Workshop*. Numerical Fluid Mechanics, Vieweg, Braunschweig, **26**, 1989.
- Dinh QV, Rogé G, Sevin C and Stoufflet B. *Shape optimization in computational fluid dynamics*, European Journal of Finite Elements, Vol. 5, p. 569–594, Hermes, 1996.
- Fanion Th. *Etude de la simulation numérique des phénomènes d'aéroélasticité dynamique. Application au problème du flottement des avions*. Ph. D. Thesis, University of Paris Dauphine, 2001.
- Farhat C and Lesoinne M. On the accuracy, stability and performance of the solution of three-dimensional nonlinear transient aeroelastic problems by partitioned procedures. *AIAA 96-1388*. 1996.
- Fezoui L and Stoufflet B. A Class of Implicit Upwind Schemes for Euler Simulations with Unstructured Meshes. *J. Comput. Phys.* 84(1), pp 174–206, 1989.
- Fisher MJ, Lush PA and Harper-Bourne M. Jet noise. *Journal of Sound and Vibration*. 28(3):563–585, 1973.
- Fortuné V and Gervais Y. Numerical investigation on noise radiated from hot subsonic turbulent jets. *AIAA 98-2356*. 1998.
- Gatski TB and Speziale CG. On explicit Algebraic Stress Models for Complex Turbulent Flows. *ICASE Report*, No. 92-58. 1992.

*Encyclopedia of Computational Mechanics*. Edited by Erwin Stein, René de Borst and Thomas J.R. Hughes.

© 2004 John Wiley & Sons, Ltd.

- Ghosal S and Moin P. The basic equations for the large eddy simulation of turbulent flows in complex geometry. *Jour. of Comput. Physics*. Vol. 118, pp. 24–37, 1995.
- Glowinski R. *Numerical Methods for Nonlinear Problems*. Springer-Verlag. 1984.
- Hagmeijer R, Oskam B, de Cock KMJ, Perrier P, Rostand Ph, Hasholder JM and Wegereef JW. Validation of the computational methods used for the design of the canopy of the Hermes spaceplane, paper #94-1865. *AIAA 12th Applied Aerodynamics Conference*, Colorado Springs, CO, June 20–22, (1994).
- Héron N, Candel S and Bailly C. Modélisation du rayonnement acoustique de jets coaxiaux supersoniques. *Compte-Rendu de l'Académie des Sciences, Série II b*. pages 497–502, 2001.
- Héron N, Lemaire S, Candel S and Bailly C. Coaxial-jet-noise predictions from statistical and stochastic source models. *AIAA Paper 2001-2205*, 2001.
- Hughes TJR, Franca LP and Mallet M. A new finite element formulation for computational fluid dynamics: I Symmetric forms of the compressible Euler and Navier-Stokes equations and the second law of thermodynamics. *Comp. Meth. in Applied Mech. and Eng.* Vol. 54, pp. 223–234, 1986.
- Hughes TJR and Mallet M. A new finite element formulation for computational fluid dynamics: IV A discontinuity-capturing operator for multidimensional advective - diffusive systems. *Comp. Meth. in Applied Mech. and Eng.* Vol. 58, pp. 329–336, 1986.
- INRIA and GAMNI-SMAI. *Workshop on Hypersonic Flows for Reentry Problems*. Antibes, France, January 22–25, 1990.
- INRIA and GAMNI-SMAI. *Workshop on Hypersonic Flows for Reentry Problems, Part II*. Antibes, France, April 15–19, 1991.
- Jameson A. Numerical computation of transonic flow with shock waves. *Symposium Transsonicum II*. Oswatich K and Rues D, Eds., Springer-Verlag, Berlin. pp. 384–414, 1975.
- Jameson A. Aerodynamic design via control theory. *Journal of Scientific Computing*. 3:233–260, 1988.
- Jameson A and Schmidt W. Some recent developments in numerical methods for transonic flows. *Computer Methods in Applied Mechanics and Engineering*. North Holland. Vol. 51, pp. 467–493, 1985.
- Johan Z. *Data Parallel Finite Element Techniques for Large-scale Computational Fluid Dynamics*. Ph.D. Thesis, Stanford University, 1992.
- Johan Z, Hughes TJR and Shakib F. A globally convergent matrix-free algorithm for implicit time-marching schemes arising in finite element analysis in fluids. *Computer Methods in Applied Mechanics and Engineering*. Vol. 87, pp 281–304, 1991.
- Lauder BE, Reece G. and Rodi W. Progress in the development of a Reynolds stress turbulence closure model. *Letters in Heat and Mass transfer*. Vol. 1, No. 2, 1975.
- Lax P and Wendroff B. Systems of conservation laws. *Communication in Pure and Applied Mathematics*. vol. 13, pp. 217–237, 1960.
- Lighthill MJ. On sound generated aerodynamically, I. general theory. *Proceedings of the Royal Society of London*. 211:564–587, 1952.
- Lighthill MJ. On sound generated aerodynamically, II. turbulence as a source of sound. *Proceedings of the Royal Society of London*. 222:1–32, 1954.
- Lighthill MJ. *On displacement thickness*, *Journal of fluid mechanics*, Vol.4, p383–392, 1958.
- Lilly DK. Lectures notes on turbulence. *World Scientific*. 1987.
- Lions JL. *Contrôle optimal des systèmes gouvernés par des équations aux dérivées partielles*, Dunod, Gauthier-Villars, Paris 1968.
- Morfey CL. Sound radiation due to unsteady dissipation in turbulent flows. *Journal of Sound and Vibration*. 48(1):95–111, 1976.
- Murman EM and Cole J. Calculation of plane, steady, transonic flows. *AIAA Journal*. Vol. 9, pp. 114–121, 1971.

- Naïm A, Mallet M, Rostand Ph and Hasholder JM. Local aerothermal problems during Hermes reentry. *Theoretical and Experimental Methods in Hypersonic Flows*. AGARD Conference Proceedings 514, pp. 42-1–42-16, (1993).
- Papamoschou D and Debiassi M. Noise measurements in supersonic jets treated with the mach wave elimination method. *AIAA Journal*. 37(2):154–160, 1999.
- Pironneau O. *Optimal Shape Design for Elliptic Systems*, Springer-Verlag, New-York, 1984.
- Polak E. *Computational methods in Optimization, a unified approach*. Math. In Sci. and Eng., Vol. 77, Academic Press, 1971.
- Rodi W. A new algebraic relation for calculating reynolds stresses. *ZAMM*, vol. 56, p. 219. 1976.
- Ravachol M. Unstructured finite elements for incompressible flows, paper #97-1864. *AIAA 28th Fluid Dynamics Conference*. Snowmass Village, CO, June 29–July 2, 1997.
- Rostaing N, Dalmas S and Galligo A. Automatic Differentiation in Odyssée. *Tellus*. (45A):358–368, 1993.
- Schwartz L. *Introduction à PERL (Practical Extraction and Report Language)*. Editions O'Reilly Internatinal Thomson, 1995.
- Selmin V. A Multistage Method for the Solution of the Euler Equations on Unstructured Grids. *Proceedings of the 5th International Symposium on Numerical Methods in Engineering*. Gruber R, Périaux J and Shaw RP Eds., Springer-Verlag. Vol. 2, pp. 449–454, 1989.
- Shakib F, Hughes TJR and Johan Z. A multi-element group preconditioned GMRES algorithm for nonsymmetric systems arising in finite element analysis. *Computer Methods in Applied Mechanics and Engineering*. Vol. 75, pp 415–456, 1989.
- Shakib F, Hughes TJR and Johan Z. A new finite element formulation for computational fluid dynamics: X. The compressible Euler and Navier-Stokes equations. *Computer Methods in Applied Mechanics and Engineering*. Vol. 89, pp 141–219, 1991.
- Spalart PR and Allmaras SR. A One-Equation Turbulence Model for Aerodynamic Flows. *La Recherche Aérospatiale*. No.1, pp. 5–21. 1994.
- Spalart PR, Jou WH, Strelets M and Allmaras SR. Comments on the feasibility of LES for wings and on an hybrid LES/RANS approach. *Advances in DNS/LES*. pp. 117–128, 1997.
- Stone JR. Interim prediction method for jet noise. *Technical report*. NASA-TM-X-71618, 1974.
- Struijs R, Roe PL and Deconinck H. Fluctuations Splitting Schemes for the 2-D Euler Equations. *Von Karman Institute Report*, 1991-11/AR. 1991.
- Tanna HK. An experimental study of jet noise. Part I: turbulent mixing noise. *Journal of Sound and Vibration*. 50(3):405–428, 1977.
- Tribot JP, Chalot F, Rapuc M and Durand G. Large gliding parachute, experimental and theoretical approaches. paper #97-1482. *AIAA 14th Aerodynamic Decelerator Systems Technology Conference*. San Francisco, CA, June 2–5, 1997.
- Vos JB, Rizzi AW, Darracq D and Hirschel E. *Navier-Stokes solvers in European aircraft design*, Progress in Aeronautic Sciences, 38(8):601–699, 2003.
- Wallin S, Johansson A, Lindblad I, Friedrich R, Lechner L, Krogmann P, Schülein E, Courty JC, Ravachol M and Giordano D. A prediction method for high speed separated flows with experimental verification. *AIAA paper #98-2547* 1998.
- Zoutendijk M. *Methods of Feasible Directions*. Elsevier Publishing Co, Amsterdam, 1960.

## FURTHER READING

- Bonfiglioli A, van der Weide E and Deconinck H. Study of 3-D hypersonic flow using unstructured grid solvers based on multidimensional upwinding. *von Karman Institute for Fluid Dynamics report*. 1996.
- Bradshaw P. The Response of a Constant-Pressure Turbulent Boundary Layer to the Sudden Application of an Adverse Pressure Gradient. *R. & M. Number 3575*, British Aeronautical Research Council. 1969.
- Chalot F, Dinh QV, Mallet M, Ravachol M, Rogé G, Rostand Ph and Stoufflet B. CFD for aircraft design: recent developments and applications. *4th ECCOMAS Computational Fluid Dynamics Conference*. Wiley, 1998.
- Chollet JP and Lesieur M. Parametrization of small scales of the three dimensional isotropic turbulence utilizing spectral closures. *J. Atmos. Sci.* Vol. 38, pp. 2747–2757, 1981.
- Comte Bellot G and Corrsin S. Simple Eulerian time correlation of full and narrow band velocity signals in grid generated isotropic turbulence. *Journal of Fluid Mechanics*. Vol. 48, pp. 273–337, 1971.
- Deconinck H, Hirsch Ch and Peuteman J. Characteristic decomposition methods for the multidimensional Euler equations. *Lect. Notes Phys.* Springer-Verlag . Vol. 264, 1986.
- Deconinck H, Roe PL and Struijs R. A multidimensional generalization of Roe's flux difference splitter for the Euler equations. *J. Comput. and Fluids*. Vol. 22, pp. 215–222, 1993.
- Dinh QV, Kleinveld S, Ribaute P and Rogé G. *CFD-Based Aerodynamic Shape Optimization*, CEAS Conference on Multidisciplinary Aircraft Design and Optimization, 25–27 June 2001, Köln, Germany, 2001.
- Farhat C and Lesoinne M. Higher-order Staggered and Subiteration Free Algorithm for Coupled Dynamic Aeroelasticity Problems. *AIAA Paper 98-0516*, 36th Aerospace Sciences Meeting and Exhibit. Reno, NV, January 1998.
- Faure C and Papegay Y. Odyssée Version 1.6, The User's Reference Manual. *Rapport INRIA 0211*. 1997.
- Favre A. Equations des gaz turbulent compressibles. *Journal de Mécanique*. Vol. 4, No. 3, pp. 361–390, 1965.
- Harten A, Lax PD and Van Leer B. On upstream differencing and Godunov type schemes for hyperbolic conservation laws. *S.I.A.M. Review*. Vol. 25(1), 1983.
- Hughes TJR, Franca LP and Mallet M. A new finite element formulation for computational fluid dynamics: VI Convergence analysis of the generalized SUPG formulation for linear time dependent multidimensional advective diffusive systems. *Comp. Meth. in Applied Mech. and Eng.* Vol. 63, pp. 97–112, 1987.
- Hughes TJR and Mallet M. A new finite element formulation for computational fluid dynamics: III The generalized streamline operator for multidimensional advective - diffusive systems. *Comp. Meth. in Applied Mech. and Eng.* Vol. 58, pp. 305–328, 1986.
- Hughes TJR, Mallet M and Mizukami A. A new finite element formulation for computational fluid dynamics: II Beyond SUPG. *Comp. Meth. in Applied Mech. and Eng.* vol. 54, pp. 341–355, 1986.
- Jones WP and Launder BE. The prediction of Laminarisation with a Two-Equation Model of Turbulence. *International Journal of Heat and Mass Transfer*, Vol. 15, pp.301–314. 1972.
- Lesieur M. *Turbulence in fluids*. Kluwer Academic Publishers, second edition. 1990.
- Menter FR. Zonal Two equation  $k-\omega$  Turbulence Models for Aerodynamic Flows. *AIAA Paper 93-2906*, Orlando, FL. 1993.
- Morel T and Mansour NN. Modeling of Turbulence in Internal Combustion Engines. *SAE Technical Papers Series* # 820040. 1982.
- Paillère H. *Multidimensional Upwind Residual Distribution Schemes for the Euler and Navier-Stokes Equations on Unstructured Grids*. Ph.D. thesis, Université Libre de Bruxelles. 1995.
- Paillère H, Deconinck H and van der Weide E. Upwind residual distribution methods for compressible flow: an alternative to finite volume and finite element methods. *von Karman Institute for Fluid Dynamics*. presented at the 28th CFD Lecture Series, 1997.
- Park C. *Nonequilibrium Hypersonic Aerothermodynamics*. Wiley-Interscience, 1990.

- Patel VC and Chen HC. Near-wall turbulence models for complex flows including separation. *AIAA Journal*, vol. 29, No. 6. 1984.
- Peraire J, Peiro J, Formaggia L, Morgan K and Zienkiewicz OC. Finite Element Euler Computations in Three Dimensions. *Internat. J. Numer. Methods Engrg.* Vol. 26, pp. 2135-2159, 1988.
- Prandtl L. *Tragflügeltheorie*, Nachr. Ges. Wiss., Göttingen, vol. 107 and 451, 1918.
- Reynolds WC. Modeling of Fluid Motions in Engines: An Introductory Overview. *Symposium on Combustion Modeling in Reciprocating Engines*, Plenum Press, pp 131-155. 1980.
- Roe PL. Discrete models for the numerical analysis of time-dependent multidimensional gas dynamics. *J. Comput. Phys.* Vol. 63, pp. 458-476, 1986.
- Roe PL. Linear advection schemes on triangular meshes. *Technical report*. Cranfield Institute of Technology, CoA 8720. 1987.
- Rudgyard M. Cell-vertex methods for steady inviscid flow. *VKI LS 1993-04*. Computational Fluid Dynamics. 1993.
- Saad Y and Schulz MH. GMRES: a Generalized Minimal Residual algorithm for solving nonsymmetric linear systems. *SIAM Journal of Scientific and Statistical Computing*. vol. 7, pp. 856-869, 1986.
- Sidilkover D. Numerical solution to steady-state problems with discontinuities. *Ph.D. thesis, The Weizmann Institute of science, Rehovot, Israel*. 1989.
- Sidilkover D. Multidimensional upwinding and multigrid. *in 12th AIAA CFD Conference*. San Diego, Paper 95-1759, 1995.
- Sidilkover D and Roe PL. Unification of some advection schemes in two dimensions. *Technical Report 95-10*. ICASE. 1995.
- Steger J and Warming RF. Flux vector splitting for the inviscid gas dynamic with applications to finite difference methods. *Journal Comp. Physics*. Vol. 40(2), pp. 263-293, 1981.
- Struijs R, Deconinck H, De Palma P, Roe PL and Powell KG. Progress on multidimensional upwind Euler solvers for unstructured grids. *AIAA-91-1550*. 1991.
- The University of Texas at Austin, The US Air Force Academy and GAMNI-SMAI. *The Second Joint Europe/US Short Course in Hypersonics*. USAF Academy, Colorado Springs, CO, January 16-20, 1989.
- Van Leer B, Lee WT and Roe PL. Characteristic Time-Stepping or Local Preconditioning of the Euler Equations. *in AIAA 10th Computational Fluid Dynamics Conference*. AIAA-91-1552-CP. 1991.
- Viegas JR, Rubesin MW and Horstman CC. On the use of Wall Functions as Boundary Conditions for Two-dimensional Separated Compressible Flows. *AIAA paper 85-0180*. 1985.
- Weber C. Développement de méthodes implicites pour les équations de Navier-Stokes moyennées et la simulation des grandes échelles: application à l'aérodynamique externe. *PhD thesis INP de Toulouse*. 1998.

## TABLES AND CAPTIONS

## FIGURES AND CAPTIONS

## SCHEMES AND CAPTIONS